Title
The Electrodeposition of PbTe Nanowires for Thermoelectric Applications

Author
Hillman, Peter

Publication Date
2012

Peer reviewed|Thesis/dissertation

The Electrodeposition of PbTe Nanowires for Thermoelectric Applications

By

Peter Hillman

A dissertation submitted in partial satisfaction of the

requirements for the degree of

Doctor of Philosophy

in

Chemistry

in the

GRADUATE DIVISION

of the

UNIVERSITY OF CALIFORNIA, BERKELEY

Committee in charge:
Professor Angelica Stacy, Chair
Professor Jeffrey R. Long
Professor Junqiao Wu

Spring 2012

The Electrodeposition of PbTe Nanowires for Thermoelectric Applications

Peter Hillman

Abstract

The Electrodeposition of PbTe Nanowires for Thermoelectric Applications

by

Peter Hillman

Doctor of Philosophy in Chemistry

University of California, Berkeley

Professor Angelica Stacy, Chair

The electrodeposition of PbTe nanowires for thermoelectric applications is presented in this thesis. The Pb-Te electrochemical system was investigated to determine the optimal conditions for deposition. It was found that citric acid complexed tellurium in solution shifting its reduction potential cathodically. The shift in reduction potential led to the deposition of pure PbTe without any observable excess tellurium.

Nanowires of PbTe were doped p-type and n-type through the addition of thallium and indium to the plating solution. Indium-doped nanowire arrays showed a linear relation between lattice parameter and atomic percent indium confirming successful incorporation. The lattice parameter trend in thallium-doped nanowire arrays was linear only after annealing. In the case of thallium doping, thallium tellurides were formed, which upon annealing formed a solid solution with PbTe.

The results of the thallium doping study led to the investigation of the Tl-Te electrochemical system. Cyclic voltammagrams were used to determine the deposition mechanism of TlTe and Tl_5Te_3. Thin films and nanowire arrays of these compounds were deposited. This was the first study of the electrochemical Tl-Te system and the first report of the electrodeposition of TlTe and Tl_5Te_3.

Thermoelectric measurements were conducted on thin films and nanowire arrays of PbTe. The Seebeck coefficient and resistivity of PbTe thin film were measured. Results from thin films were complicated by the Pt substrate on which PbTe was deposited. Subtracting the effects of the Pt layer suggested PbTe thin films could have a large zT, however further work is needed to confirm this result. Resistivity measurements on nanowire arrays were also conducted. Despite efforts to minimize the oxidation of PbTe nanowires, good electrical contacts could not be created. The resistivity of nanowire arrays were orders of magnitude higher than expected. As a result of their low conductivity, the thermoelectric efficiency of PbTe nanowires were negliglable.

Nanotube arrays of conductive polyaniline were synthesized through the electrochemical deposition into porous anodic alumina. PbTe nanowires were deposited into these nanotubes to create a PbTe/polyaniline core-shell structure. PbTe/polyaniline hybrids should have a lower thermal conductivity than pure PbTe. Measurements of PbTe/polyaniline core-shell nanowires are still needed to confirm the predicted lower thermal conductivity.

Table of Contents

List of Figures

List of Tables

Acknowledgements

There are many people I would like to thank, who without their help and support, this disseration would not have been possible. First, thank you to the entire Stacy group past and present for all their advice and support. In particular, thank you to Philip Kalisman for serving as a sounding board for my many ideas on thermoelectrics and nanowires. I owe a debt of gratitude to the entire thermoelectrics team, particulary Jeff Sharp and Todd McBee, whose expert knowledge made all this work possible. Also, I would like to thank Marisol Martin-Gonzalez and Cristina Vicente for all their hard work to measure the thermoelectric properties of PbTe thin films. Thank you to Angy Stacy for your mentorship throughout the years. You have always challenged and allowed me to explore new ideas which has helped me become a better scientist. Last and certainly not least, thank you to my wonderful wife Young. Without your love and support, I would never have been able to endure the long and grueling hours in lab. You have sacrificed a lot for me to be able to achieve my goal and I don't think I can ever thank you enough. I promise to provide the same encouragement and patience you gave me as you begin your graduate career.

Chapter 1: Introduction

Increasing demands for new, clean, and renewable energy sources has led to resurgence in the field of thermoelectric materials. Thermoelectric devices have the ability to interconvert heat and electricity and for this reason have been proposed as a source for clean power generation and refrigeration.[1] However, the figure of merit (zT), which is directly related to device efficiency, has remained too low for broad based applications, relegating them to niche applications, such as the Voyager Missions.[2,3]

In order to compete effectively with commercial refrigeration and power generation units, a zT of 3-4 will be needed.[4] Unfortunately, discovering new materials with high zTs has proved especially challenging. Nanowires thermoelectrics, however, have the potential to significantly improve current devices and revolutionize the world of thermoelectrics.[5,6,7] Both the synthesis and the characterization of nanowire arrays for thermoelectric applications will be presented in this work. A detailed investigation into the electrochemical synthesis of PbTe will be discussed along with measurements to determine the thermoelectric efficiency of nanowire devices and the viability of nanomaterials for thermoelectric applications.

1.1 World Energy Challenges

Based on projections of population growth and economic development, the rate of global energy expenditures is predicted to rise from 2001 levels of 13.5 TW to 27.6 TW in 2050 and 43 TW in 2100.[8] Even though there are oil, natural gas, and coal reserves to meet energy requirements in the future, there could be dramatic consequences to utilizing these carbon based fuels.[8] There are serious climate concerns about the increasing levels of CO_2 in the atmosphere. Current CO_2 level in the atmosphere is about 380ppm, which is much higher than pre-industrial levels of between 210 to 300 ppm.[9,10] Research suggests that at 550 ppm dramatic climate effects might be observed and at this level the CO_2 in the atmosphere could enter a positive feedback loop.[11] Without serious changes in global energy strategies, atmospheric CO_2 levels are predicted to pass this tipping point and more than double within the 21st century.

To prevent the catastrophic effects of increased CO_2 levels in the atmosphere, clean and renewable energy sources must make up a larger percentage of the earth's energy usage. Increasing the use of carbon neutral energy sources such as solar, wind, hydroelectric, geothermal, and nuclear must be part of the solution. However, because technological developments are still required before these energy sources can be fully deployed, fossil fuels are likely to remain the primary energy source of the planet in the near future. The best strategy to limit CO_2 emissions within the confines of fossil fuels is to increase the efficiency of their use.

Today, most of the global power is delivered through heat engines that operate with efficiencies of 30-40%. As a consequence, in the U.S. in 2006 roughly 60% of the energy consumed was lost as waste heat.[12] Collecting this waste heat and converting it to usable energy will therefore dramatically improve engine efficiencies. Thermoelectrics, which have the ability to convert temperature gradients into electrical energy, could be used to capture waste heat and improve the efficiency of fossil fuel usage. However,

improvements in thermoelectric technology are needed before any practical and cost effective implementation can be achieved. A detailed description of thermoelectrics and advances in the field will be provided in this introduction.

1.2 Thermoelectrics

The thermoelectric effect encompasses three related phenomena; the Seebeck effect, the Peltier effect, and the Thomson effect. In 1821 Thomas Johann Seebeck observed a voltage across two different conductors in a temperature gradient. This effect became known as the Seebeck effect and arises from the diffusion of electrons (or holes) from the hot to the cold side in the metal creating an electric field. The Seebeck coefficient is defined as the electric potential divided by the applied temperature gradient.

$$S_{AB} = dV/dT \tag{1.1}$$

Figure 1 shows a basic thermoelectric circuit. If A and B are two different materials and T_1 and T_2 two different temperatures a Seebeck voltage S_{AB} can be measured. The Seebeck coefficient typically has units of μV/K and can have values that are both positive and negative. Negative Seebeck coefficients generally correspond to electrons being the majority carrier while materials with positive Seebeck coefficients have holes as their majority carrier. Typical values of the Seebeck coefficient range from near 0 for metals to +/- 600 μV/K for lightly doped semiconductors.

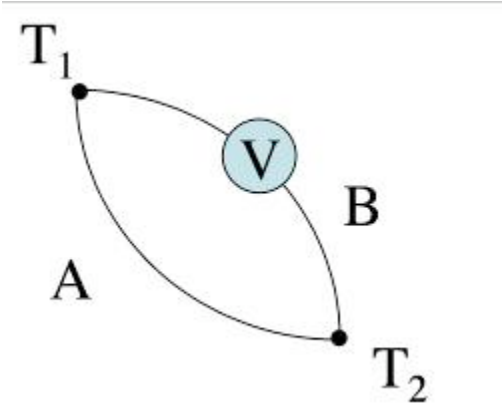

Figure 1-1. Thermoelectric circuit

In 1834 Jean Charles Anthanase Peltier discovered effectively the reverse of the Seebeck effect, the Peltier effect. Instead of applying a temperature gradient as in Figure 1, a current passing through A and B will cause heat to be absorbed and emitted at the positions labeled T_1 and T_2 forming a temperature gradient. The heat absorbed at the junction of the two materials can be defined as

$$Q = \Pi_{AB} I \tag{1.2}$$

where Π is Peltier coefficient and I is the current through the device. The description of the Peltier effect is similar to the Seebeck effect. In this case, electrons moving through

the device carry heat with them thus generating a temperature gradient. Like the Seebeck coefficient, the Peltier coefficent can either be negative or positive depending on the majority carrier.

The Thomson effect, observed by Lord Kelvin in 1851, is the heating or cooling of a material with a current in a temperature gradient. Heating or cooling from the passage of a current through the material can be calculated from the following equation

$$Q = B\ I\ \Delta T \tag{1.3}$$

where B is the Thomson coefficient, I the current, and ΔT the temperature difference.

The Thomson relations relate the three different effects and their coefficients in two equations. The Seebeck coefficient and the Peltier coefficient are related through

$$S_{AB} = \Pi_{AB}/T \tag{1.4}$$

The Thomson coefficient and the Seebeck coefficient can be similarly linked

$$dS_{AB}/dT = (B_a - B_b)/T \tag{1.5}$$

Thermoelectric materials with opposite Seebeck coefficients can be combined to create a thermoelectric device that has the ability to convert a temperature gradient into electrical energy. The reverse is also true; electrical energy can be used to generate a temperature gradient. A thermoelectric device is designed with n-type and p-type semiconductors electrically connected in series and thermally in parallel as shown in Figure 2. Here a heat source causes electrons and holes to diffuse from the hot to the cold side generating an electrical current.

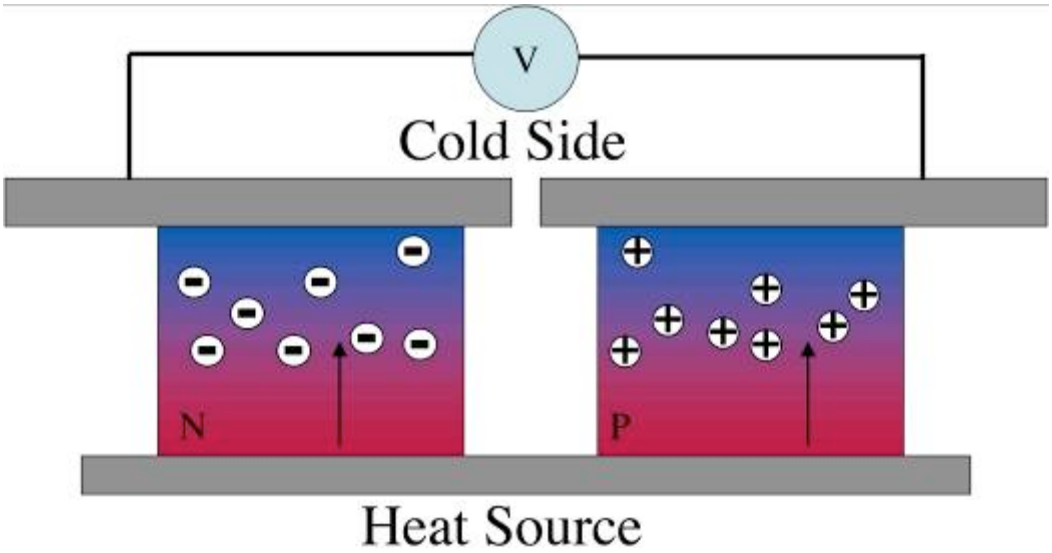

Figure 1-2. Thermoelectric device collecting energy from a temperature gradient

While there could an infinite number of applications for a device that can interconvert electricity and heat, refrigeration, waste heat recovery, and power generation are the majority of applications for thermoelectric devices.

Refrigeration typically makes use of vapor-compression systems. These systems have many moving parts and often employ refrigerants that are detrimental to the environment. Thermoelectric cooling on the other hand requires no moving parts or dangerous refrigerants. Thermoelectric devices are also completely scalable, unlike mechanical systems. Scalability has obvious benefits for cooling applications where a small size is crucial, for example in computer cooling.

Thermoelectric waste heat recovery systems attempt to save energy by capturing waste heat that would be normally lost to the environment and converting it into useful energy. Car manufactures are researching ways to include thermoelectric devices to capture waste heat from car engines and improve fuel efficiency. A typically car engine only operates with a 25% efficiency.[13] Capturing as little as 10% of the waste heat from the engine could provide as much as a 20% boost in fuel efficiencies.[14] BMW has manufactured a concept car making use of thermoelectrics that has a 5% better fuel efficiency than one without this waste heat recovery system.[4]

Power generation is another major application of thermoelectrics. Radioisotope Thermoelectric Generator Systems (RTG) generate electrical power by collecting the heat given off by a radioactive material. RTGs find particular usefulness in space mission applications, where it is not feasible to use solar power. The voyager spacecrafts launched in 1977 are powered by RTGs and are expected to be operational until 2025-2030.[15] The incredibly long lifetime of the voyager spacecraft is due to the reliable nature of RTGs. Free from moving parts, RTGs can operate maintenance free for extended periods of time. Success in RTGs has led to their continued use by the space industry. The recently launched Mars Science Laboratory is using a RTG to power the rover Curiosity.[16]

Solar thermoelectric generators are a more terrestrial based application for power generating thermoelectric devices. Solar thermoelectric generators use radiation from the sun instead of a radioisotope to heat one side of a thermoelectric device. Recent research has shown that these types of devices can effectively compete with other photovoltaic and solar thermal systems.[17]

Despite the obvious benefits of using thermoelectric devices for certain applications their use has yet to become truly wide spread because of their low efficiencies. Thermoelectrics are judged by the figure of merit, zT

$$zT = (S^2 \sigma T)/\kappa \tag{1.6}$$

where T is the temperature, S the Seebeck coefficient, σ the electrical conductivity, and κ the thermal conductivity. Overall device efficiency can be calculated from the figure of merit through the following equation,

$$\eta = \{(T_H - T_C)/T_H\} \{(1+ZT_{avg})^{1/2} - 1\}/\{(1+ZT_{avg})^{1/2} + (T_C/T_H)\} \tag{1.7}$$

where T_H is the hot side temperature, T_C the cold side temperature, and T_{avg} the average temperature between the two sides.[18] Figure 3 displays the calculated efficiencies for ZT

of 0.7, 4, and 20, along with the maximum Carnot efficiency (ZT = ∞). Also shown in the figure are some common mechanical heat engines and their corresponding efficiencies. Despite the fact that Seebeck effect was discovered nearly 200 years ago, the figure of merit of the best materials has hovered only around 1, slightly better than the lowest curve in the figure. To compete with most heat engines figure of merits will have to improve significantly.

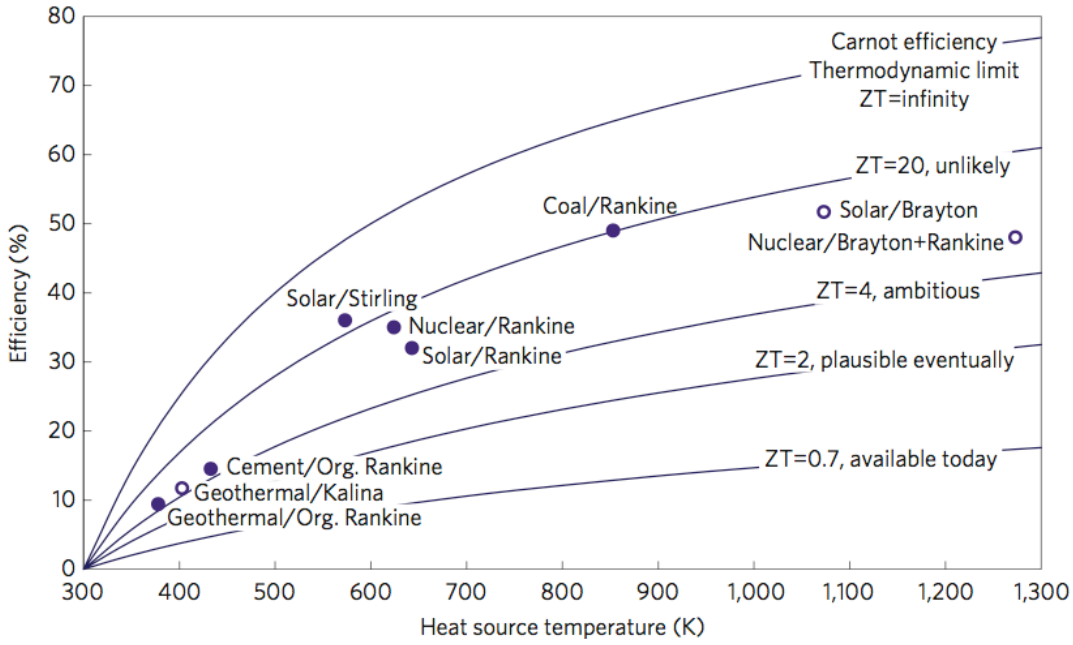

Figure 1-3. Efficiencies of various ZTs compared with various heat engines[4]

The reason it has proved difficult to find new materials with a higher zT is the fact that a material with a simultaneous high Seebeck coefficient, high electrical conductivity, and low thermal conductivity is next to impossible. Insulators have large Seebeck coefficients and low thermal conductivities, but are poor electrical conductors. Metals on the other hand are good conductors, but have low Seebeck coefficients and high thermal conductivities. The widely differing carrier concentrations of metals and insulators lead to the discrepancy in their properties. In the "goldilocks zone" of thermoelectrics are semiconductors. They represent a tradeoff of the best properties of metals and insulators. Semiconductors with carrier concentrations between 10^{19} and 10^{21} carriers per cm^3 tend to have the highest zTs.[19]

The thermal conductivity of a material can be broken down into an electronic portion and lattice portion. The electronic portion of thermal conductivity depends only on the carrier concentration, while the lattice portion can be lowered through careful selection of constituent elements. Heavy atoms, large unit cells, and alloying all serve to lower the lattice thermal conductivity.[19]

The best thermoelectric materials are therefore generally highly doped, high mobility semiconductors made of heavy elements. PbTe, Bi_2Te_3, and Sb_2Te_3 are materials that meet all requirements and some of the best and most common thermoelectrics. Despite the fact that the criteria for a good thermoelectric are met, these

materials still only have a moderate figure of merit. This problem has led researchers to search for new materials and also for ways to modify existing materials to improve their properties.

1.3 Advanced Thermoelectrics

Advancements in thermoelectrics in recent years have mainly focused on lowering the thermal conductivity of materials. The ideal thermoelectric would be what is called a phonon glass/electronic crystal (PGEC). The goal of PGEC concept is to lower the lattice thermal conductivity to a glass-like state while maintaining good electrical conductivity.[20] The generic approach to create a PGEC material is to selectively scatter heat carry phonons while allow electronic carriers to travel unperturbed. Numerous methods are being investigated for creating phonon scattering centers. Among some of the more successful methods include incorporating donor atoms in voids, synthesizing materials with complex crystal structures, and creating materials with nanoscale impurity phases.

Compounds with large voids in their crystal structure are actively being researched to create a PGEC. Clathrates are one group of compounds that crystallize with large voids in their structure and show thermoelectric promise.[21] Skutterudites are another class of compounds being investigated that similarly have large cavities.[22] These voids can be filled with a heavy atom that can act as a "rattler" in the cavity. The rattler atom can selectively scatter phonons allowing electrons to travel by unperturbed leading to low thermal conductivities and high electrical conductivities. More work in the field of skutterudites is needed to determine the optimal parameters for the highest zTs. Selectively filling only certain voids or filling voids with different atoms could lead to an even greater reduction in thermal conductivity. Also, the "rattler" atoms that lower the thermal conductivity often act as dopants, which affect the electronic transport properties. Tuning the "rattler" atom incorporation to maximize both the electronic and thermal properties is still an active area of research.

Complex unit cells also have been a way to lower the thermal conductivity of compounds. $CsBi_4Te_6$ is one example. Compared to its parent compound, Bi_2Te_3, the complex crystal structure of $CsBi_4Te_6$ leads to a lower lattice thermal conductivity.[23] The zintl compound $Yb_{14}MnSb_{11}$ has multiple structural elements and a complex crystal structure leading to a low thermal conductivity and a high zT at 900 °C.[24,25] Besides inherently having low thermal conductivities due to complex structures, these materials all have multiple structural elements, which allow for the possibility of substructure approach to achieve a PGEC material. One structural element could serve as electronic crystal, while another element could serve as insulating phonon-glass. Future research is needed to discover new complex materials with these desired structural elements.

Another successful method of lowering the thermal conductivity of a material is introducing complex nanostructuring into bulk materials. PbTe and Sb_2Te_3 will form a metastable compound, which decomposes into microstructured lamellae of Sb_2Te_3 and PbTe.[26,27] These lamellae effectively scatter phonons but not electrons creating a PGEC type material. $(AgSbTe_2)_x(PbTe)_{1-x}$,known as LAST, also has a very low lattice thermal conductivity. Originally thought to be a solid solution, it was discovered that the compound actually consists of 1-10 nm Ag-Sb rich nanoparticles precipated from the

bulk structure.[28,29] These nanoparticles scatter phonons leading to a thermal conductivity of around 0.5 $Wm^{-1}K^{-1}$ at 700 K, yielding a zT of 2.2 at 800 K.[30] One question that has not been sufficiently answered is the stability of these types of materials during long periods of high temperature operation. Held at high temperatures for an extended period of time the nanoparticles might agglomerate leading to a reduction in zT.

These strategies to lower the thermal conductivity have produced some of the highest zTs to date and have far surpassed the typical value of zT=1 found in common thermoelectric materials. However, continuing in this direction most likely will not yield further improvements in the figure of merit. The lattice thermal conductivity has a lower limit where the phonon mean free path becomes comparable to the lattice spacing of the atoms.[31] The lattice thermal conductivity of a material can be written as

$$\kappa_L = 1/3\ C\ v\ l \tag{1.8}$$

where C is the heat capacity per unit volume, v the speed of sound in the material, and l the mean free path of the phonons. Using the atom spacing of PbTe as the minimum phonon mean free path and plugging in the values of the speed of sound and heat capacity per unit volume, the minimum thermal conductivity of PbTe can be calculated to be around 0.2 W/mK. Repeating this calculation for a variety of compounds the lowest lattice thermal conductivities possible are in the range of 0.1 to 0.2 $Wm^{-1}K^{-1}$.[32] The best thermoelectrics are already approaching these limiting values so without a simultaneous increase in the power factor ($S\sigma^2$) improvements to the figure of merit will be hard to come by.

1.4 Thermoelectric Nanowires

Lower dimension materials, such as nanowires, are predicted to not only lower the lattice thermal conductivity but also increase the power factor, which is needed to achieve even higher figure of merits.[7] By confining a system to a 1-D nanowire there is a change in the materials density of states. The new density of states now has periodic spikes followed by $E^{-1/2}$ decay. Figure 4 illustrates the change in density of states when going from a 3-D bulk solid to a 1-D nanowire.

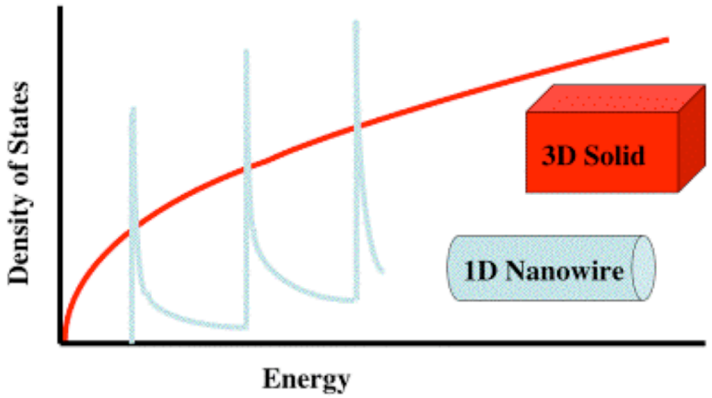

Figure 1-4. Density of states for a nanowire and 3-D solid

The result of the increased density of states in the nanowire leads to an increased Seebeck coefficient. The reason for the increase comes from the Mott equation for the Seebeck coefficient,

$$S = (\pi^2/3)\,(k_b/q)\,k_bT\,\{(1/n)\,dn(E)/dE + (1/\mu)\,d\mu(E)/dE\} \qquad (1.9)$$

where k_b is the Boltzman constant, T the temperature, q the carrier charge, $\mu(E)$ the mobility, and n(E) the carrier density.[33] In the case of the nanowire, the derivative of the density of states with respect to energy at the Fermi level is much greater than the 3-D solid. This effect has been experimentally observed in nanowires of Bi.[34] The enhanced Seebeck coefficient in bulk thallium doped lead telluride is predicted to arise due to a similar mechanism.[35] Thallium creates a resonant energy level in PbTe increasing the density of states at the Fermi level, thus increasing the Seebeck coefficient.

In addition to an increased Seebeck coefficient thermoelectric, nanowires should have a significantly lower thermal conductivity than their bulk counterparts. As the size of the nanowire approaches the mean free path of phonons (the median phonon free path in PbTe is about 42 nm[36]) thermal conductivity will drop due to increased phonon scattering. This effect is similar to the mechanism of the low observed thermal conductivities in the nano and micro- structured bulk thermoelectrics mentioned earlier. Also, like mentioned before, the lower limit on the thermal conductivity in the case of nanowires is near 0.2 W/mK, necessitating a simultaneous increase in the power factor to significantly increase ZT.

Because of both the increased Seebeck coefficient and reduced thermal conductivities, figure of merits for nanowire thermoelectrics are predicted to reach unheard-of values. Take for example the specific case of Bi_2Te_3 nanowires. Theoretical calculations propose that the zT of the smallest wires could approach 20. Shown in Figure 5 the zT of 3-D, 2-D, and 1D Bi_2Te_3 is plotted versus the size of the material.

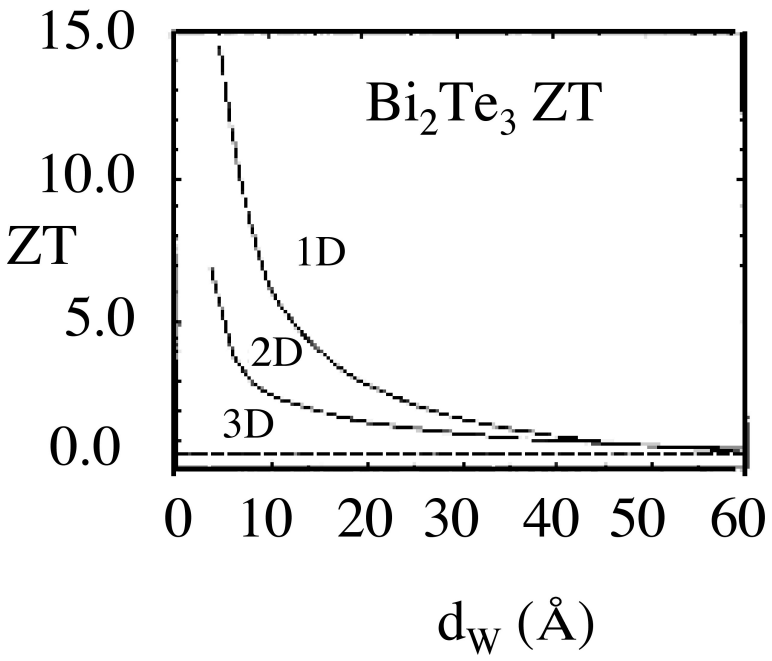

Figure 1-5. zT of 3-D, 2-D, and 1-D Bi2Te3 as a function of size[37]

Partial conformation of these predictions has been demonstrated in nanostructure superlattices of PbTe/$Pb_{1-x}Eu_xTe$ and Bi_2Te_3/Sb_2Te_3, which have the highest figures of merits reported in the literature to date.[38,39,40,41,42,43,44] Most of the improvement in these systems comes from their lower thermal conductivity however, and not from an increased power factor. In addition, these materials are synthesized through costly methods limiting their usefulness for real world applications.

Additional theoretical work has shed some light on why increased power factors in nanowires have proven elusive.[45] In the original work, the power factor of nanowires was calculated assuming a one-subband conduction band. However, most good bulk thermoelectric materials posses significant band degeneracy at the Fermi level.[46] When these multiple subbands are taken into account, the expected increase in power factor with decreasing nanowire diameter is lessened. In fact the power factor actually decreases to around 62% of the bulk value as the nanowire radius is initially decreased. Only when the nanowire diameter approaches significant quantum confinement does the multiple subband model predict power factors similar to the single-subband model.

1.5 Project Goals

The ultimate goal of this project is to develop a thermoelectric with a zT high enough to compete with commercial refrigeration and power generation units. Thermoelectric nanowires appear to be the most promising method to accomplish this goal. To compete effectively with most heat engines though, the synthetic strategy used must be cost effective and scalable. High temperature and high vacuum syntheses, like molecular beam epitaxy used to create the high zT superlattices discussed earlier, most

likely will never reach the mass market because of cost and scalability issues. In addition, the nanowire thermoelectrics developed must be able to fit in the architecture of thermoelectric devices shown in Figure 2.

A promising synthetic method is electrodeposition. Electrodeposition is a cheap, scalable, and widely used process in industry. Many semiconductors and metals have already been plated so there is a wealth of information and research to build upon.[47,48] Electrodeposition also provides excellent control. By tuning variables such as solution concentrations, pH, temperature, additives, and applied potential/current, the process can be optimized. More detailed information on the electrochemical methods used will be found in later chapters.

Porous anodic alumina can be used in combination with electrodeposition to create arrays of nanowires. Alumina, when synthesized in a controlled anodization process, consists of hollow cylindrical pores that run parallel from top to bottom of the alumina. Using the porous alumina as a template, thermoelectric material can be electrodeposited into the pores creating a nanowire/alumina hybrid. This nanowire/alumina hybrid matches well with the geometry required for actual thermoelectric devices. Shown in Figure 6 are two nanowire/alumina hybrids placed into a thermoelectric device. Device efficiencies and also figure of merits can then be measured and compared against other state of the art thermoelectrics.

The two main elements of this thesis are the fabrication of thermoelectric nanowires and the measurement of their thermoelectric properties. Chapters 3, 4, and 5 will present the creation of nanowires through a templated electrodeposition method. The viability of this method for creating thermoelectric nanowires will be thoroughly explored. Chapters 6 and 7 concern the challenges of electrically contacting and measuring the thermoelectric properties of these materials. Measurements on nanowires synthesized will serve as a test for the theoretical predictions presented in this chapter. Measuring the success of these nanowires will also provide guidelines for future work in the field of thermoelectrics. It is still a matter of debate as to whether PGEC bulk materials or one-dimensional nanowires will ultimately produce a high zT thermoelectric.

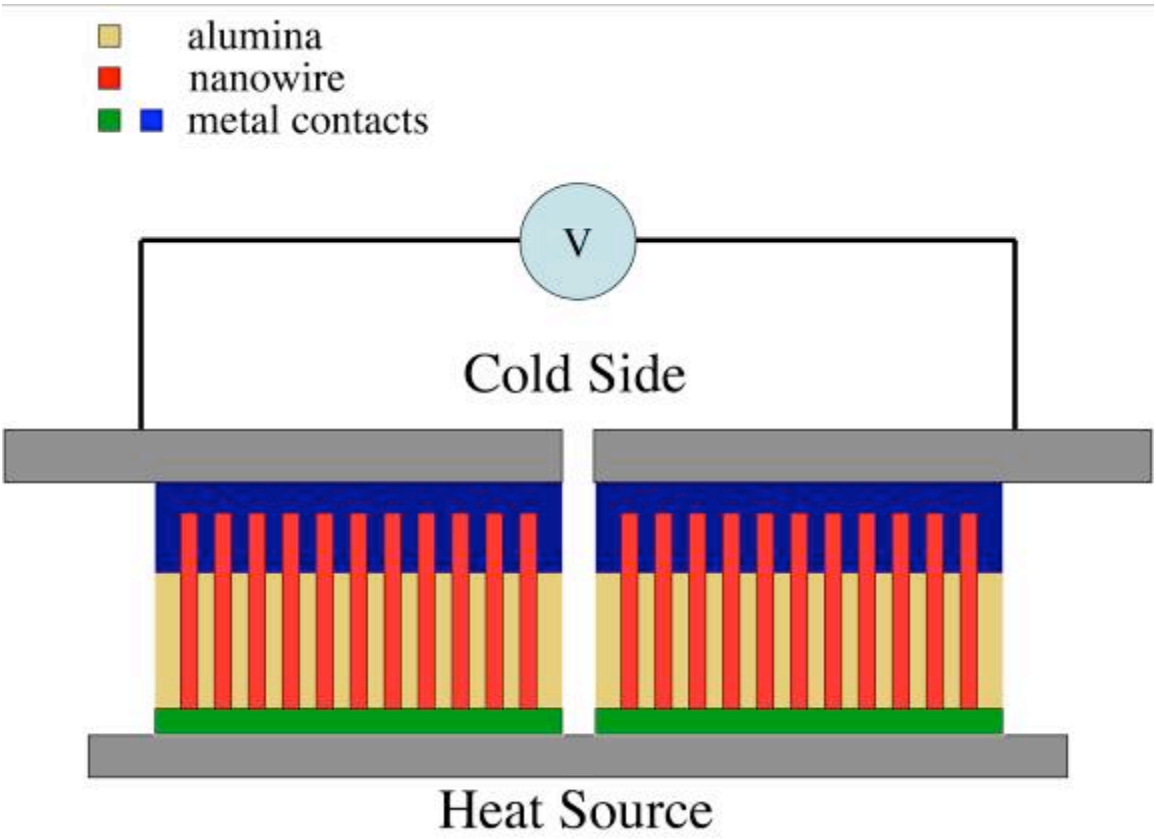

Figure 1-6. Nanowire thermoelectric device

Chapter 2: Methods

This chapter will describe the electrochemical methods used to synthesize porous alumina and the basics of electrochemical depositions.

2.1 Cyclic Voltammetry

Cyclic voltammetry (CV) is the primary method electrochemists use to investigate electrochemical systems. It is a fairly easy experiment to run and can yield plenty of information on the electrochemistry of the system if interpreted correctly. The typical setup for a CV is a 3-electrode cell and is illustrated in Figure 1.

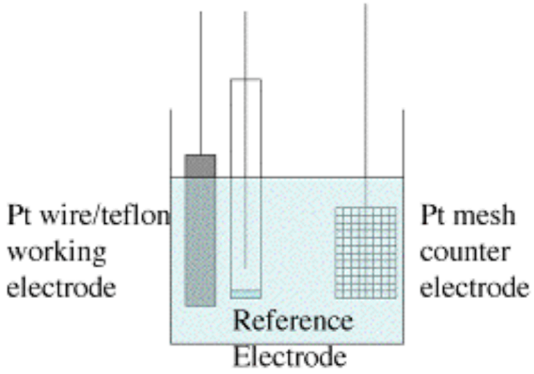

Figure 2-1. CV experimental setup

The 3 electrodes include the working electrode, reference electrode, and the counter electrode. Each electrode serves a particular purpose. The working electrode is the location where the electrochemical events of interest occur. For all the CVs in later chapters, the working electrode is a platinum wire encased in a Teflon insulator so that only a small portion of the wire is exposed to the solution (approximately 1mm^2 disk). The counter electrode completes the electrical circuit. The electrochemical reactions occurring at the counter electrode do not matter as long as they do not become rate limiting. For this reason the counter electrode used for all CVs is a high surface area Pt mesh electrode. The final electrode is the reference electrode. The potential of the working electrode is measured with respect to another redox couple. This redox couple is housed in the reference electrode. To measure the potential of the working electrode accurately, the reference electrode should also remain at constant potential. This type of electrode is termed an ideally nonpolarizable electrode, meaning that the potential of the electrode will only change under a large current. The reference electrode used in all of the future electrochemical experiments is the Ag/AgCl 3M NaCl electrode, using the redox couple Ag/AgCl as the reference. The Ag/AgCl electrode falls under the more general category of reference electrodes, the metal/insoluble salt/ion electrode. Since the activity of the solid Ag and AgCl is 1, the electrode potential can be written as

$$E = E^\circ - RT/F \ln[Cl^-] \qquad (2.1)$$

For a 3M NaCl solution the equilibrium potential of the reference electrode is +0.209 V vs NHE.[49]

During a CV, the potential of the working electrode is swept from a starting potential to a final potential and then back again to the starting potential. The typical potential waveform is shown in Figure 2. While changing the potential of the working electrode, the current is measured and an I-V curve is produced. Also shown in Figure 2 is a typical CV curve of a reversible electrochemical reaction. The qualitative shape of this curve can be fairly easily reasoned. The current is simply a measure of the reaction rate of the electrochemical reaction. Assuming the electrochemical reaction being studied is the couple between M^{3+} and M^{2+}, a negative current corresponds to electrons passing from the electrode to M^{3+} and a positive current indicates that electrons are passing from M^{2+} to the electrode. If we start with a solution of M^{3+} and begin the potential sweep at an oxidizing or anodic (right side of Figure 2) potential there will be negligible current since the potential is not reducing or cathodic enough to reduce the species in solution. As the potential becomes more cathodic the energy of the electrons in the working electrode is raised. Once the electron energy level in the electrode is within k_bT of the equilibrium potential of M^{3+}/M^{2+}, electrons can flow from the electrode to solution reducing M^{3+}. As the potential becomes more cathodic the rate of electron transfer from the electrode to the solution increases until the cathodic peak current, I_{pc}, is reached. At this point all of the M^{3+} near the electrode surface has been reduced to M^{2+}. The current now begins to drop off due to a lack of available M^{3+} at the electrode surface. The reaction is now in the diffusion-limited regime. Reversing the potential sweep at this point will produce the anodic peak shown in Figure 2 for the same reasoning as the cathodic peak. While many CVs are likely to be more complicated, having a qualitative understanding of the simple situation helps in deciphering more complex ones. Changing variables such as concentration, pH, and scanning potentials help to tease out more information from these curves. Ultimately, the purpose of running CVs on plating solutions is to determine the optimal conditions for the electrodeposition.

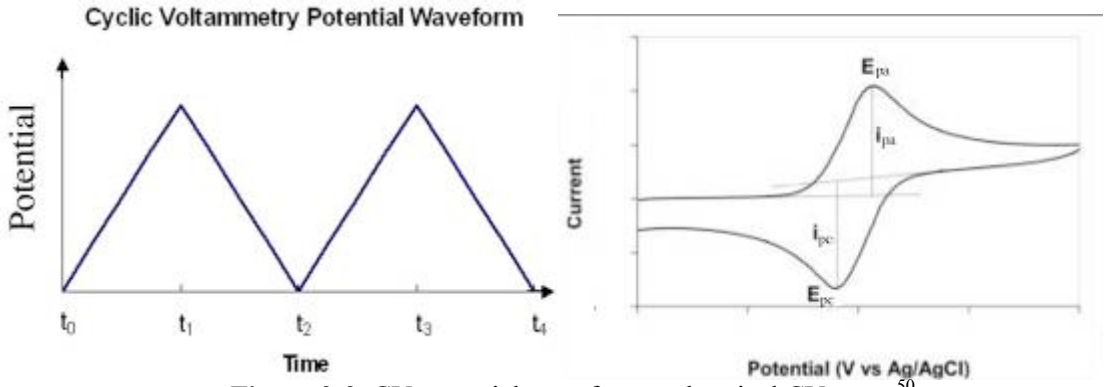

Figure 2-2. CV potential waveform and typical CV curve[50]

2.2 Electrodeposition of Compounds

A majority of this thesis will focus on the electrodeposition of compound semiconductors. It is therefore useful to discuss the principles and challenges of electroplating multi-component systems. While electroplating a single metal can be a very straightforward process, depositing two or more different atoms simultaneously to

form a complex compound is difficult. Both thermodynamic and kinetic considerations play an important role in compound deposition. Differing reduction potentials of the constituent elements in a compound is the major thermodynamic problem with multi-element electrodeposition. Electrochemists typically attempt to work around this issue through adjusting activities and pH values. Kinetics of forming the desired compound also presents a problem. Generally, the only solution to this issue is to raise the temperature of the deposition. A more detailed description of the problems and the solutions to these problems will be presented in this section.

To begin, it is useful to state some of the assumptions that are made in this section. It is also worth noting that the distinction between thermodynamic and kinetic issues in electrochemistry is often vague. This is because when a potential other than the equilibrium potential is applied to a system (an overpotential), it is possible to calculate both the change in equilibrium concentration (thermodynamics) and the expected current density (kinetics), assuming certain parameters are known. The relationship between overpotential and current density is known as the Tafel Equation[49],

$$\eta = (RT/\alpha zF)\ \ln i_0 - (RT/\alpha zF)\ \ln i \qquad (2.2)$$

where η is the overpotential, R is the gas constant, T is the temperature, α is the charge transfer coefficient, z is the number of electrons involved, F is Faraday's constant, i_0 is the exchange current density, and i is the current density. This equation is extremely important for the electrodeposition of compounds. For a compound of a given stoichiometry, for example AB, it is necessary that the rate A is plated be equal to the rate B is plated to achieve the correct ratio of A to B. However, if the reduction potentials of A and B differ, the applied deposition potential will result in two different overpotentials for A and B and therefore two different plating rates, assuming that α, z, and i_0, are similar for the two elements. To determine the validity of this statement it is useful to elaborate on the charge transfer coefficient and the exchange current density. The charge transfer coefficient is a measure of the symmetry of activation barrier and can take values from 0 to 1. However, most electrochemical reactions are symmetrical, and therefore the charge transfer coefficient is typically around 0.5.[49] The exchange current density is the current at zero overpotential. At zero overpotential, there are still cathodic and anodic reactions occurring. The rates of the forward and reverse reactions are merely equal, and the rate at which they occur is the exchange current. The exchange current is therefore a measure of the intrinsic rate of electron transfer from the electrode to the reduced species. The assumption that the exchange current of A and B will be similar is therefore problematic since it is reaction specific. However, for the sake of simplicity, the assumption is made nonetheless.

As already mentioned, one of the biggest difficulties in depositing a binary compound is that the reduction potential of the two atoms can be very different. In the case shown in Figure 3, B has a lower reduction potential than A and is therefore called the more noble species. Because A and B have different reduction potentials, the Tafel equation states they will have different polarization curves, assuming the previously stated issues hold. The ratio of A to B in the deposit will therefore depend on the potential applied. Applying a potential of V_1, as shown in Figure 3, will give a deposit

where the ratio of A to B is equal to j_1/j_2, assuming the same number of electrons are involved in the reduction of A and B.

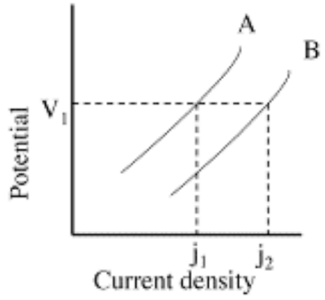

Figure 2-3. Potential versus current curves for A and B adapted from [49]

In this example the amount of B in the deposit will always be greater than A no matter what potential is applied. If the desired compound has a stoichiometry of AB, obtaining a pure phase deposit would be impossible. The large difference in the reduction potential of these two elements must be minimized in order to obtain the compound AB.

One obvious way to adjust the deposition potential of A and B is to alter their activity. The Nernst equation relates the activity of the species in solution to the deposition potential.

$$E = E° + RT/zF \ln a_{ion} \quad (2.3)$$

Therefore, lowering or raising the activity of the ion in solution shifts its deposition potential cathodically or anodically respectively. Tuning the activity opens the possibility of codepositing two elements with different reduction potentials. Adjusting the concentration of the species in the plating solution is one way to tune its activity. Another common method of changing the activity of a species in solution is through a complexing agent. The classic example of this method is the electrodeposition of brass (Cu and Zn). The standard reduction potentials of Cu and Zn are 0.34 V and –0.77 V, respectively. With such a large difference in reduction potentials it is difficult to deposit brass from a solution of just copper and zinc. However, adding KCN to the solution as a complexing agent makes this possible. Both copper and zinc form complexes with cyanide, but copper cyanide is much more stable than zinc cyanide. Therefore, the activity of Cu^+ in solution is shifted by a larger amount than the for Zn^{2+} with no cyanide present. The activities of copper and zinc are changed such that both now have a reduction potential around –1.3 V and can be codeposited.[49]

Tuning the pH of the solution can also, in some cases, be used to adjust the deposition potentials of two elements closer to one another. If the balanced electrochemical deposition reaction includes hydronium or hydroxyl ions, the pH of the solution will affect the reduction potential. The dependence can be calculated from the Nernst equation. For example if n protons are needed to deposit a metal M from a solution M^{z+} the reduction potential is

$$E = E° - n(0.0592)/z \text{ pH} + 0.0592/z \log [M^{z+}] \quad (2.4)$$

Setting the concentration of the metal ion to a constant value and graphing the resulting potential as a function of pH creates what is known as a Pourbaix diagram.[51] Pourbaix diagrams are useful tools for electrochemists since they show the thermodynamically stable species at a given pH and potential. Using a Pourbaix diagram, it is possible to select a pH to deposit a multi-element compound. Assuming, as often can be the case, the number of protons involved in depositing two elements, A and B, differ, then the slope of their potential/pH curves will differ, thereby causing the reduction potential of A and B to be equivalent at some pH as shown in Figure 4. While the red section shows a large range of pH values at which it is possible to deposit both A and B, it is important to point out that if their reduction potentials are very different the ratio of A to B in the deposit can be extreme. It is only near the pH indicated by the dotted line that the amount of A and B in the deposit will be equal, again making the assumptions stated in the beginning of this section.

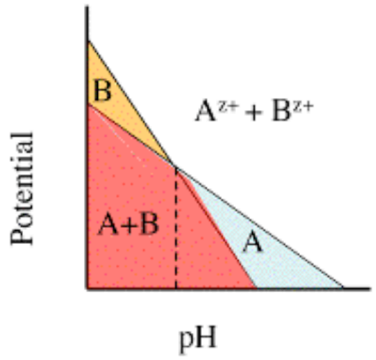

Figure 2-4. Pourbaix diagram of A and B

While in the case of brass, the reduction potentials of Zn and Cu must be made nearly identical to codeposit the two metals, this is not always the case. The allowable difference in reduction potential of the two elements can be as large as the free energy of formation of the compound being formed. Take the generic case of depositing AB from a solution of A and B again. If a potential of V_1 is applied and neglecting the formation of any compounds, B will only be deposited as shown in Figure 4. However, accounting for the formation of AB, A can be underpotentially deposited if the potential difference is less than or equal to the free energy of formation of AB divided by Faraday's constant and the number of electrons needed to reduce A, also shown in Figure 5.

$$\Delta V = \Delta G^\circ_f / zF \tag{2.5}$$

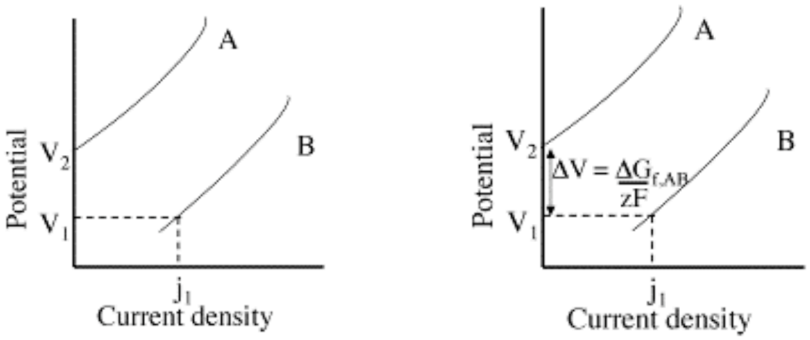

Figure 2-5. Potential versus current curves for deposits with and without AB formation

This equation comes from the fact that the Gibbs free energy can be related to the cell voltage through the following equation

$$\Delta G = -zFE \tag{2.6}$$

The underpotential deposition mechanism is crucial to understanding the deposition of most compounds and will be used to explain the deposition of a variety of materials in this thesis.

All of the previously discussed considerations involved thermodynamic challenges. Kinetic issues can often play as big a role as thermodynamic ones. Creating conditions that cause A and B to be deposited in equal amounts does not guarantee the compound AB will be formed even if it is thermodynamically favorable to do so. Most solid state chemist are already familiar with this problem. High temperature synthetic strategies are often employed to overcome kinetic barriers. Electrochemists are limited, however, in the range of temperatures available by their choice of solvent. Fortunately, however, in the case of electrodeposition, kinetic barriers to phase formation typically are less of an issue, but not unknown.[52]

2.3 Porous Anodic Aluminum

Without porous anodic aluminum (PAA), the synthesis and incorporation of nanowires into thermoelectric devices would not be possible. The remarkable ability of PAA to form well-ordered and uniform nanopores under the right conditions has given researchers a powerful tool for creating nanomaterials. Because of the importance of PAA to this project and the research of nanomaterials in general, a discussion of its history and synthesis is warranted.

The history of anodic aluminum dates all the way back to 1923 when it was commercially used to protect aluminum surfaces.[53] It was not until 1953 that the microstructure of PAA began to be investigated.[54] Over the course of the following decades researchers attempted to pin down the mechanism of the pore formation with one of the leading contenders, the equifield model.[55] There is still some debate in the literature as to the validity of this model and there have been several competing explanations proposed.[56,57] Even without a clear understanding of the pore formation mechanism, Masuda observed that the use of two controlled anodizations greatly improved the uniformity and ordering of the nanopores.[58] This discovery paved the way

for using PAA as a template for nanowires since the uniformity and distribution of nanowires could now be better controlled.[59,60]

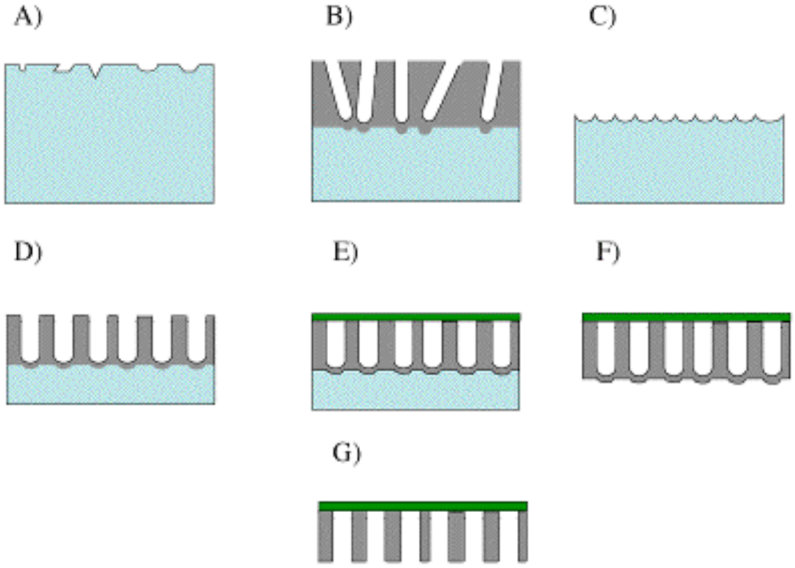

Figure 2-6. Creation of PAA template for nanowire synthesis

Figure 6 shows the creation of a PAA template from start to finish. PAA begins with a piece of pure aluminum foil that is 99.9995% pure and 0.13mm thick. It is cut into the shape of a circle with a tail that is used for the electrical connection. Typically the circle portion that will become the PAA is around 1cm^2 in area. The aluminum is then polished to a mirror finish using 1 micron diamond paste followed by 0.05 micron silica paste. The polishing step removes any large imperfections in the surface, leaving only microscopic defects that are seen in cartoon A. It is at these defects that pore nucleation begins.

Once the aluminum is polished it is electrically oxidized at 40V in a 0.2M oxalic acid solution. This process is called anodization. As mentioned previously, the creation of well-ordered pores requires two separate anodizations. During the first anodization, the aluminum is oxidized to Al_2O_3, also known as alumina (the grey portion in Figure 6). While the alumina is forming, it is at the same time being dissolved by the oxalic acid solution. It is these two effects that lead to the formation of hexagonally arranged nanopores. After an approximately 5 hour first anodization, the aluminum/alumina structure resembles cartoon B. Pores have formed but they are not very well ordered.

The alumina that was formed from the first anodization is then stripped in a chromic acid solution. Chromic acid will dissolve the alumina but leave the aluminum. This etching step leaves a scalloped aluminum surface like the one seen in cartoon C.

The scalloped aluminum is then anodized again in 0.2 M oxalic acid, but this time near 0° C. The second anodization lasts anywhere from 34 to 48 hours depending on the thickness of alumina desired. Shown in cartoon D is the result of the second anodization. Notice now that the pores are uniform and well ordered.

Cartoons E-F depict the process of turning the PAA/aluminum structure into a template for the electrodeposition of nanowires. First, a Pt layer that will serve as the working electrode is sputtered onto the side with open pores (E). Then, the leftover

aluminum is removed with mercuric chloride (F). Finally, the barrier layer of alumina is removed with 10% phosphoric acid leaving open pores for electrodeposition (G). Top-down and cross-section SEM images of a 40 nm PAA template are shown in Figure 7.

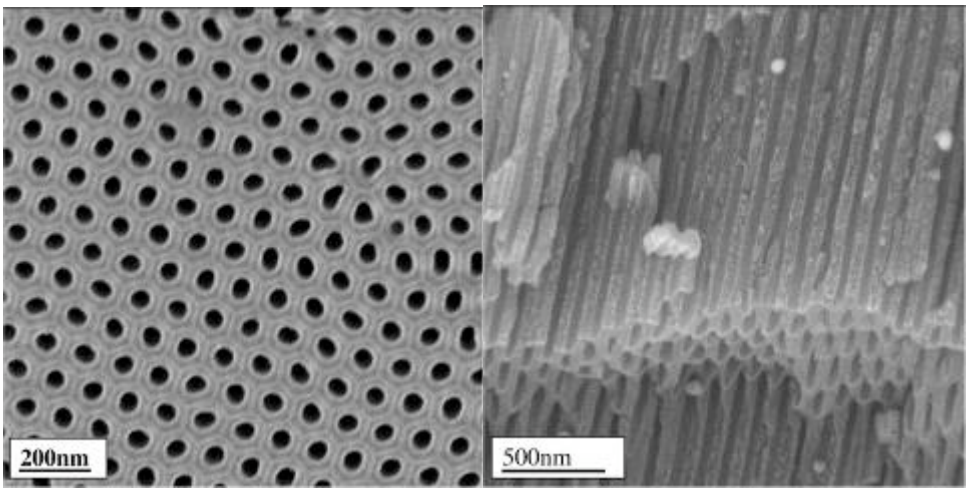

Figure 2-7. SEM of PAA

2.4 Materials Characterization

Topics in the previous sections concerned the general methods used in the fabrication of nanowires. This section will present the various techniques that are used to characterize nanowires once they are created. The nanowire morphology, crystallinity, composition, grain size, lattice parameter, and crystallographic orientation all could have a large effect on thermoelectric properties and require thorough exploration. The characterization methods used to determine these properties include x-ray diffraction (XRD), scanning electron microscopy (SEM), and electron microprobe analysis (EMPA). A brief discussion of these methods will be presented.

By far the most used characterization technique in this thesis is powder XRD. A large amount of information can be collected from a single diffraction pattern. XRD was used to determine the crystallinity, lattice parameter, grain size, and crystallographic orientation of the nanowires. A Siemans D5000 diffractometer with CuKα radiation was used. Entire nanowire samples can easily be mounted on XRD sample holders and used to collect a diffraction pattern. By comparing the measured pattern to computer powder diffraction files (PDF), the compounds deposited can be determined. The intensity of the different diffraction peaks reveals the growth direction of the nanowires. A peak with a higher intensity than predicted by the PDF indicates that the nanowires are oriented in that direction. The lattice parameter of crystal structure can also be calculated from the 2θ angle of a known diffraction peak using the Bragg equation for diffraction. In addition, the grain size can be calculated using the full-width at half maximum of

diffraction peaks from the Debye-Scherrer equation. Because of the considerable amount of information available from XRD, it is an extremely useful technique for characterizing nanowire arrays. In addition, since it is a non-destructive method, samples can be further characterized with other methods or still used for creating thermoelectric devices, adding to the utility of XRD.

The nanoscale morphology of nanowire arrays was studied using a Hitachi S5000 SEM. Samples were routinely examined in three different orientations, i.e. cross section, top-down, and bottom-up. To prevent charging effects samples were sputtered with a thin conductive coating prior to imaging. SEM images of nanowire array cross-sections provided valuable information on the uniformity and lengths of the nanowires. For cross-section images, back-scattered electron micrographs were typically recorded. Using back-scattered electrons, as opposed to secondary electrons, provides contrast based on atomic number and therefore makes viewing heavy element nanowires embedded in an alumina matrix possible. Top-down views of nanowires were used to study nanowire overgrowths and also the diameter of the nanopores. Polishing off the sputtered platinum layer and imaging bottom-up was used to determine the density of nanowires in the PAA template. The importance of knowing the nanowire lengths, morphology, and density for creating devices (all of which will be discussed in chapter 7) makes the SEM a vital tool.

The final crucial technique for characterizing nanowire arrays is EMPA. EMPA is used for accurate determination of the elemental composition of nanowire arrays. To prepare samples for microprobe analysis, the sputtered platinum layer was first removed by polishing. Samples were mounted in a bottom-up orientation and coated with a thin conductive carbon layer to prevent charging. Data was collected at several points along several lines that transverse the sample. These points were used to determine the overall elemental composition and standard deviation. Compared to energy-dispersive x-ray spectroscopy (EDS), another common compositional analysis method, EMPA offers far better accuracy and sensitivity. The high accuracy and sensitivity of EMPA is because it is first calibrated using known standards. Both the accuracy and sensitivity of EMPA is needed in characterizing these thermoelectric nanowires since their electronic properties are strongly affected by small changes in elemental composition.

2.5 Conclusion

Presented in this chapter were the general methods and concepts that are used heavily in later chapters. The foundations of cyclic voltammetry and the electrodeposition of multi-element compounds were established to help the reader better understand the electrochemical data presented in chapters 3, 4, 5, and 8. The specific details of these chapters can all be understood with the principles presented in [2.1] and [2.2]. Found throughout all the chapters are materials characterization techniques briefly presented in [2.4]. The utility of each technique was explained so as to better understand why these methods were employed. In addition, the data available from each technique was described to introduce the reader to information that will be presented throughout the rest of this work

Chapter 3: The Electrodeposition of Stoichiometric Lead Telluride

Up to this point the reader should have noticed that there has been no direct mention of the particular material to be investigated. This omission was intentional and designed to display the versatility of this approach to produce high efficiency thermoelectrics. Any material that can be electrodeposited can be substituted and then investigated with this method. Additionally, the application of the nanowires does not have to be limited to thermoelectrics. In the following chapters, a strong case will be presented for why PbTe and several thallium chalcogenides nanowires should be investigated for thermoelectric applications. The electrochemical growth of these materials will also be thoroughly discussed. The conditions that lead to the electrodeposition of stoichiometric pure phase PbTe nanowires in porous anodic alumina with 40nm pores will be presented in this chapter. The PbTe nanowires can be grown with extremely uniform lengths and high aspect ratios, which are important for practical device incorporation.

3.1 PbTe Thermoelectrics

Lead chalcogenides have a long history of being investigated for thermoelectric applications. Thomas Johann Seebeck was the first to observe the high thermoelectric power of PbS in 1822. Joseph Stefan in 1865 observed the thermoelectric power of different samples of natural PbS could switch signs depending on the carrier type. A. F. Ioffe beginning in 1928 started investigating PbTe as a possible thermoelectric material.[61] Much of the basic properties of PbTe were investigated and published in the 1950's and 1960's.[62] Research into PbTe ultimately led to the "world's first atomic battery" (a.k.a. a RTG) in 1959.[63] Pictured in Figure 1 is President Eisenhower observing the first RTG based on PbTe technology. Applications for PbTe based generators were quickly found by the US army and NASA.[64,65,66] The new Mars Science Laboratory is continuing the tradition of using PbTe based RTGs to power its rover.[16] The widespread use of PbTe means that a vast body of literature has already been collected on its properties. Being able to draw upon these resources greatly increases the odds of understanding the properties of PbTe nanowires, thus making PbTe a good choice for investigation. The following paragraphs contain a brief summary of the important properties of PbTe.

Figure 3-1. President Eisenhower admiring a PbTe RTG[67]

PbTe has a NaCl structure type, with tellurium forming a face-centered cubic lattice and lead filling all of the octahedral holes. The lattice parameter of PbTe is 6.46 Å.[62] Based on the radius ratio rule and the ionic radii of Pb^{2+} (133 pm) and Te^{2-} (207 pm) NaCl is the predicted structure type.[68]

The chemical bonding in PbTe is best described as a mixture of ionic and covalent. The crystal structure and lattice parameter data matches well with an ionic model. In addition, the large difference between the high frequency (33) and static (414) dielectric permittivity values supports an ionic bonding model.[63] However, the small difference in the electronegativities of Pb and Te would seem to suggest covalent bonding.[69] Studies on carrier scattering in PbTe support the idea of covalent bonding.[63] Based on the contradictory evidence, bonding is typically viewed as mixed ionic-covalent. The mixed ionic-covalent bonding is responsible for some of the superior thermoelectric properties.

PbTe is a narrow gap semiconductor with a band gap of 0.32eV at room temperature.[70] Because of the covalent nature of bonding in PbTe the measured carrier mobilities can be quite high. With low carrier concentrations, the mobility of electrons and holes can approach 1.73 and 0.84 x 10^3 $cm^2V^{-1}s^{-1}$ respectively.[71] The high carrier mobility means the electrical conductivity of PbTe can be on the order of 10^4 to 10^5 S/m.[72] Depending on the carrier concentration and type, the Seebeck coefficient can range from around 300 to –300 μvK^{-1}.[73]

The large atomic weight and the ionic nature of the bonding in PbTe lead to the observed low lattice thermal conductivity. At room temperature the lattice thermal conductivity of PbTe is 2.0 $Wm^{-1}K^{-1}$.[73] At the higher temperatures where PbTe is

typically used, the lattice thermal conductivity drops to close to 1 $Wm^{-1}K^{-1}$ due to increased Umklapp scattering of phonons.

The combination of low thermal conductivity, high Seebeck coefficient, and high electrical conductivity gives PbTe one of the highest zTs. Shown in Figure 2 are the zTs of common thermoelectrics and how they compare to PbTe. From 200 ° to 500 °C PbTe outperforms all other thermoelectric materials. Choosing to make nanowires of PbTe, which already has a high zT, increases the likelihood of achieving zTs in the range of 3-4 since only a modest improvement is needed.

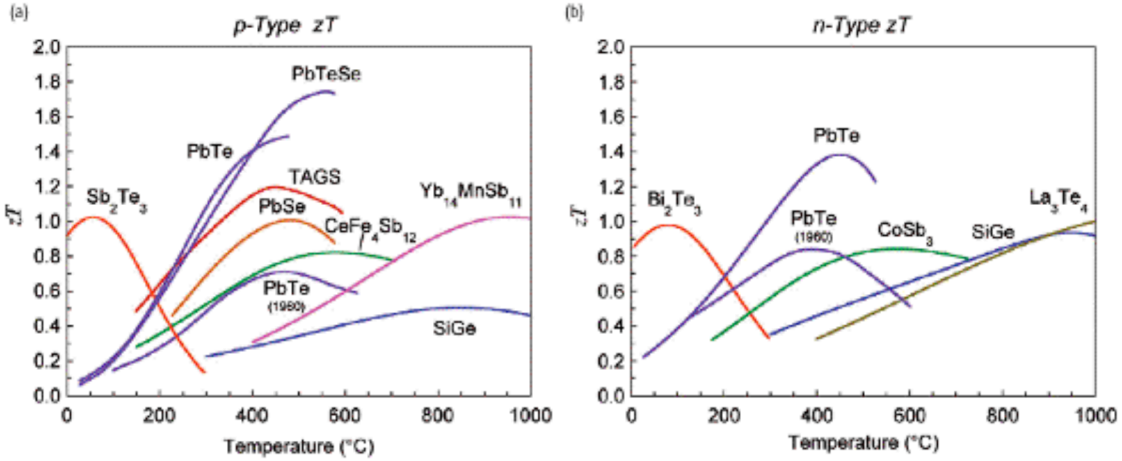

Figure 3-2. zTs of thermoelectric materials[67]

In order for the proposed method of creating high zT thermoelectrics by electrodeposition into PAA to be successful, quantum confinement needs to occur in the size regime of the nanopores in PAA (22-40 nm). For example, theory predicts that the zT of Bi_2Te_3 will not increase due to quantum confinement effects until below 5 nm.[37] Currently this critical size dimension is unachievable through PAA templating. While improvements in the zT of 40 nm Bi_2Te_3 are still possible, this would all come from a reduction in thermal conductivity and not an increased power factor. Obviously, selecting a material that can exhibit quantum confinement in the 22 to 40 nm limit set by PAA is very important.

An easily calculated value called the Bohr exciton radius is a quick estimate to determine when a material will exhibit quantum confinement. An exciton is an excited electron-hole pair that is bound through Coloumb forces. The electron-hole pair can be thought of as a simple atom, like the hydrogen atom. The lowest energy level of the exciton can be calculated from a Bohr model of an atom. The Bohr exciton radius is simply the smallest allowable radius in the hypothetical atom. The radius can be calculated from

$$R = \varepsilon h^2/4\pi^2 e^2 (1/m_e + 1/m_h) \qquad (3.1)$$

where ε is the dielectric constant, h is Plank's constant, e is the charge of an electron, and m_e and m_h are the effective mass of the hole and electron. Shown in Table 1 are the Bohr exciton radii of several semiconductors.

Semiconductor	R (nm) [74,75]
Si	4.9
Ge	17.7
GaAs	11.3
CdSe	5.2
PbS	20
InAs	34
PbSe	46
InSb	54
PbTe	116

Table 3-1. Bohr exciton radii of several semiconductors

Because of the low effective mass and high dielectric constant of PbTe, it has one of the largest Bohr exciton radii of all materials. Based on this calculation it should be possible, even given the limitations of PAA, to create quantum confined wires of PbTe.

To summarize, PbTe is an excellent candidate to investigate for nanowire thermoelectric applications. It is already being used in many thermoelectric applications and many of its properties have already been studied. Of all common thermoelectrics, PbTe has the highest zT in the mid to high temperature range. The expected increase in zT should also occur at the dimensions being studied given the large Bohr exciton radius.

3.2 Previous PbTe Electrochemical Studies

While the first report of the electrodeposition of PbTe was in 1976, it was not until more recently that the electrodeposition began to be studied in depth.[76,77] Variables such as the deposition potential, precursor concentration, substrate, and solution pH have all been investigated.[78,79,80,81,82] It was observed that thin films of PbTe could be deposited from both alkaline and acidic solutions. Substrates of indium tin oxide (ITO), InP, Cu, n-Si (100), Au, and Pt have all been used to deposit PbTe. The electrodeposition mechanism appears to be the same regardless of the pH or substrate used. PbTe is deposited through an underpotential deposition mechanism.[76,81] Tellurium, the more noble species, is first deposited and then lead is underpotentially deposited due to the free energy of formation of PbTe.

There are still many challenges to the electrochemical growth of PbTe despite the many reports of its deposition. Generally the films of PbTe produced have an excess of tellurium. A mixture of PbTe and Te would end up lowering some of the positive thermoelectric properties of pure PbTe. The reason for the excess of tellurium is the fact that the reduction potentials of Pb and Te in aqueous solution are very far apart (Pb, -0.13 V vs NHE; Te, +0.551 V vs NHE). Recall the discussion in [2.2] on the difficulties of codepositing a compound made of elements with very different reduction potentials. A problem for the electrodeposition into PAA, but not necessarily thin films, is the acidic or basic solution required. Tellurium is extremely insoluble in water unless very acidic or basic solutions are used. However, the PAA template used for creating the nanowires dissolves in strong acids and bases. A way around this problem used by this lab in other

systems has been to lower the deposition temperature.[83] At lower temperatures the dissolution of PAA is significantly slowed. However, it is unclear how lowering the temperature would affect the deposition of PbTe since it has never been examined.

While there has been a lot of work done on the electrodeposition of thin films of PbTe, there was only one published report of the electrodeposition of PbTe nanowires at the start of this investigation.[84] However, the claims of this report, according to this author's opinion, are possibly exaggerated based on the findings of thin film work and work presented in this thesis. Very recently there have been a few additional reports of electrodeposited PbTe nanowires.[85,86,87,88] These investigations, however, were focused more on single wire measurements than on nanowire arrays. The limited information on the topic of electrodeposited PbTe nanowires demonstrates there is a clear need for further investigation. In addition to the objective of producing high zT nanowires, another goal of this work is to add to the understanding of the electrodeposition of PbTe nanowires and address some of the problems remaining with thin film growth.

3.3 Electrodeposition of Te-rich PbTe

Before beginning any electrochemical investigation it is very important to run a series of cyclic voltammograms (CVs). While much of the information presented in this section can already be found in the literature, it is valuable to present again since it will elucidate later sections.

Shown in Figure 3 is the CV of a solution of 5mM TeO_2 dissolved in 1 M HNO_3. The first reduction wave ($E_{pc} \sim -160$ mV) corresponds to the deposition of pure tellurium and can be assigned as follows:

$$HTeO_2^+ + 3H^+ + 4e^- \Rightarrow Te + 2H_2O \quad (3.2)$$

At more negative potentials, a second reduction wave ($E_{pc} \sim -700$ mV) is observed. Previous work identified this wave as the reduction of $HTeO_2^+$ to $H_2Te_{(aq)}$. The $H_2Te_{(aq)}$ immediately reacts to form pure tellurium through the following mechanism.[89,90,91]

$$HTeO_2^+ + 5H^+ + 6e^- \Rightarrow H_2Te + 2H_2O \quad (3.3)$$
$$H_2Te + HTeO_2^+ \Rightarrow 3Te + 2H_2O + H^+ \quad (3.4)$$

One anodic peak can be observed ($E_{pc} \sim 540$ mV) which is believed to be the stripping of deposited tellurium. This observation is consistent with the conclusion that both reduction peaks result in the production of tellurium. This CV is in good agreement with previous reports on the electrochemical behavior of tellurium in acid solutions.[89,92]

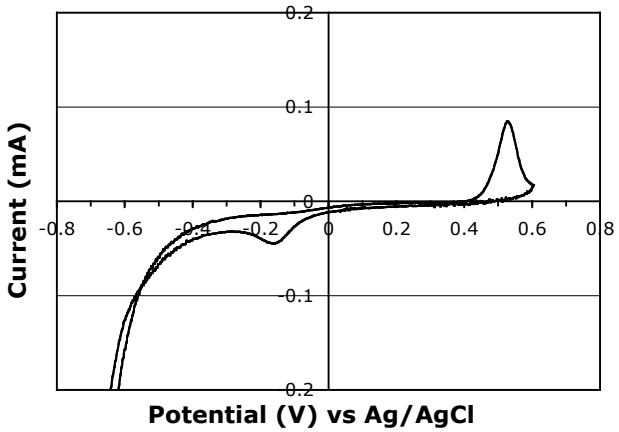

Figure 3-3. CV of Te, reference electrode Ag/AgCl (3M NaCl), scan rate 10mV/s

Shown in Figure 4 is the CV of a solution of 50 mM $Pb(NO_3)_2$ in 1 M HNO_3. In the CV there is one cathodic and one anodic peak corresponding to the deposition and stripping of Pb. The reduction peak beginning sharply at –460 mV is the plating of Pb.

$$Pb^{2+} + 2e^- \Rightarrow Pb \qquad (3.5)$$

An equally sharp stripping peak is also observed beginning around –440 mV.

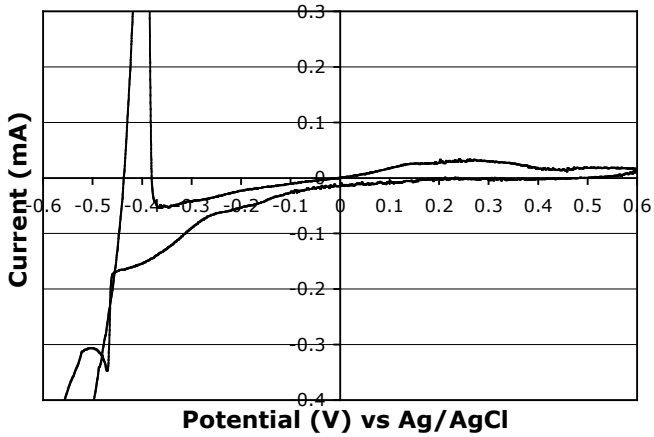

Figure 3-4. CV of Pb, reference electrode Ag/AgCl (3M NaCl), scan rate 10 mV/s

Shown in Figure 5 is one scan of a CV of a 50 mM $Pb(NO_3)_2$, 5 mM TeO_2, 1 M HNO_3 solution. Qualitatively the shape of this CV is very similar to the combination of the CVs shown in Figures 3 and 4. The two reduction peaks in the forward scan are at approximately the same potential where tellurium and lead plated in their individual solutions. The same can be said for the stripping peaks. Based on this information one would expect the first reduction peak to correspond to tellurium deposition and the second peak to lead deposition. However, x-ray diffraction of the deposit at the first reduction peak does not indicate tellurium, but rather PbTe. The reason that PbTe is deposited at this potential is due to an underpotential deposition mechanism. The overall mechanism can be written as

$$HTeO_2^+ + 3H^+ + 4e^- \Rightarrow Te + 2H_2O \quad (3.6)$$

$$Pb^{2+} + Te + 2e^- \Rightarrow PbTe \quad (3.7)$$

Tellurium is first deposited and then Pb^{2+} is underpotentially deposited onto the tellurium due to the free energy of formation of PbTe ($\Delta G°_{f,PbTe}$ = -69.5 kJ/mol).[93] The shift in reduction potential of Pb^{2+} caused by forming PbTe can be calculated to be 360 mV. Since the reduction potentials of Pb and Te differ by roughly this value, PbTe can be plated at around –170 mV vs Ag/AgCl.

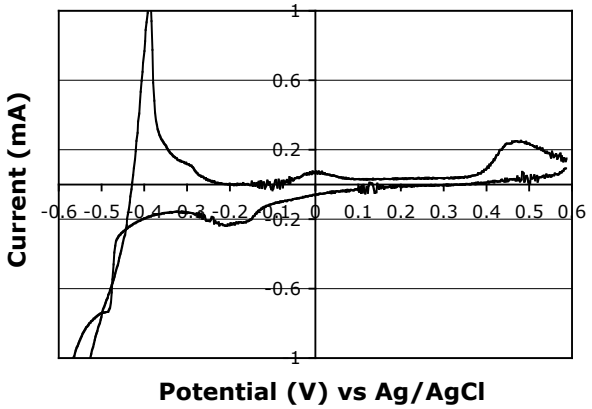

Figure 3-5. CV of Pb and Te, reference electrode Ag/AgCl (3M NaCl), scan rate 10 mV/s

Starting with the initial report in the literature on electrodeposition of PbTe nanowires and the results of the CVs of Pb and Te, attempts were made at deposition of nanowires of PbTe. Reproducing the findings in the literature proved challenging however. Using the solution concentrations given in the reference 84 (50 mM $Pb(NO_3)_3$, 50 mM Te) only Te nanowires were deposited. Reducing the starting tellurium concentration to 1 mM did show improvement, but x-ray diffraction (XRD) analyses on even these nanowire arrays showed elemental tellurium in addition to PbTe. Shown in Figure 6 is a typical XRD of a nanowire array of PbTe with Te inclusions. Recall that the problem of excess Te is not unique to nanowires, but has also occurred in thin films. Since excess Te was also observed in thin films, it is likely that kinetic issues relating to diffusion down the pores of the alumina template are not the cause of the excess Te. Additionally, the diffusion coefficients of the Pb^{2+} and $HTeO_2^+$ in aqueous solutions are approximately the same value (Pb^{2+} 1 x 10^{-5} cm^2/s; $HTeO_2^+$ 0.65 x 10^{-5} cm^2/s),[94,95] meaning each ion should be replenished at similar rates. The culprit must then be the widely differing reduction potentials. From the discussion in [2.2] there are two main remedies to this problem, adjust the activity (lower concentration or complexing agent) or adjust the pH. The limited solubility of Te in more neutral solutions eliminates the possibility of tuning the pH. Adjusting the activity through further reducing the starting concentration of Te is not possible since at these low concentrations the Te in solution will be completely depleted over the course of the deposition. The last remaining possibility is to find a complexing agent that will shift the reduction potential of Te more

negative. If an appropriate complexing agent can be found depositing nanowires of only PbTe becomes more likely.

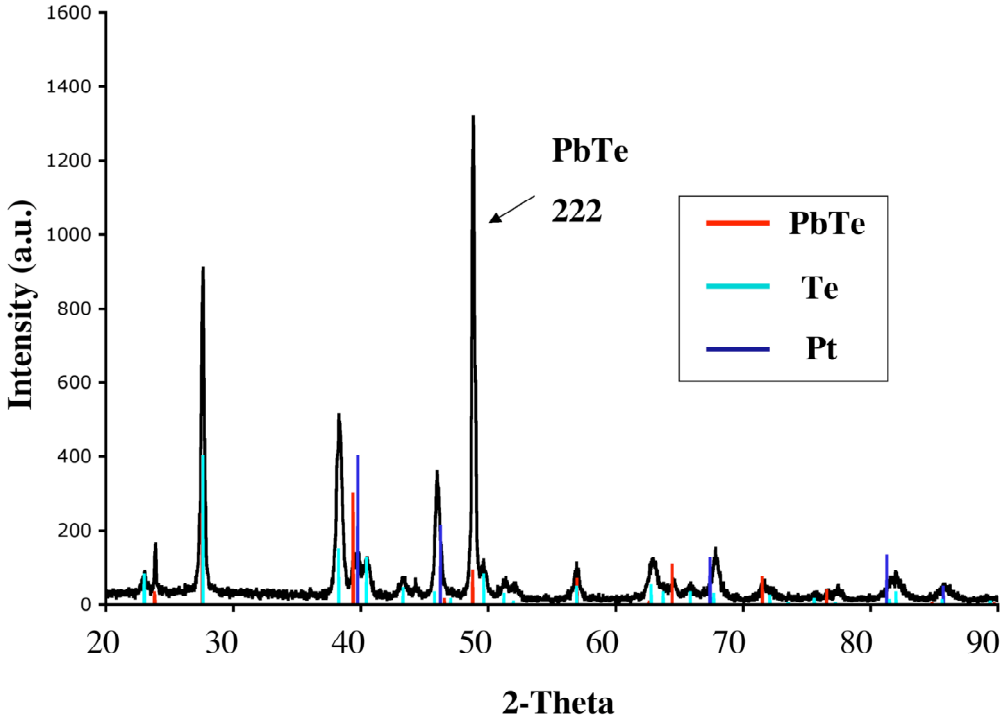

Figure 3-6. XRD of PbTe nanowire array with Te inclusions

3.4 Electrodeposition of Stoichiometric PbTe with a Complexing Agent

The ideal complexing agent will shift the reduction potential of $HTeO_2^+$ more negative but not affect the reduction potential of Pb^{2+}. A good place to begin searching for a complexing agent that has these properties is the common organic acids. Aspartic acid, ascorbic acid, maleic acid, alanine, acetic acid and citric acid were all screened as possible complexing agents. Of these acids only citric acid was found to have the desired properties.

Citric acid has been used as a complexing agent in various other electrodepositions. For example, citrate has been used successfully as a complexing agent in depositions involving either antimony[96] or selenium[97]. Similarly citrate has the ability to act as a complexing agent for tellurium, reducing its effective concentration and shifting its reduction potential more negative. The addition of citric acid has already been shown to reduce excess tellurium in ZnTe deposits by shifting the reduction potential of tellurium.[98]

In addition to a change in reduction potential, citrate increases the solubility of tellurium from about 10^{-5} M to 10^{-2} M at pH = 3.[99] Citric acid thus allows for adjusting the pH to a more neutral value, while maintaining Te concentrations at reasonable levels. This has the effect of further reducing the difference in reduction potential between Pb and Te since tellurium requires $3H^+$ to be reduced while lead requires none.

There have been only a few studies on the nature of tellurium-citrate complex formed in solution. The first report of a tellurium-citrate compound occurred in 1919.[100]

Based on the percentage of tellurium in crystals collected, the compound was determined to have the formula $Te(HC_6H_5O_7)_2$. This formula corresponds to tellurium in the 4+ oxidation state, equivalent to the oxidation state in aqueous nitric acid solutions. An illustration of the proposed complex is shown in Figure 7.

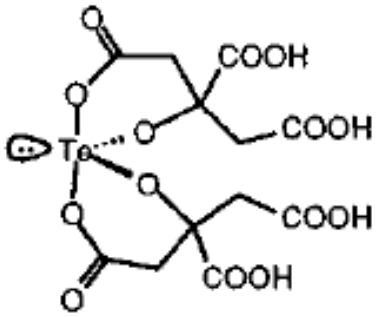

Figure 3-7. Tellurium(citrate)$_2$ complex[101]

The effect of citric acid on the reduction of Pb^{2+} (A) and the reduction of TeO_2 (B) is seen in Figure 8. The concentration of $Pb(NO_3)_2$ and TeO_2 are kept constant throughout the experiments. In the CV with citric acid, 0.25 M H_3Cit and 0.25 M K_3Cit were added and the pH of solution was adjusted to 1 with HNO_3. In the case where citric acid was not added the pH, was adjusted to near 0 with HNO_3 in order to keep the tellurium soluble. Examining Figure 8a reveals that citrate has no affect on the deposition potential of Pb^{2+}. However, in the case of Te (Figure 8b), a noticeable cathodic shift of nearly 200 mV is observed. Using the Nernst equation, the change in pH, and the original tellurium concentration, the activity of $HTeO_2^+$ in the citrate solution can be calculated.

$$\Delta E = E_{Te,cit} - E_{HTeO_2^+} = -n/z\ (0.0592)\ \Delta pH + 0.0592/z\ \log([Te_{cit}]) - 0.0592/z\ \log[HTeO_2^+] \quad (3.8)$$

Plugging in ΔE = 200 mV, n = 3 (number of protons), z = 4 (number of electrons), and $[HTeO_2^+]$ = 5 mM, a value of $[Te_{cit}] = 1.4 \times 10^{-13}$ is calculated. Therefore nearly all of the tellurium in solution is complexed by citric acid leading to the large shift in the reduction potential. Since the deposition potential of Pb remains unchanged, the reduction of Te and Pb are brought closer together in potential, which should improve the composition of the deposit.

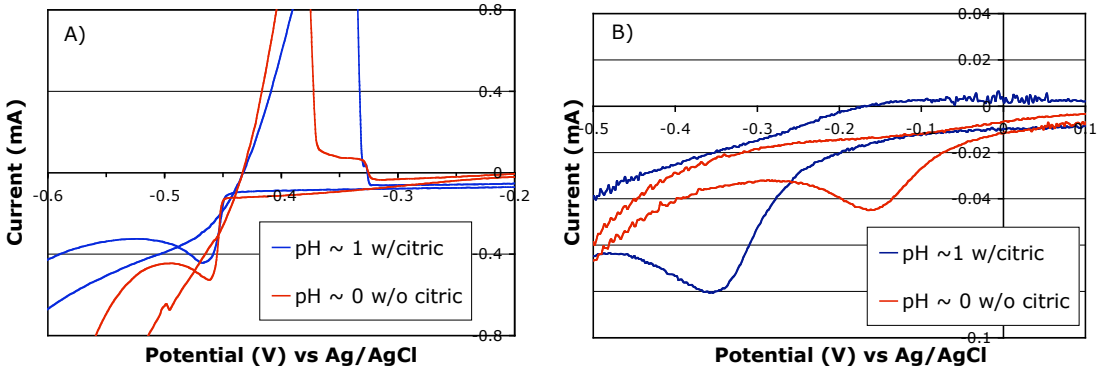

Figure 3-8. CVs of $Pb(NO_3)_2$(A)/TeO_2(B) with and without citric acid, reference electrode Ag/AgCl (3M NaCl), scan rate 10 mV/s

Depositing nanowires from solutions with citric acid in fact does yield more stoichiometric PbTe. The best nanowire arrays were grown using a pulsed current deposition (-0.15 mA/cm^2 2 seconds, 0 mA/cm^2 4 seconds) at near 0 °C over the course of approximately 40 hours. A rest pulse allows ions to diffuse down the pores and has been shown to improve wire uniformity.[83] Shown in Figure 9 is the XRD pattern of an array of PbTe nanowires grown using this method with the addition of citric acid. The Te peaks have vanished and the PbTe peaks have intensified. Based on the strength of the (111) and (222) peak compared to the other possible reflections, it is clear the nanowires grow in the (111) direction. Wire growth in the (111) direction is consistent with underpotential deposition mechanism. The (111) planes of PbTe consist entirely of either Pb atoms or Te atoms, meaning the nanowire must grow layer by layer. Recall that in order to deposit PbTe, a layer of Te must first be deposited, and then onto this layer Pb is underpotentially deposited forming PbTe oriented in the (111) direction

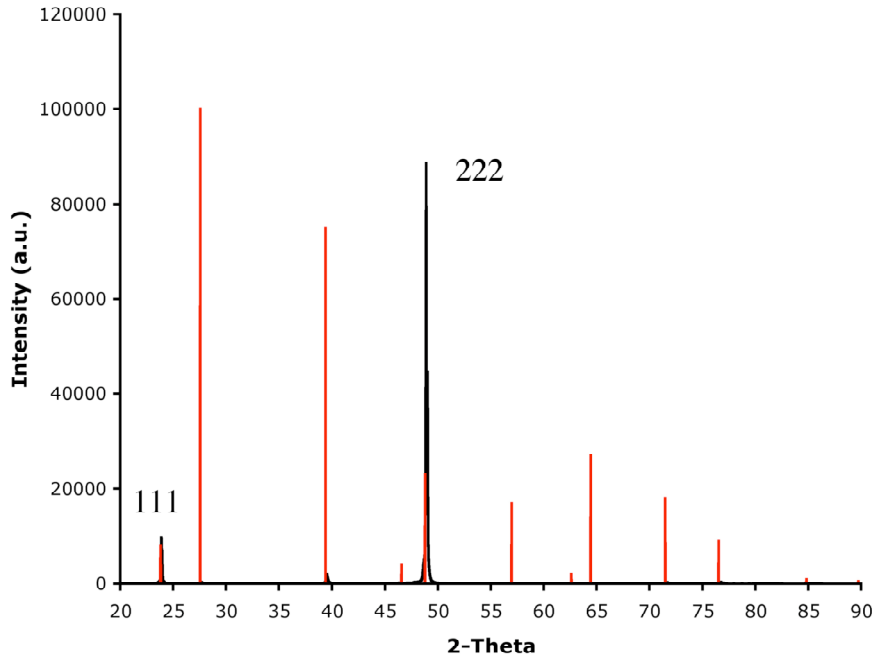

Figure 3-9. XRD of pure PbTe nanowires

Polishing off the platinum working electrode reveals the filling of the PbTe nanowires in the PAA template. The backscattered SEM image can be seen in Figure 10. The bright spots are the pores filled with PbTe. The SEM illustrates the high degree of pore filling, which is beneficial for actual device incorporation. Additionally, when the Pt is polished off, electron microprobe can be used to determine the elemental composition of the nanowires. The tellurium to lead ratio was found to be spot on for stoichiometric PbTe, 1.00 +/- 0.015.

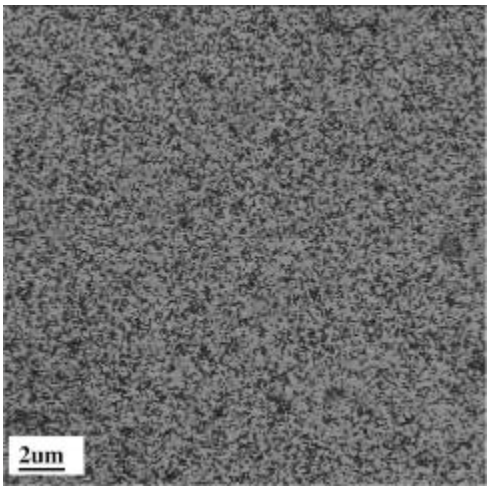

Figure 3-10. Backscattered SEM showing nanowire filling

One of the crucial requirements for incorporation of these nanowire arrays into a device is uniform wire lengths.[83,102] Electrical contacts need to be made to all 10^{10} nanowires/cm^2 in order to have good electrical conductivity across the thermoelectric device. Contacting nanowires of varying lengths is infinitely more complicated than wires of uniform length. A detailed discussion of the methods and challenges of contacting the nanowires will be discussed in a later chapter. Shown in Figure 11 is the backscattered SEM image of a cross section of a nanowire array. In addition to depositing stoichiometric crystalline PbTe with a high degree of filling, the nanowires were all roughly uniform in length. By controlling the total time for the deposition, the nanowires can be grown right up to the top of the PAA template. The nanowires in Figure 11 nearly reach the top of the template with only a small portion of unfilled alumina visible (the small dark portion at the top of the white arrow).

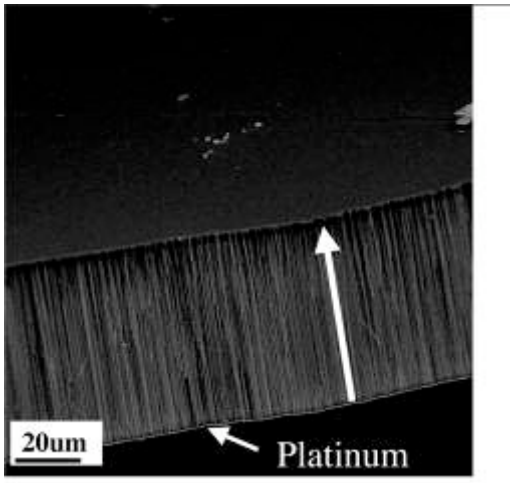

Figure 3-11. Cross section backscattered SEM of nanowire array

3.5 Conclusions

Previous electrochemical depositions of PbTe have all been rich in tellurium caused by the large difference in reduction potentials of Pb and Te. This finding was also observed in initial attempts at electrodepositing PbTe nanowires. By using citric acid as a complexing agent for Te, the deposition potentials of Pb and Te can be brought closer together. Nanowires of PbTe grown from a citric acid solution are stoichiometrically pure PbTe. The density and uniformity of these nanowires are also ideal for future device integration.

Chapter 4: Electrodeposition of Group III Doped PbTe Nanowires

In order to have a working thermoelectric device both an n-type and p-type semiconductor are required. The PbTe nanowire arrays described in the previous chapter would not be very useful if they could not be appropriately matched with a nanowire array of opposite carrier type. Being able to synthesize both n-type and p-type PbTe is crucial towards the goal of creating a working nanowire thermoelectric device.

One benefit of PbTe is that it can be doped both n-type and p-type. The group III elements, In and Tl, can act as donors and acceptors, respectively, in PbTe. These elements, when added to the plating solution of PbTe, can be incorporated into the nanowires to create doped PbTe nanowire arrays in a controlled fashion. The concentration of indium and thallium dopant atoms in PbTe can be quantified through electron microprobe and correlated to the solution concentration of the respective dopant. As described further below, lattice parameters determined by x-ray diffraction (XRD) of the as deposited and post-annealed wires indicate the dopant is being incorporated into the lattice without any phase segregation. A possible mechanism of electrochemical incorporation will be discussed.

4.1 Intrinsically Doped PbTe

PbTe is generally considered a line compound. However, a closer inspection of the phase diagram, shown in Figure 1, reveals that slightly off stoichiometric PbTe is stable. At the widest point in the phase diagram, PbTe can be slightly Te rich (50.014 at. % Te) or Pb rich (49.999 at. % Te). The deviations in stoichiometry are the result of native defects in the PbTe structure. Te-rich PbTe is due to Pb vacancies, while Pb-rich PbTe to Te vacancies.[72] These intrinsic defects can act as either donors or acceptors. Tellurium vacancies in Pb-rich PbTe act as donors creating an n-type semiconductor, while lead vacancies in Te-rich PbTe act as acceptors creating a p-type semiconductor.[72] Shown in Figure 2 are the carrier concentration limits of slightly off stoichiometric PbTe. Hole concentrations can approach around 10^{18} cm^{-3}, while electrons 10^{19} cm^{-3}.

Controlling the defect type and concentration is a common way researchers create n and p type PbTe. Extending this method to PbTe nanowires seems practically impossible however. The level of precision in stoichiometry needed (around +0.014 or –0.001 at. % Te) is not achievable through electrochemical means. Even if it were possible, the maximum carrier concentrations fall slightly below the optimal doping range for thermoelectrics.[19] Therefore, other doping methods must be considered.

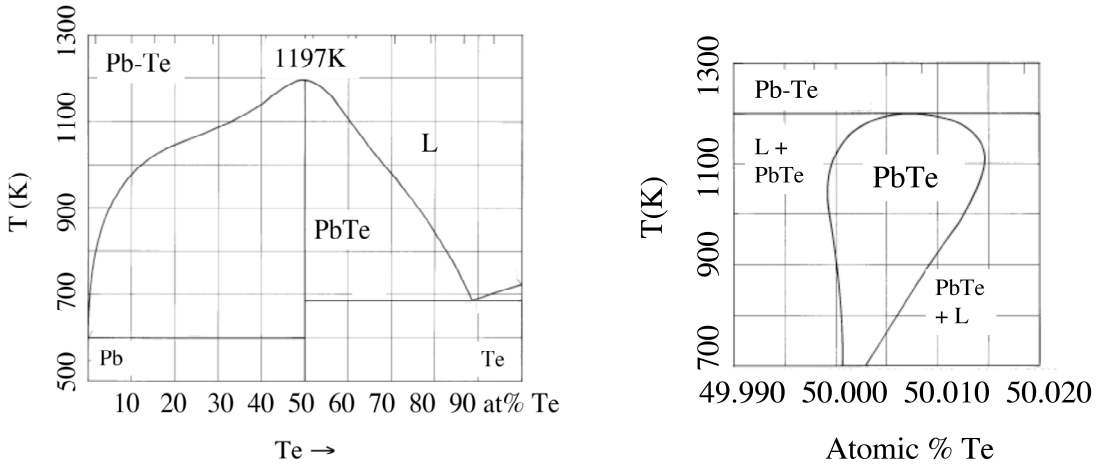

Figure 4-1. Phase diagram of PbTe[103]

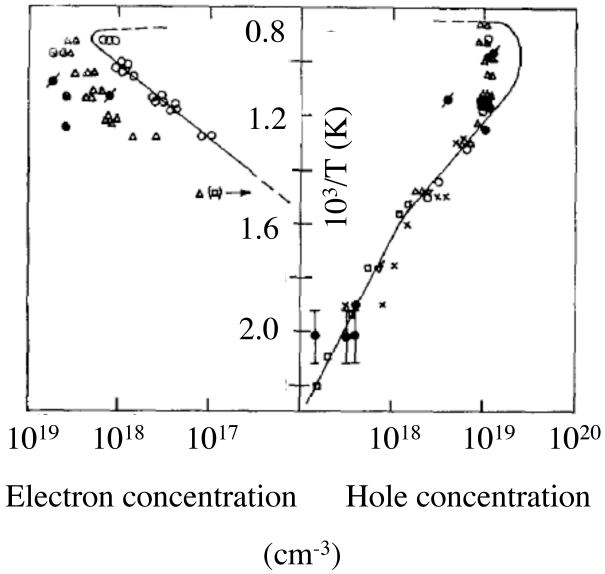

Figure 4-2. Carrier concentration limit of intrinsic PbTe[104]

4.2 Extrinsically Doped PbTe

To reach the higher carrier concentrations needed for thermoelectric materials PbTe is often doped with impurities. Impurity doping can also provide better tuning of the carrier concentration than defect doped samples.

The most common n-type dopants in PbTe are halogens. $PbCl_2$, $PbBr_2$, and PbI_2 are used to introduce the halogen donor into PbTe. The halogen ends up replacing a tellurium atom in PbTe, and since the halogen has one extra valence electron compared to tellurium an electron is promoted to the conduction band. Carrier concentrations of PbTe doped with a halogen can reach 1-2 x 10^{20} cm^{-3}.[61]

P-type dopants in PbTe are commonly alkali metals (mostly Na or K). Alkali metal impurities replace a lead atom in PbTe, and since they are only able to donate one

electron to tellurium, compared to the two electrons of Pb, alkali metal impurities produce holes in the valence band. Carrier concentrations of PbTe doped with alkali metals can reach 1.5 x 10^{20} cm^{-3}.[61]

Synthesizing PbTe doped with these common acceptors and donors through electrochemistry however would present a real challenge. The reduction potential of the alkali metals is far beyond that of PbTe and also the aqueous solvent window. Similarly, incorporating a halogen into PbTe through electrochemistry is unlikely since the halogens are typically electrochemically inactive due to the stability of the halide anion. Even if it were possible to electrodeposit halogen doped PbTe, adding a halogen to the deposition solution would cause all of the Pb^{2+} in solution to precipitate due to the insoluble nature of $PbCl_2$, $PbBr_2$, and PbI_2.

Group III doping, particularly In and Tl, represents the best solution to producing electrochemically synthesized doped PbTe nanowires. Group III impurities have been shown to dope PbTe either n-type or p-type depending on the element. Additionally, and perhaps most importantly, the reduction potentials of thallium and indium are close enough to PbTe to not limit their usefulness. Tl^{+} and In^{3+} are both plated at –0.34 V vs NHE compared to –0.13 V vs NHE for Pb^{2+}.

Indium acts as a donor impurity in PbTe. Indium doped PbTe has a figure of merit comparable to the best iodine doped n-type PbTe. An interesting effect of indium doping in PbTe is Fermi level pinning. At indium concentrations above 0.1 at. %[105] (or 2 at. %[106], there is disagreement in the literature) the carrier concentration is fixed at around 5 x 10^{19} cm^{-3}. Additional indium doping has no effect on the carrier concentration.

Thallium on the other hand acts as an acceptor in PbTe. Recently, thallium doped PbTe has even been shown to have the highest figure of merit of all p-doped PbTe samples.[35] The increase in the figure of merit is due to thallium increasing the density of states at the Fermi level as previously mentioned.

As an aside, the donor and acceptor nature of indium and thallium can be rationalized in the following manner. Both indium and thallium substitute for Pb in the PbTe lattice. Because of relativistic effects in thallium, its 6s electrons are much lower in energy than its 6p electron. Thallium is therefore only able to donate the one electron from its p orbital to tellurium, leaving it one short with respect to Pb. This relativistic effect is much weaker in indium though, and indium is able to donate all three of its valence electrons (one more than Pb) explaining the observed n-type conduction. This explanation very well might oversimplify things, but nevertheless is still a useful model for thinking about group III doping in PbTe.

To summarize, for a working thermoelectric device both n-type and p-type nanowires need to be synthesized. While PbTe can self-dope through Pb or Te vacancies, controlling these tiny deviations in stoichiometry through electrochemistry would prove next to impossible. Common dopants (Na and I) used in most PbTe thermoelectrics are also impractical due to electrochemical and solubility concerns. Indium and thallium doping is the most likely way to electrochemically synthesize controllably doped PbTe nanowires. The results of attempts to produce indium and thallium doped PbTe are discussed in the following sections.

4.3 Indium Doped PbTe Nanowires

To incorporate indium into the nanowire arrays, indium chloride was added to the plating solution in varying amounts and PbTe was deposited using the same deposition parameters in [3.4]. The amount of indium incorporation in the nanowires was determined through electron microprobe analysis and plotted vs. indium concentration as shown in Figure 3. In the range of concentrations studied, there is a linear relation between the two variables.

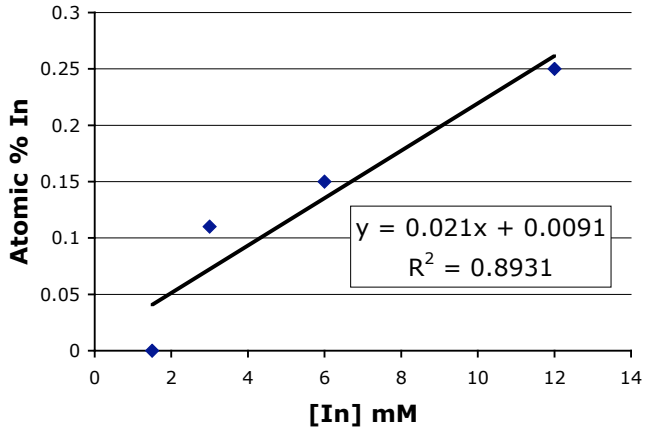

Figure 4-3. Atomic % In dependence on solution concentration

While Figure 3 proves that there is indium present in the nanowire, it is impossible to make any conclusions on the incorporation of indium into the PbTe lattice. A mixture of PbTe and metallic indium equally explains the results in Figure 3. However, this explanation can be ruled out through a XRD study on the lattice parameter of the different nanowires. If indium is truly substituting for lead, the lattice parameter of PbTe should change due to the different sizes of Pb and In. Shown in Figure 4 is the PbTe (111) reflection with differing amounts of indium determined by electron microprobe. A shift in the peak is in fact seen with increasing indium. It should also be noted that no indium or indium telluride peaks were observed in any of the XRDs.

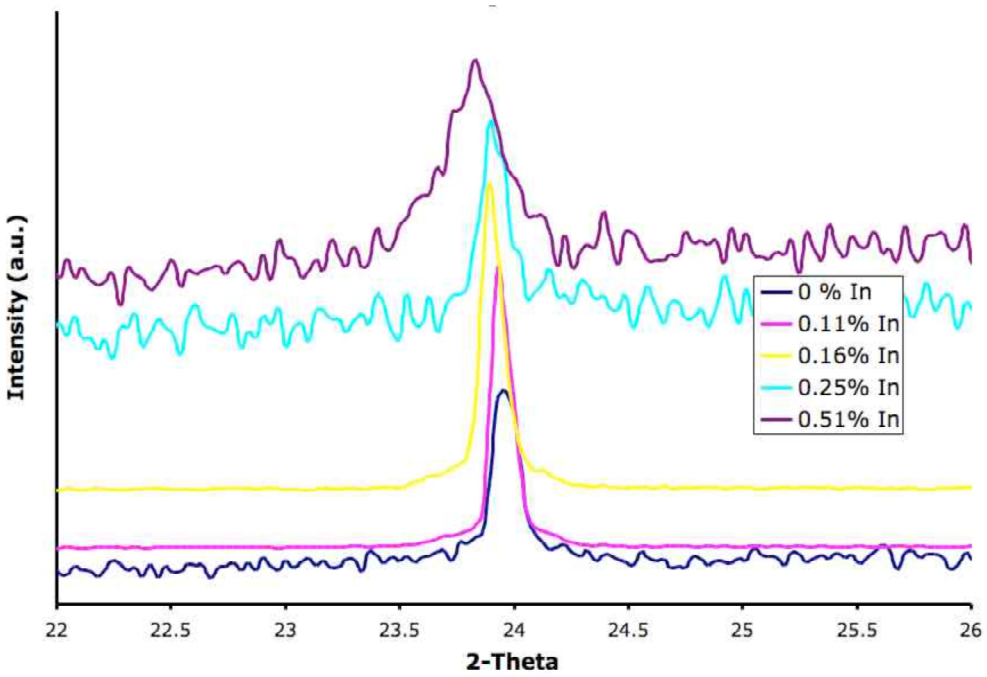

Figure 4-4. PbTe (111) peak with differing % In

Calculating the lattice parameters from the PbTe (111) peak and plotting this lattice parameter versus indium incorporation reveals a linear relation between the lattice constant and atomic percent indium. This relation can be seen in Figure 5. This observation proves that indium must be incorporating into the PbTe lattice instead of merely being deposited as a separate phase.

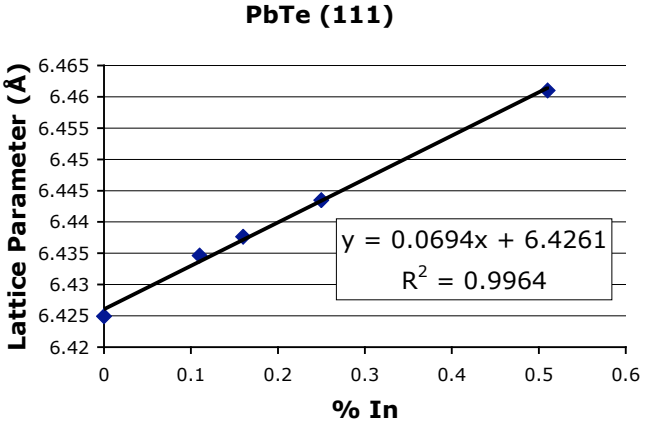

Figure 4-5. Lattice parameter dependence on % In

The lattice parameter trend shown in Figure 5 increases linearly with increasing indium. Based on everything that is known about PbTe and indium doping this result was surprising. If In^{3+} were substituting for Pb^{2+} the lattice parameter would be expected to decrease based on the ionic radii of Pb^{2+} (133 pm) and In^{3+} (92 pm). Another idea in the literature is that indium could be substituting as both In^{+} and In^{3+} through the disproportionation of In^{2+}.[106] This model would also imply a decreasing lattice parameter though since the average of ionic radius of In^{+} (130 pm) and In^{3+} is still smaller than

Pb^{2+}. XPS studies on indium doped PbTe suggest that In is actually In^{+} however.[107] Again based on the relative sizes of In^{+} and Pb^{2+} a small decrease in the lattice parameter would be expected. Looking to the literature there have been three studies on how indium doping affects the lattice parameter of PbTe. The results from the three studies are shown in Figure 6. Two of the three report a decrease in lattice parameter with increasing indium doping but differ on the slope and solubility limit. The third and most recent study observed both a decrease and increase in the lattice parameter with indium doping. From 0 to 0.6% In the lattice parameter decreased, but from 0.6 to 1.2% In an increase was observed. Beyond 1.4% In the lattice parameter remains constant and InTe and In_2Te_3 begin to appear in the XRD. This trend in lattice parameter is explained through two different incorporation mechanisms. At low In concentrations indium substitutes for Pb leading to a decrease in the lattice parameter. At higher doping levels In either fills Pb vacancies or squeezes into tetrahedral interstices. While the results in the doped PbTe nanowires show no decrease in the lattice parameter, the slope of the curve agrees reasonably well with the positive slope in the 0.6 to 1.2% In regime in the study. This fact seems to suggest that the indium incorporation mechanism in PbTe nanowires is similar to that observed in the bulk in the 0.6 to 1.2% doping regime (indium incorporation into Pb vacancies or tetrahedral interstices), despite the indium levels in the nanowires ranging from 0.0 to 0.6%.

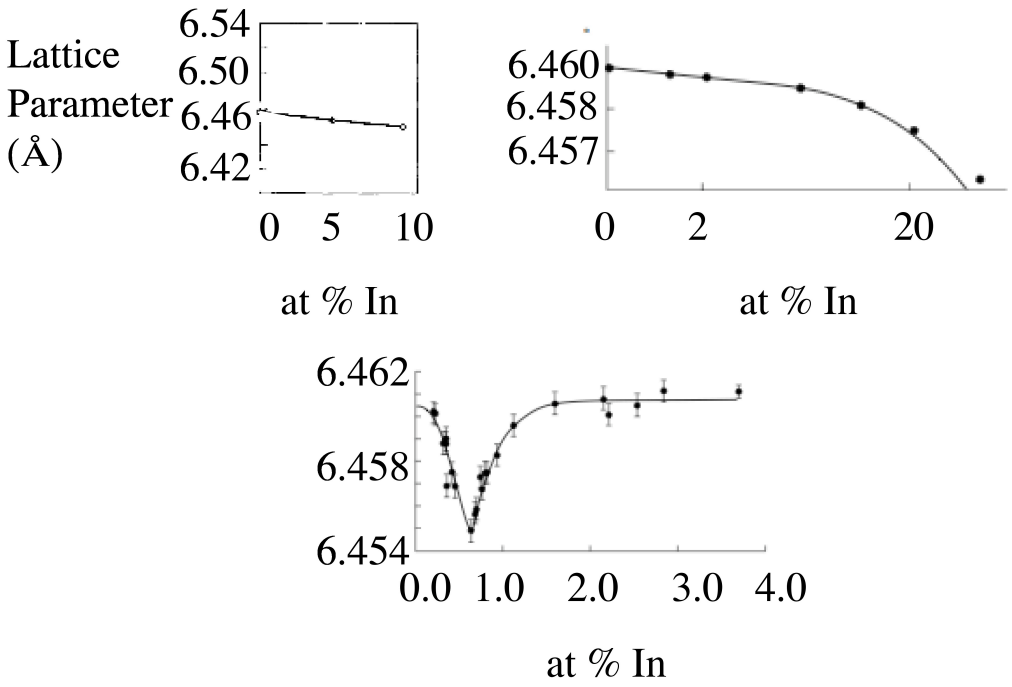

Figure 4-6. Literature lattice parameters of indium doped PbTe[108,109,110]

Of the two possible choices for indium incorporation into PbTe nanowires, indium filling tetrahedral interstices fits best with the observed data and the structure of In_2Te_3. The location of indium in the PbTe lattice should be consistent with two observations of the XRD analysis, specifically a fairly high rate of change in lattice parameter and a broadening of the XRD peak with increasing indium. A tetrahedral interstice is much smaller than an octahedral Pb vacancy. Therefore, introducing an

indium atom to a tetrahedral interstice will have a much larger impact on the lattice parameter than a Pb vacancy. It also follows that since indium fits poorly into this location it would lead to a disruption in the crystallinity of the lattice, thus explaining the broadening of the XRD peak. The fact that the concentration of stable Pb vacancies in PbTe is far less than the amount of indium added also suggests a tetrahedral incorporation mechanism. Additionally, the structure of In_2Te_3 is a defect zinc blende structure.[111] The tellurium sublattice is still face-centered cubic (FCC) like PbTe, but now indium occupies a fraction of the tetrahedral holes. It follows that during the course of the deposition indium might preferentially try to settle in tetrahedral sites in the growing PbTe structure, similar to In_2Te_3.

Annealing the indium doped PbTe nanowires at 300 °C under house N_2 for 90 hrs yields a change in the lattice parameter compared to the as-deposited wires. The new lattice parameters are plotted with the initial results in Figure 7. The annealed results no longer show a linear increase in lattice parameter with increasing indium concentration. Instead the lattice parameter decreases slightly and then remains constant. This result can be interpreted within the framework of the hypothesis that indium is being incorporated into tetrahedral interstices. Since indium is too large for the tetrahedral interstices in PbTe, it may relax upon annealing to a lower energy location, thereby decreasing the lattice parameter. However, the concentration of available locations for indium to move appears to be limited to below 0.1% In. Beyond this doping level there is no further change in the lattice parameter and excess indium is most likely extruded from the structure.

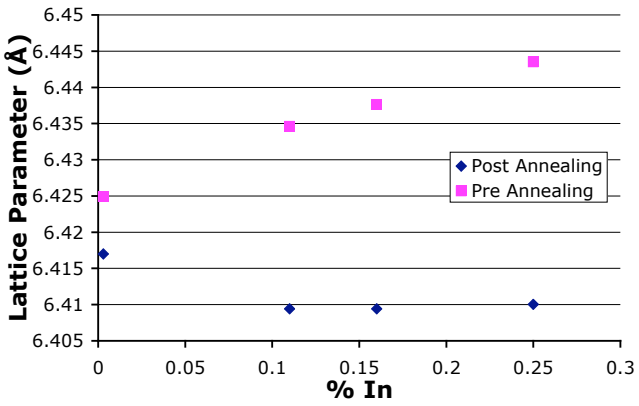

Figure 4-7. Annealed lattice parameters of indium doped PbTe

4.4 Thallium Doped PbTe Nanowires

Thallium nitrate was added to the PbTe plating solution and the amount of thallium incorporated into the wires was determined by electron microprobe, as shown in Figure 8. In contrast to the case of indium doping, the amount of thallium incorporated into the wires does not appear to scale linearly with $TlNO_3$ in solution. Instead, there is only a general trend of increasing thallium detected with increasing thallium in solution.

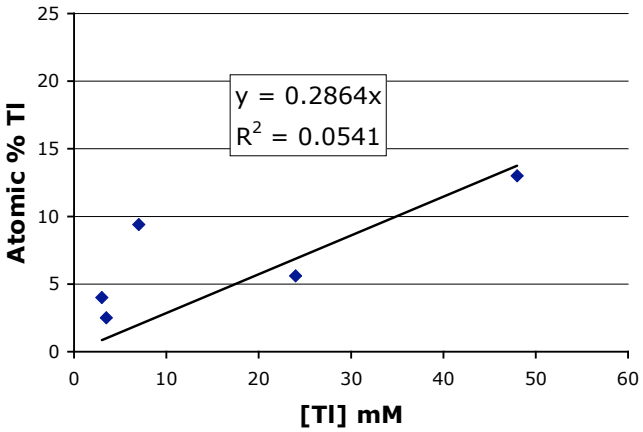

Figure 4-8. Atomic % Tl dependence on solution concentration

To establish whether thallium was being incorporated into the PbTe structure the lattice parameters were determined. Figure 9 shows the lattice parameter of PbTe versus the percent of thallium detected by microprobe. While there are observed changes in the lattice parameters, they do not fit a linear regression. Substituting Tl^{+} for Pb^{2+} should result in an increase in the lattice parameter based on the ionic radii of Tl^{+} (164 pm) and Pb^{2+} (133 pm). In the case of thallium, unlike indium, the 3+ oxidation state is too high in energy to be a likely dopant in PbTe, thus negating the possibility of a decreasing lattice parameter (Tl^{3+} = 103 pm). The large difference in radii of thallium and indium also makes it unlikely that thallium could fit into tetrahedral interstices. Reports in the literature support the idea that the lattice parameters of thallium doped PbTe do increase due to thallium substitution.[108] An increase in the lattice parameter is in fact generally observed suggesting there is some substitution, but the fact that it does not follow a linear trend hints at a more complex explanation than simple substitution.

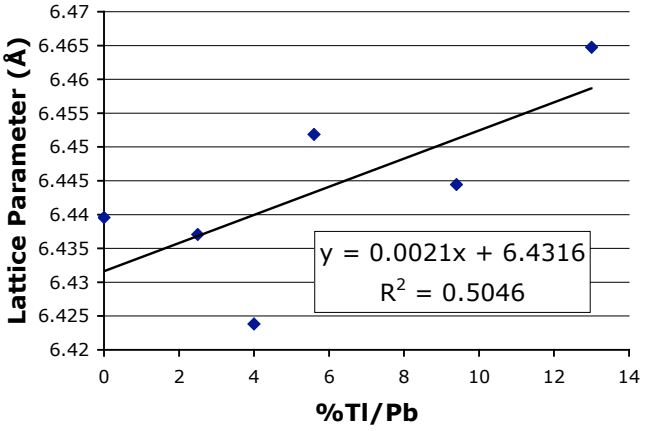

Figure 4-9. Lattice parameter dependence on % Tl

Annealing the as deposited nanowires at 340° C for 90 hrs under house nitrogen however linearizes the lattice parameters of the Tl doped PbTe arrays. The calculated

lattice parameters of the as deposited and annealed arrays vs the thallium incorporated are shown in Figure 10.

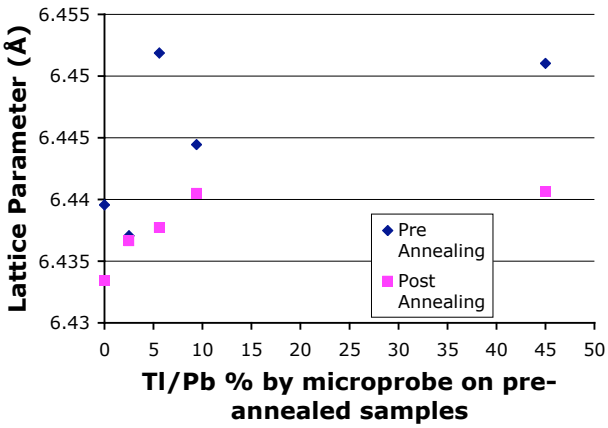

Figure 4-10. Annealed lattice parameters of thallium doped PbTe

An explanation for these results lies in the rather complicated electrochemistry of thallium and tellurium, which will be explained in chapter 5. In contrast to the case of indium, thallium telluride compounds are readily deposited from a solution of thallium and tellurium. At the potential that PbTe is deposited, TlTe should also be deposited as a side product. Upon heating, the side product TlTe melts incongruently to yield liquid and Tl_5Te_3.[112] The newly formed Tl_5Te_3 diffuses into the PbTe nanowires forming a solid solution up to the solubility limit of about 8 atomic % Tl (1.6 mol %Tl_5Te_3).[113] This mechanism is consistent with the larger unit cell size of Tl_5Te_3 and the observed increase in the PbTe lattice parameter upon annealing. Additionally, the lattice parameter increases up to roughly 10 atomic % pre-annealed Tl, close to the solubility limit of Tl_5Te_3 in PbTe. Had TlTe alloyed with PbTe instead, the lattice parameters would level out at its solubility limit of ~2 atomic % Tl.[114] Electron microprobe on selected samples after annealing also reveals a decrease in the Te/Pb ratio and the Tl/Pb ratio indicating some Tl and Te are lost, presumably due to their vapor pressures over the liquid phase present during annealing.

4.5 Conclusions

Both n-type and p-type arrays of PbTe were grown through the electrochemical incorporation of the appropriate dopant atom. Indium initially incorporates into the PbTe lattice in a high energy interstitial location and then relaxes to a lower energy position upon annealing. Thallium, on the other hand, initially deposits as a mixture of thallium doped PbTe and the side product TlTe. Upon annealing TlTe melts incongruently yielding Tl_5Te_3, which then forms a solid solution with PbTe.

Chapter 5: Electrochemistry of Thallium and Tellurium in Aqueous Solutions

As mentioned in chapter 4 the electrochemical synthesis of Tl doped PbTe produced some interesting results. Truly understanding the doping mechanism required knowledge of the electrochemistry of thallium and tellurium in aqueous solutions that was completely lacking in the literature. A thorough investigation into the electrochemistry provided not only an explanation for the results of Tl doped PbTe but also produced the first electrochemical synthesis of two interesting thallium telluride compounds.

In this chapter the first reported electrodeposition of TlTe and Tl_5Te_3 will be presented. The deposition mechanism of these two different thallium tellurides was studied through a series of cyclic voltammograms and deposited thin films. In the case of TlTe, tellurium is first deposited and then thallium is underpotentially deposited to form the compound. Tl_5Te_3, which is deposited at more negative potentials, is formed by first electrochemically generating H_2Te, which subsequently reacts with thallium in solution. Nanowires of TlTe can be grown inside 40 nm porous alumina templates. XRD reveals the wires grow in the 001 direction and electron microprobe analysis shows them to be tellurium rich.

5.1 Thallium Telluride Thermoelectrics

One set of compounds that so far has been ignored by the electrochemical community is thallium tellurides. Thallium and tellurium form a number of compounds[112] with varying properties, ranging from metallic for TlTe[115], semimetallic for Tl_5Te_3[116], and semiconducting for Tl_2Te_3.[117] Thallium containing compounds have been investigated recently as possible thermoelectric materials.[118] Because the electronegativity of thallium is in the middle of the range of values, thallium tends to form strongly covalent compounds with smaller band gaps and higher electron and hole mobilities; these are important characteristics of a good thermoelectric. In addition, the large atomic mass creates a reduction in the lattice thermal conductivity of the material. A wide range of structures can also be anticipated because of the possibility that the 6s lone pair on Tl^+ is stereochemically active, thus generating a rich diversity of chemistry. Several high zT Tl compounds have already been discovered, namely Tl_9BiTe_6 with a maximum zT of 1.2 at 500 K[119], Ag_9TlTe_5 with a zT of 1.23 at 700 K[120], and Tl_2SnTe_5 with a zT of 0.6 at 300 K.[121]

Reported here is the first investigation of the electrochemistry of thallium and tellurium. The deposition mechanism was investigated through a series of cyclic voltammogram studies (CV's). Thin films of TlTe and Tl_5Te_3 were grown and characterized by powder x-ray diffraction (XRD) and scanning electron microscopy (SEM). In addition, nanowire arrays of TlTe were grown in 40 nm porous alumina templates and characterized by XRD, SEM, and electron probe microanalysis.

5.2 CV Studies on Tl-Te Solutions and Peak Identifications

The electrochemical study of the thallium telluride system consisted of various CVs at differing thallium and tellurium concentrations and pH values. CVs were first taken to determine the potential where reduction events occurred. Thin films grown at these reduction potentials were analyzed by XRD and SEM to determine the phase present as well as its morphology. It was found that TlTe deposits before Tl_5Te_3 and the deposition mechanisms of the two thallium tellurides are different. Through changing variables such as concentration and pH, the deposition mechanism was elucidated and this understanding aided in determining the optimal deposition conditions for TlTe and Tl_5Te_3. Once the conditions for successful thin film growth were determined, this knowledge was used in the growth of nanowire arrays in porous alumina templates. These nanowire arrays were characterized by XRD, SEM, and electron microprobe to determine the phase, dimensions, and stoichiometry of the deposited nanowires, respectively.

The CV obtained for a solution of 96 mM $TlNO_3$ with 0.25 M H_3Cit and 0.25 M K_3Cit adjusted to a pH of 1 with concentrated HNO_3 is shown in Figure 1. One reduction wave can be seen beginning around –660 mV. XRD reveals the deposit at this potential to be pure thallium. Therefore this peak can be assigned as follows:

$$Tl^+ + e^- \Rightarrow Tl \qquad (5.1)$$

Also visible is one stripping peak, which can be assigned to the anodic stripping of thallium from the platinum surface.

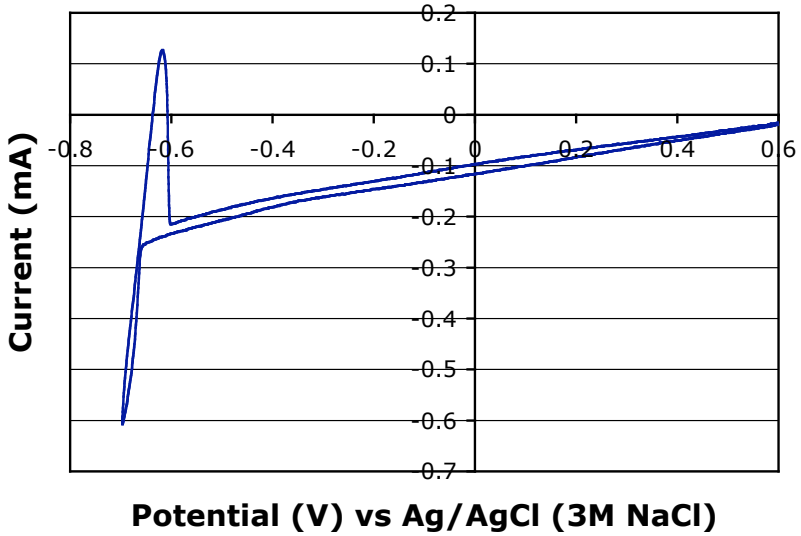

Figure 5-1. Cyclic Voltammogram of Tl^+, reference electrode Ag/AgCl (3M NaCl), scan rate 10 mV/s, pH ~1

The electrochemical behavior of tellurium has already been explained in [3.3] and by previous work.[89,90,91] The CV obtained for 5 mM TeO_2 with 0.25 M H_3Cit and 0.25 M K_3Cit adjusted to a pH of 1 with concentrated HNO_3 is shown in Figure 2. To reiterate,

the first reduction wave (E_{pc} ~ –170 mV) corresponds to the deposition of pure tellurium and can be assigned as follows:

$$HTeO_2^+ + 3H^+ + 4e^- \Rightarrow Te + 2H_2O \quad (5.2)$$

At more negative potentials, a second reduction wave (E_{pc} ~ –700 mV) is observed. As mentioned previously this wave corresponds to the reduction of $HTeO_2^+$ to $H_2Te_{(aq)}$. The $H_2Te_{(aq)}$ immediately reacts to form pure tellurium through the following mechanism.[89,90,91]

$$HTeO_2^+ + 5H^+ + 6e^- \Rightarrow H_2Te + 2H_2O \quad (5.3)$$
$$H_2Te + HTeO_2^+ \Rightarrow 3Te + 2H_2O + H^+ \quad (5.4)$$

One anodic peak can be observed (E_{pc} ~ 540 mV) which is the stripping of deposited tellurium. This observation is consistent with the conclusion that both reduction peaks result in the production of tellurium.

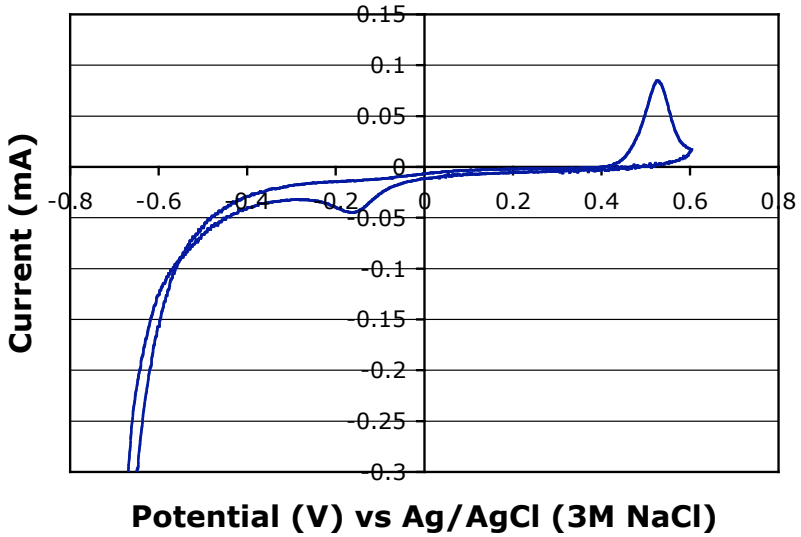

Figure 5-2. Cyclic Voltammogram of $HTeO_2^+$, reference electrode Ag/AgCl (3M NaCl), scan rate 10 mV/s, pH ~1

The CV of a solution of 92 mM $TlNO_3$ and 5mM TeO_2 with 0.25 M H_3Cit and 0.25 M K_3Cit again adjusted to pH~1 with concentrated HNO_3 is shown in Figure 3. In addition to the deposition of pure tellurium (at –170 mV) and pure thallium (at –660 mV), two new reduction peaks appear with E_{pc} near –250 mV and –390 mV. In the reverse scan, in addition to the stripping of thallium and tellurium, there are three new oxidation peaks with E_{pc} near –160 mV, -50 mV, and 50 mV. The peaks have all been identified in this figure. A detailed analysis of the determination will be included in later sections.

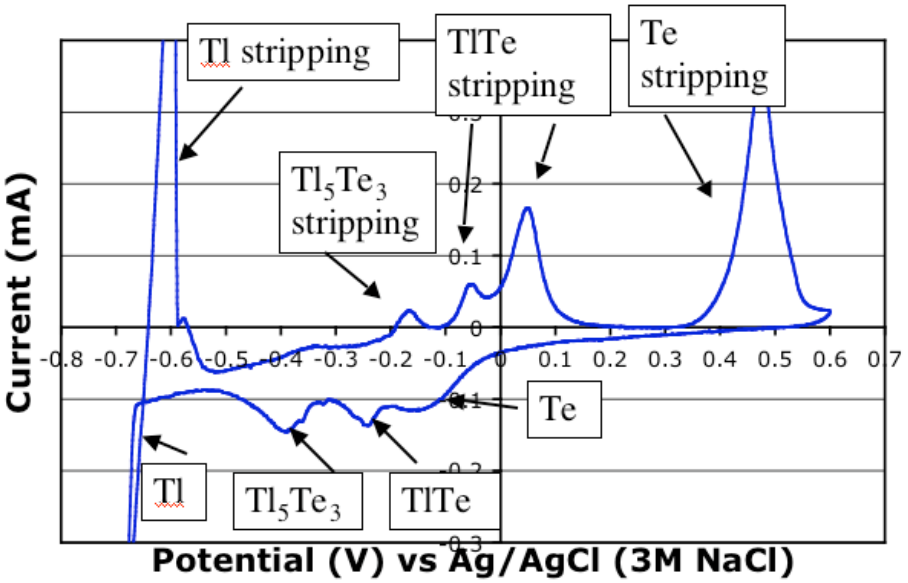

Figure 5-3. Cyclic Voltammogram of Tl^+ and $HTeO_2^+$, reference electrode Ag/AgCl (3M NaCl), scan rate 10 mV/s, pH ~1

Thin films were grown at potentials corresponding to the new reduction peaks to identify the material deposited. The deposit on the working electrode at potentials near –250 mV appears black. The XRD pattern of the film shown in Figure 4 reveals that the deposit is TlTe. The 002 reflection is the strongest peak observed, despite the fact that this reflection is relatively weak in a powder sample. This indicates that the TlTe film is oriented in the [002] direction. No other side products were observed. Deposits prepared around –390 mV again appear black in color. The XRD pattern of the deposit shown in Figure 5 reveals that this deposit is Tl_5Te_3. In contrast to TlTe there appears to be no preferred orientation to the film. The observation of a more negative reduction potential for Tl_5Te_3 is consistent with the decrease in the average charge on the Tl due to an increase in the Tl:Te ratio.

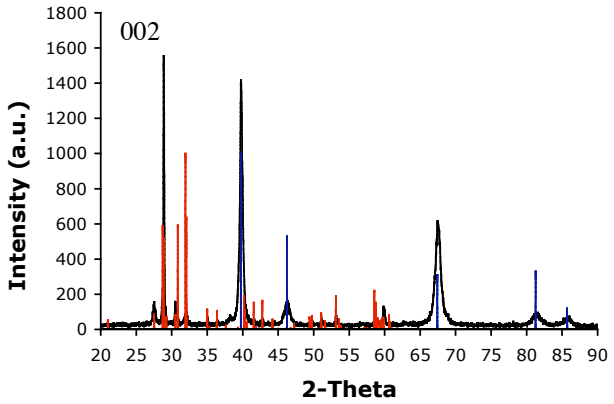

Figure 5-4. X-ray diffraction pattern of TlTe thin film grown at –250mV vs Ag/AgCl (3M NaCl), the 002 reflection has been labeled, TlTe (red) PDF 85-1704, Pt substrate (blue) PDF 04-0802

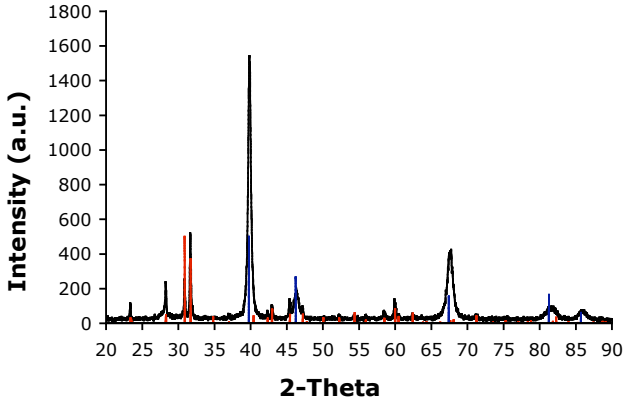

Figure 5-5. X-ray diffraction pattern of Tl_5Te_3 thin film grown at –390mV vs Ag/AgCl (3M NaCl), the 002 reflection has been labeled, Tl_5Te_3 (red) PDF 80-2026, Pt substrate (blue) PDF 04-0802

5.3 Deposition Mechanism of TlTe and Tl_5Te_3

The electrodeposition of TlTe can be described by an under potential deposition mechanism. Tellurium, which is deposited first, causes thallium to be underpotentially deposited (UPD) due to the free energy of formation of TlTe (ΔG_f° = -44.5 KJ/mol)[122]. UPD is a common deposition mechanism, and has been seen in the case of numerous other telluride compounds.[47,89,123,] The energy gained by forming TlTe causes the reduction potential of thallium to be shifted by $\Delta E_{UPD} = \Delta G_f^\circ / zF$ where z is the number of electrons associated with the reduction and F is Faraday's constant.

$$Tl(s) + Te(s) \Rightarrow TlTe(s) \quad \Delta G_f^\circ = -44.5 kJ/mol$$

$$+ \quad \underline{Tl^+ \Rightarrow Tl(s) \quad E_{dep} = -660mV \text{ vs } Ag/AgCl \text{ (3M NaCl)}}$$

$$Tl^+ + Te(s) \Rightarrow TlTe(s) \quad E_{UPD} = E_{dep} + \Delta G_f^\circ \quad \therefore \Delta E_{UPD} = 460 \text{ mV}$$

This equation predicts that thallium will be deposited at a potential ΔE_{UPD} = 460 mV more positive than pure thallium. This calculated underpotential shift corresponds well to the measured shift of 445 mV from the CV of thallium and tellurium solutions. This mechanism places the deposition of TlTe in the class I UPD category as described by Kroger.[124] Class I compounds, like CdTe, CdSe, and CdS, are characterized by $-G_{TlTe}/F < (E^\circ_{Te} - E^\circ_{Tl})$ meaning that the reduction of Tl^+ is determines the deposition potential of TlTe.

One curious aspect of the deposition of TlTe is the fact that Tl_5Te_3 is actually the most thermodynamically stable of the thallium tellurides. The enthalpy of formation of TlTe is 43.9 KJ/mol compared to 216.8 KJ/mol for Tl_5Te_3.[125] Note that enthalpy is used here rather than Gibbs free energy because the entropy of formation was not available. It is probably safe to assume that entropic concerns are negligble. The obvious question then becomes why does Tl not underpotentially deposit onto Te to form Tl_5Te_3, the more stable product? The answer most likely lies in the kinetics of forming the two compounds. The crystal structure of pure Te can be described as helical chains of

tellurium that pack together to form a hexagonal closed packed array of Te atoms. TlTe has a similar chain-like structure of Te atoms. When thallium underpotentially deposits onto the chain-like structure of tellurium, it is therefore kinetically more favorable to form TlTe instead of Tl_5Te_3, which lacks tellurium chains. It is notable that using slow, pulsed depositions to allow sufficient time to form Tl_5Te_3, results in a mixture of the two products being underpotentially deposited in XRD. This provides evidence that TlTe is a kinetic product.

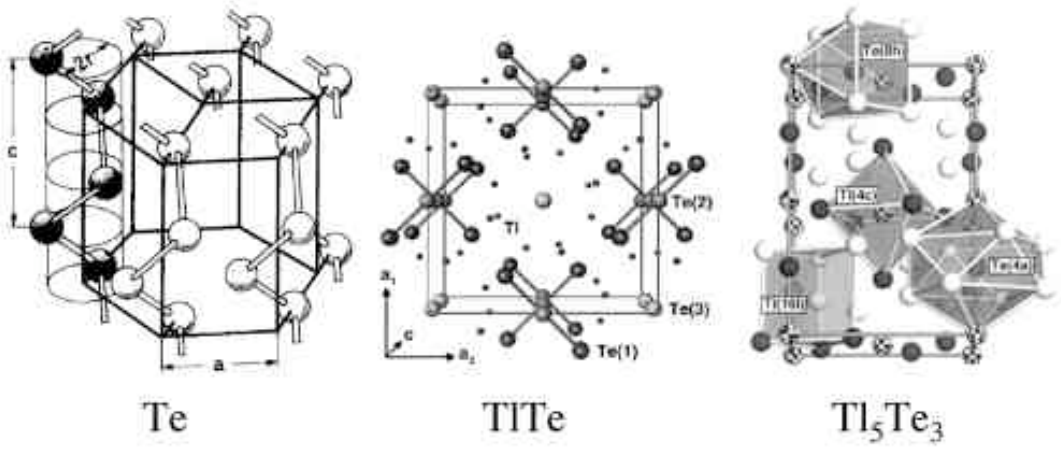

Figure 5-6. Structure of Te[126], TlTe[127], and Tl_5Te_3[125]

Tl_5Te_3 deposits at more negative potentials than TlTe. The deposition mechanism of Tl_5Te_3 is predicted to be different than that of TlTe. $H_2Te_{(aq)}$ is first formed from the reduction of $HTeO_2^+$, which then reacts immediately with Tl^+ to form Tl_5Te_3. Evidence for this mechanism and the TlTe UPD mechanism was gathered through CVs recorded at different thallium ant tellurium concentrations as well as different values of pH. Presented below are the results and insights that support the purported hypotheses.

5.4 CV Study on Thallium Concentration Dependence

The first reduction peak at –170 mV corresponds to the deposition of Te. Subsequently, TlTe is formed at –250 mV. Doubling the concentration of thallium resulted in the CV shown in Figure 7. The deposition peaks of Te, TlTe, and Tl_5Te_3 have been labeled. It is evident from the CV that increasing the thallium concentration had no effect on current density related to the deposition of TlTe. This indicates that the deposition of TlTe is limited by the diffusion of $HTeO_2^+$ to the electrode surface and the subsequent formation of a layer of Te. Similar results have been obtained for the deposition of other tellurides.[47,89,128] Similarly, the reduction of Tl_5Te_3 at –390 mV is limited by the diffusion of $HTeO_2^+$ to the electrode surface despite the fact that the phase is thallium-rich compared with TlTe. Diffusion of $HTeO_2^+$ to the electrode surface limits the formation of both TlTe and Tl_5Te_3.

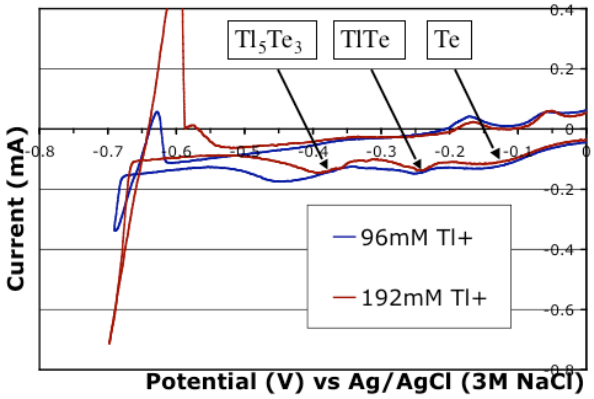

Figure 5-7. Cyclic Voltammogram of 96mM Tl^+ and 5mM $HTeO_2^+$ compared with 192mM Tl^+ and 5mM $HTeO_2^+$, reference electrode Ag/AgCl (3M NaCl), scan rate 10mV/s, pH ~1

While there is no change in current density for the two peaks associated with the deposition of TlTe and Tl_5Te_3 when the Tl^+ concentration is increased, there is a shift in the potential at which the peaks occur. The onset of the peak associated with the deposition of pure thallium is shifted by 10-15 mV to a more positive potential (~ –650 mV), which is close to the value predicted by the Nernst equation.

$$\Delta E_{Tl} = 59.16mV\ (\log_{10}(192mM)-\log_{10}(96mM) = 16.9mV \qquad (5.5)$$

The TlTe reduction wave is shifted by this same amount. This observation is consistent with a class I UPD mechanism for the deposition of TlTe. Since the reduction of Tl^+ in solution determines the formation potential for TlTe, a shift in the reduction potential of pure thallium due to the Nernst equation will cause an equal shift in the reduction of TlTe.

The shift in the reduction potential of the Tl_5Te_3 peak (~50 mV) by increasing the thallium concentration is larger than in the case of TlTe reduction. This makes it unlikely that Tl_5Te_3 is being deposited with the same UPD mechanism as invoked for TlTe. Had Tl_5Te_3 been deposited through an UPD mechanism, the shift in its reduction potential should have corresponded to the shift seen in the pure thallium reduction peak, i.e. ~10 mV.

5.5 CV Study on Tellurium Concentration Dependence

Increasing the tellurium concentration resulted in the CV shown in Figure 8. Consistent with the earlier observation that diffusion of $HTeO_2^+$ is the limiting step in both the deposition of TlTe and Tl_5Te_3, an increase in current density for these two reductions is observed. It is worth noting that there is no significant change in current or potential for the deposition of tellurium. This is consistent with reports that $HTeO_2^+$ adsorbs strongly to the platinum surface, which is then reduced to pure tellurium.[87,129]

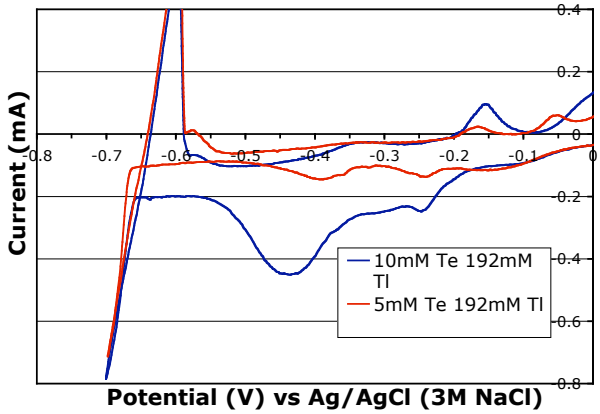

Figure 5-8. Cyclic Voltammogram of 192mM Tl^+ and 5mM $HTeO_2^+$ compared with 192mM Tl^+ and 10mM $HTeO_2^+$, reference electrode Ag/AgCl (3M NaCl), scan rate 10mV/s, pH ~1

5.6 CV Study on pH Dependence

Adjusting the pH from 1 to 4 produces the CV shown in Figure 9. In the less acidic solution there are only two reduction peaks (-230 mV and –680 mV). The peak at –680 mV corresponds to the reduction of Tl^+ to pure thallium and is unchanged from the more acidic solution. The peak at –230 mV corresponds to the formation of TlTe as determined by XRD of films grown at this potential. Deposition of Te and Tl_5Te_3 are not observed.

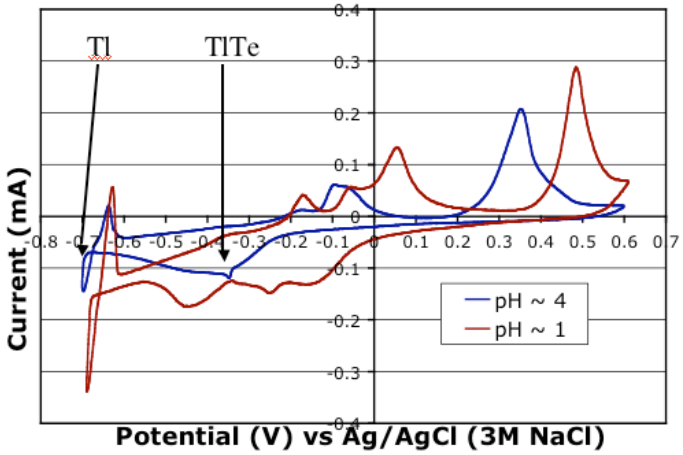

Figure 5-9. Cyclic Voltammogram of 96mM Tl^+ and 5mM $HTeO_2^+$ at pH ~1 and pH~4, reference electrode Ag/AgCl (3M NaCl), scan rate 10mV/s

Since TlTe is formed through the underpotential deposition of Tl onto Te, its reduction potential is intimately associated with the reduction potential of pure Tl. Adjusting the pH of the solution to a more neutral value has no effect on the reduction potential of pure Tl since no H^+ is required for its deposition. Therefore, TlTe should form at a potential that is 460 mV more positive than Tl, regardless of the acidity. However, the underpotential deposition of Tl is caused by free energy gained from forming TlTe and therefore first requires the deposition of Te onto the electrode surface.

The reduction of tellurium, however, does depend on pH. The reduction potential of tellurium shifts to more negative potentials with increasing pH because H^+ is a reactant in the reduction.

$$HTeO_2^+ + 3H^+ + 4e^- \Rightarrow Te + 2H_2O \quad (5.6)$$

The observation of only one reduction wave in pH = 4 solution can be explained by the reduction potential of tellurium being shifted to a more negative potential than where TlTe should be deposited by the prediction of the UPD mechanism. Once Te is deposited, Tl is immediately underpotentially deposited, thus resulting in a coalescence of the reduction peaks of Te and TlTe. It is likely that the TlTe formed at pH = 4 is more pure than the deposit obtained at pH = 1 because in more acidic solutions, Te deposits at more positive potentials compared with TlTe. However, this hypothesis has not been tested.

The peak corresponding to Tl_5Te_3 is also absent in the CV of the pH~4 solution. The deposition mechanism must therefore have a strong pH dependence. In the acidic case the Tl_5Te_3 peak is observed around –390 mV. It is predicated that $H_2Te_{(aq)}$ is first formed at this potential and then it reacts immediately with Tl^+ to form Tl_5Te_3. A similar reaction of a telluride ion with Tl^+ to produce Tl_5Te_3 has been reported where TlCl added to liquid ammonia solution of Na_2Te resulted in a metathesis reaction yielding Tl_5Te_3 and NaCl.[130] $H_2Te_{(aq)}$ is formed at a more positive potential then when just $HTeO_2^+$ is present in solution, due to the formation of Tl_5Te_3. This mechanism is similar to the one proposed for the electrodeposition of Bi_2Te_3 near this potential.[89] Adjusting the pH to 4, shifts the production of $H_2Te_{(aq)}$ outside of the electrochemical window thus preventing the formation of Tl_5Te_3.

The oxidation peaks of TlTe and Tl_5Te_3 can be assigned by comparing the pH ~1 and pH~4 CVs. The two CVs for pH ~1 and pH ~4 are both shown in Figure 10, with the CV for pH~1 shifted by –150 mV to line up the oxidation peaks. The two oxidation peaks beginning at –200 mV and ending at 0 mV have similar shape indicating that they are due to a similar oxidation process. In addition, because only TlTe can be deposited from the more neutral solutions these two peaks can be assigned to the stripping of TlTe. The two oxidation peaks of TlTe can most likely can be assigned to first the oxidation of Tl followed by the oxidation of the remaining Te. The remaining unassigned oxidation event occurring at pH~1 with an E_{pc} near –160 mV has to be that of Tl_5Te_3.

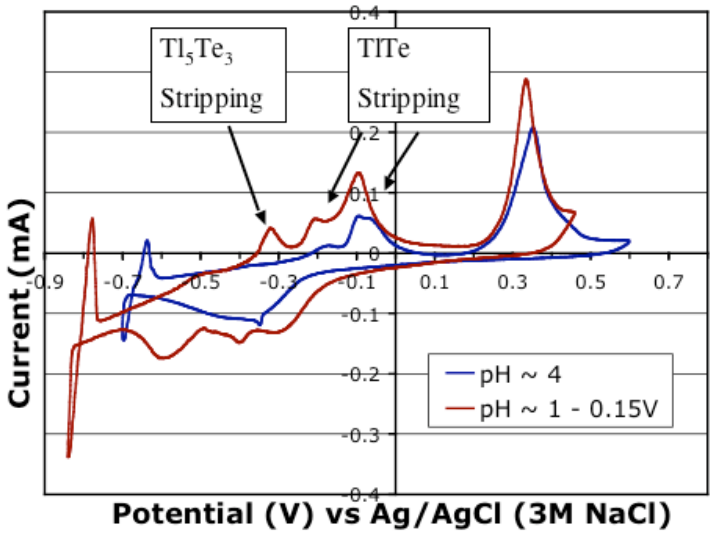

Figure 5-10. Cyclic Voltammogram of 96mM Tl^{+} and 5mM $HTeO_2^{+}$ at pH ~4 and pH~1, the pH~4 CV has been shifted by –150mV to show the overlap in oxidation peaks, reference electrode Ag/AgCl (3M NaCl), scan rate 10mV/s

5.7 Thin Film Morphology

The SEM images of the TlTe and Tl_5Te_3 films are shown in Figure 11 and 12, respectively. The TlTe films appear smooth with relatively small feature sizes in the range of 0.1 to 1.5 μm. This is consistent with what is seen in other materials that are deposited through an UPD mechanism.[89] The Tl_5Te_3 film on the other hand appears much coarser. The feature sizes in this case have a wide range from a few microns all the way up to almost 15microns. The varied and coarse grain structure is consistent with the claim of a two-step deposition mechanism for Tl_5Te_3. The non-oriented XRD of Tl_5Te_3 films reinforces this idea of $H_2Te_{(aq)}$ reacting in solution near the electrode surface to form the compound.

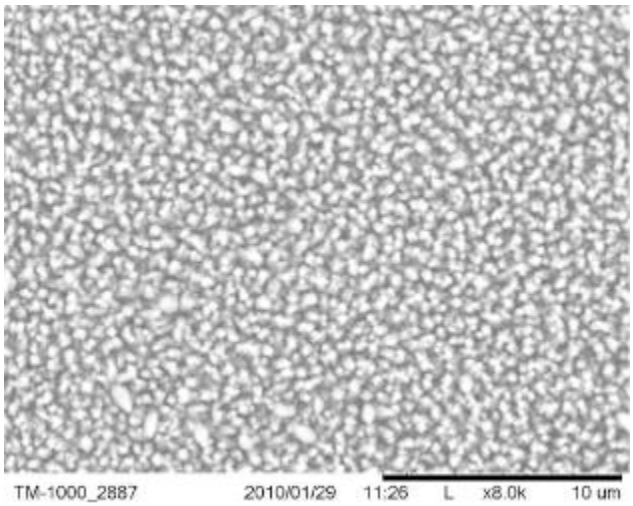

Figure 5-11. Planar SEM image of thin film of TlTe grown at –250mV vs Ag/AgCl (3M NaCl)

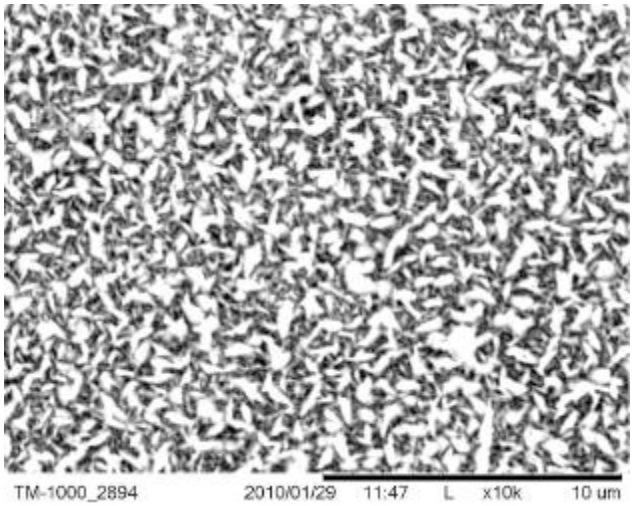

Figure 5-12. Planar SEM image of thin film of Tl_5Te_3 grown at –390mV vs Ag/AgCl (3M NaCl)

5.8 Nanowire Growth

Using the information gathered from CVs and thin films, nanowire arrays of TlTe were grown in 40 nm porous alumina templates. The XRD pattern for the TlTe array is shown in Figure 13. The TlTe XRD pattern shows only two peaks belonging to the 002 and 004 reflections of TlTe, indicating growth in the (002) direction. This is consistent with the orientation found in thin films and also with the chain-like structure of the compound.[131,132,133] In Figure 14, SEM images of the TlTe nanowires are shown. The wires are 40 nm in diameter as set by the porous alumina template and 30 μm in length.

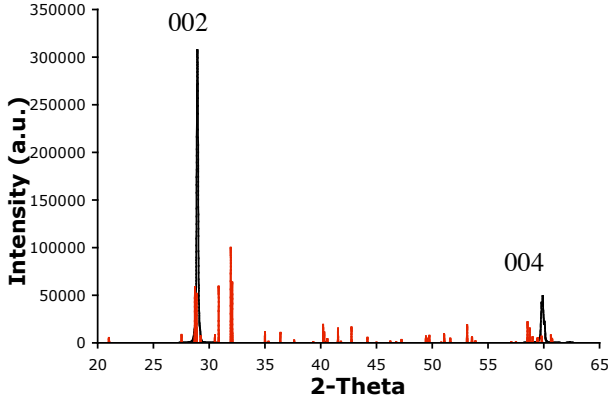

Figure 5-13. X-ray diffraction pattern of TlTe nanowire array, the 002 and 004 reflection have been labeled, TlTe (red) PDF 85-1704

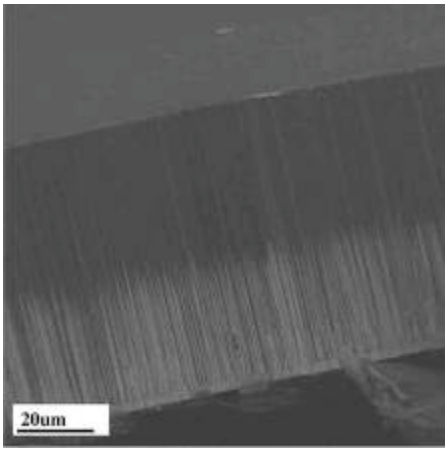

Figure 5-14. Cross-section back-scattered SEM image of TlTe nanowire array

The composition of the wires was determined by polishing the platinum backing electrode off and using electron microprobe analysis. The wires were found to be Te rich with a Te/Tl ratio of 1.77+/-0.32. Due to the UPD mechanism excess tellurium is a common problem and has been observed in a number of tellurides deposited by electrodeposition.[45,81,134] The Te/Tl ratio in TlTe is considerably higher than in electrodeposited PbTe, which follows from the fact the deposition potentials of thallium and tellurium are even further apart than lead and tellurium.

Attempts at growing nanowire arrays of Tl_5Te_3 proved more difficult than TlTe. Nanowires grown near the potentials used in the growth of thin films of Tl_5Te_3 appear at first to succeed in creating Tl_5Te_3 nanowires. Shown in Figure 15 is the XRD for a Tl_5Te_3 array grown in a PAA template. The pattern matches well with what is predicated for Tl_5Te_3. However, overgrowth can be seen in the SEM images of the nanowire array, shown in Figure 16. The peaks observed in the XRD in Figure 15 are therefore most likely from the overgrowth and not the nanowires. To determine the composition of the nanowires, the overgrowth must first be removed by polishing. With the overgrowth removed, the XRD of the array reveals the nanowires are a mixture of Tl_5Te_3 and TlTe.

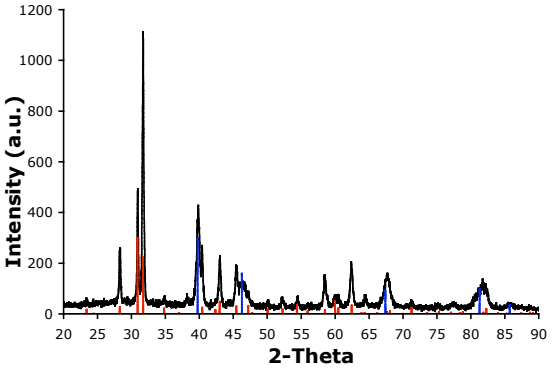

Figure 5-15. X-ray diffraction pattern of Tl_5Te_3 nanowire array, Tl_5Te_3 (red) PDF 80-2026, Pt (blue) PDF 04-0802

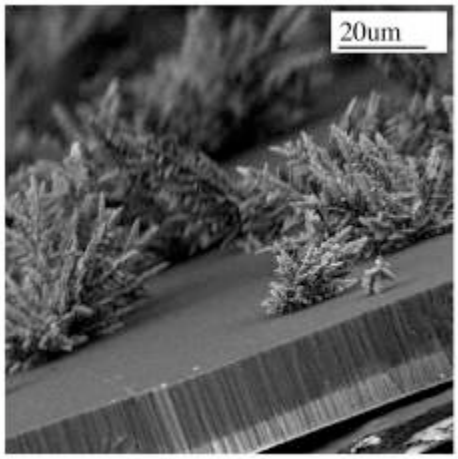

Figure 5-16. Cross-section back-scattered SEM image of Tl_5Te_3 nanowire array showing overgrowth

5.9 Conclusions

The electrodeposition of two different thallium tellurides was demonstrated both as thin films and nanowire arrays. TlTe deposits through an UPD mechanism with Tl being underpotentially deposited on tellurium. Tl_5Te_3 deposits through a two-step mechanism whereby $H_2Te_{(aq)}$ is first formed and then reacts with Tl^+ in solution. In acidic solutions (pH~1) it is possible to deposit thin films of both TlTe and Tl_5Te_3 by means of these mechanisms. Adjusting the pH of solution more basic shifts the reduction potentials of TlTe and Tl_5Te_3 more negative, and at pH~ 4 the reduction of Tl_5Te_3 occurs outside of the solvent window, thereby preventing its deposition. Using a pH~4 solution and depositing into 40nm porous alumina template results in oriented pure phase TlTe nanowires without any Tl_5Te_3 present by XRD. Attempts at growing nanowires of Tl_5Te_3 however resulted in a mixture of the two phases. These two compounds have the potential to show interesting thermoelectric properties in the nanowire form and could serve as a starting point for the synthesis of more complex thallium tellurides. In addition, knowledge of the complex electrochemistry has led to a better understanding of the results in chapter 4.

Chapter 6: Thin Film Measurements

Chapters 3 and 4 outlined the electrochemical synthesis of pure and doped PbTe nanowires in PAA. Ultimately, it is the transport properties of these wires that will determine the success of the thermoelectric modules created. However, transport measurements on single nanowires are extremely difficult to make and very time consuming. Measurements on arrays of nanowires, which will be discussed in detail in chapter 7, can be equally challenging. The major difficulty lies in creating electrical contacts to all 10^{10} wires per square centimeter. The uncertainty in the number of wires contacted and contact resistances make extracting nanowire properties from array measurements very difficult. However, measurements on thin films are infinitely easier to make than on nanowires. While these measurements will not give any information on the nanowire properties, they will provide some insight into the properties of electrodeposited PbTe. While there have been numerous reports on the properties of traditional high temperature synthesized PbTe, studies on the properties of electrodeposited PbTe are lacking, despite numerous examples of electrodeposited PbTe in the literature. In addition to filling in a gap in the literature, measurements on electrodeposited thin films of PbTe should point toward the best growth conditions for nanowires.

In this chapter, thin film transport measurements, specifically electrical conductivity and Seebeck coefficient, will be reported and analyzed. Thin films of PbTe were electrodeposited here at UC Berkeley. The electrical conductivity and Seebeck coefficients were measured by a team led by Dr. Marisol Martin-Gonzales at the Institute of Microelectronics in Madrid.

6.1 Experimental Methods

The explanation of the measurement techniques was summarized from an internal report prepared by the Madrid group. The illustrations in this section were taken from that report.

A Van der Pauw method[135] was used to measure the electrical conductivity of thin films of PbTe. In order for this method to be successful the sample must be homogenous and of uniform thickness. The validity of these two statements with regards to the films studied will be further explored in later sections. The experimental set up for the resistance measurement is shown in Figure 1. The resistivity measurements were made by placing four electrical contacts at the four corners of the PbTe thin film. An electrical current is run through the sample from P to O and the voltage is measured across leads M and N. Using Ohm's law the resistance of the thin film can be calculated. This value

however is the resistance of the combination of the PbTe film and the Pt/Ti substrate.

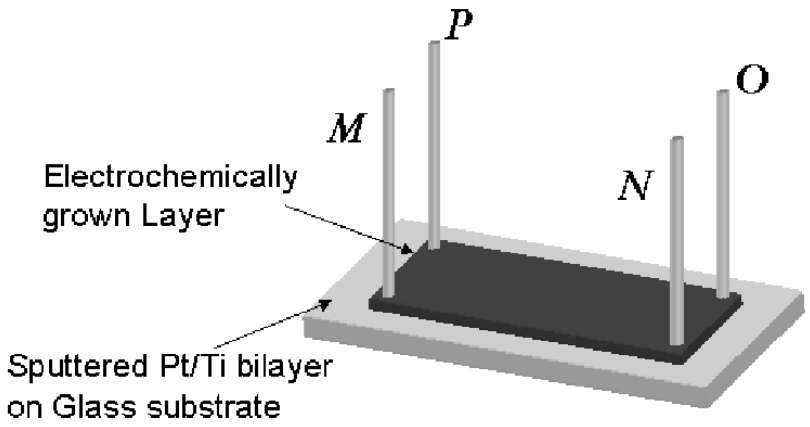

Figure 6-1. Experimental setup for thin film resistance measurements

By treating the sample as resistors in parallel, the resistivity of the PbTe layer can be extracted from this total resistance. The total resistance of the sample is equal to following equation,

$$R_T = \frac{1}{\frac{1}{R_1} + \frac{1}{R_2} + \cdots + \frac{1}{R_n}}$$

where R_1 to R_n are the resistances of the individual resistors in parallel. The resistance of each layer is equal to the resistivity multiplied by length, divided by the width and thickness, d. Each layer has the same length and width, but a different thickness. Substituting the resistivity of each layer into the equation yields the following equation,

$$\frac{\rho_T}{d_T} = \frac{\prod_{i=1}^{n} \rho_i}{\sum_{i=1}^{n} \left(\prod_{i \neq j} \rho_i \cdot d_j \right)}$$

This equation can be simplified if the system is treated as two layers, the PbTe layer and the Pt/Ti layer, as shown in Figure 2.

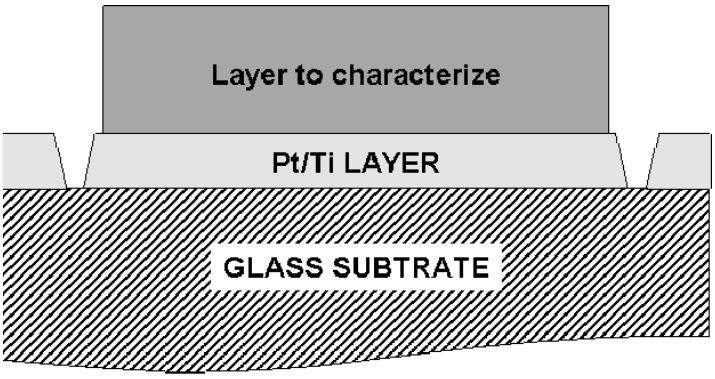

Figure 6-2. Two layer model

The resistivity of the PbTe layer can then simply be calculated from the thickness of each layer, the total resistivity, and the resistivity of the Pt/Ti layer, which was determined by measuring just the substrate. The equation for the resistivity of PbTe is shown below.

$$\frac{\rho_T}{d_T} = \frac{\rho_1 \cdot \rho_2}{\rho_1 \cdot d_2 + \rho_2 \cdot d_1} \quad \Rightarrow \quad \rho_1 = \frac{\rho_T \cdot \rho_2 \cdot d_1}{\rho_2 \cdot d_T - \rho_T \cdot d_2}$$

The Seebeck measurements were conducted in a similar manner to the electrical conductivity measurements. The experimental setup is shown in Figure 3. A temperature gradient is applied to the sample. Thermocouples measure the temperature at the hot and cold side of the film. The potential across the sample is measured with the two leads V_H and V_C. The slope of the potential vs temperature gradient curve is the Seebeck coefficient of the sample.

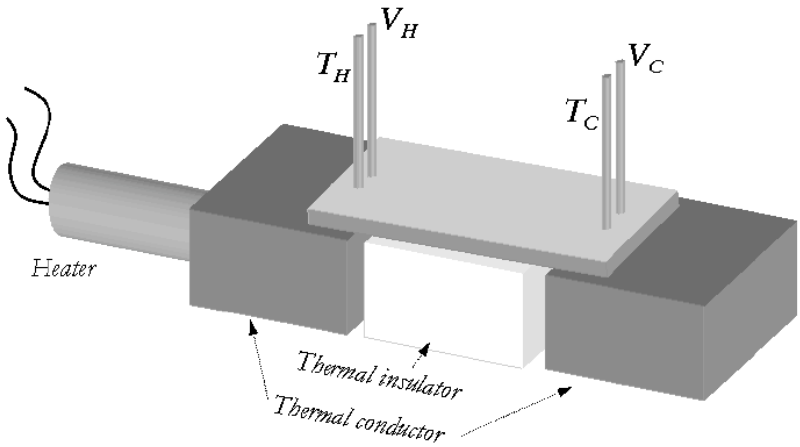

Figure 6-3. Experimental setup for thin film Seebeck measurements

Just like the conductivity measurements, the Seebeck coefficient obtained is for the whole system. However, treating the entire system as two resistors in parallel also

works for extracting the Seebeck coefficient of just the PbTe layer. The PbTe Seebeck coefficient can be calculated from the thicknesses of both layers, the resistivity of both layers, and the Seebeck coefficient of just the Pt/Ti layer. The equation for the PbTe Seebeck coefficient is shown below.

$$S_T = \frac{\sum_{i=1}^{n}\left(\prod_{j\neq i}\rho_j\right)\cdot d_i \cdot S_i}{\sum_{i=1}^{n}\left(\prod_{j\neq i}\rho_j\right)\cdot d_i} \Rightarrow S_T = \frac{\rho_1 \cdot d_2 \cdot S_2 + \rho_2 \cdot d_1 \cdot S_1}{\rho_1 \cdot d_2 + \rho_2 \cdot d_1} \Rightarrow S_1 = \frac{S_T(\rho_1 \cdot d_2 + \rho_2 \cdot d_1) - S_2 \cdot \rho_1 \cdot d_2}{\rho_2 \cdot d_1}$$

6.2 Previous Measurements on PbTe Thin Films

To the best of my knowledge there has only been two reported studies on the transport properties of electrodeposited PbTe thin films. Both reports measured only the resistances and not the Seebeck coefficient. To have a benchmark to compare the results from this thesis, the previous reports will be described below.

The first study deposited PbTe thin films from a basic solution onto a sacrificial Pb substrate, which was then removed for measurements.[136] The sign of the Seebeck coefficient was measured through a hot probe technique. Specifically, a temperature gradient was applied to the sample and the sign of the potential across the sample was measured with a voltmeter. No attempt was made to determine the Seebeck coefficient. Resistivity measurements were made on as-deposited and annealed samples.

All PbTe films initially had a negative Seebeck coefficient. Annealing the samples at 85-120 ºC in air changed the Seebeck coefficient from negative to positive. Dipping the film in a solution of H_2O_2 had the same effect. It was also noted that PbTe just stored in a desiccator for 2 days similarly reversed its Seebeck coefficient. No explicit explanation was given for the change in the Seebeck coefficient, but it is implied that oxidation of the sample is the primary cause. This hypothesis is supported by other studies on the effect of oxygen on PbTe. The resistivity of just-deposited PbTe films was around 1 Ω-cm. Upon annealing at 100 ºC in air for between 168 and 600 hours the resistivity decreased slightly to 0.5 Ω-cm. It is interesting to note that the conductivity of these films are orders of magnitude lower than what is typically measured in bulk PbTe.

The second report deposited PbTe from an acidic solution on a transparent conducting oxide substrate.[137] Only resistivity measurements were taken. The resistivities reported did not account for the substrate, which was not removed prior to measurement. The effect of the deposition temperature on the conductivity of the films was recorded. Resistivities were also measured after annealing samples in an argon atmosphere at 200º and 400º C for 10 minutes.

All of the resistivities measured for this study were on the order of 10^5 Ω-cm. Samples deposited at room temperature had a resistivity of 18 x 10^5 Ω-cm and this decreased to 2.5 x 10^5 Ω-cm when the deposition temperature was raised to 80 ºC. Annealing the films in argon lowered the resistivity even more. Films annealed at 200 ºC showed the lowest resistivity, 1.5 x 10^5 Ω-cm. Unfortunately, since these resistivity values include the substrate, a comparison can not be made to the previous study or even

to bulk PbTe. The decrease in resistivity in both the annealed and 80º C deposition is attributed to an increase in the grain size in the PbTe film. Grain sizes, determined through XRD and the Scherrer equation, increased with increasing deposition temperature and annealing temperature.

From these studies two important factors affecting the properties of electrodeposited PbTe films emerge. The degree of oxidation and the size of the grains clearly have a huge influence on the properties of the film. Even though many of the specifics of the deposition and measurements presented in this thesis are different from these published reports, studying the grain size and oxidation should help in understanding the results of the resistivity and Seebeck measurements.

A clear example of the importance of grain size and oxidation, and also how they are closely related, is found in the properties of PbTe thin films prepared by physical vapor methods. While there has been very little work done on the properties of electrodeposited thin films of PbTe, reports on the properties of films made by high temperature vapor depositions are more numerous. The temperature dependence of the electrical conductivity of these films show an activated response.[138] The hypothesis is that oxygen, which acts as an acceptor in PbTe, is absorbed at the grain boundaries in the film. The acceptor sites at the grain boundaries cause the energy bands to bend and create an activation barrier to electrical conduction, as shown in Figure 4. This band bending at the grain boundaries leads to the observed activated response of the electrical conductivity. Further oxidation will eventually lead to a carrier type inversion as electrons are compensated by holes created by oxygen impurities. This is similar to what was observed in the case of electrodeposited PbTe. Since oxygen is quickly adsorbed at grain boundaries, increasing the amount of grain boundaries should lead to increased oxygen adsorption. Films with more grain boundaries are therefore expected to have a greater oxygen content, which, due to the acceptor nature of oxygen in PbTe, would lead to greater p-type character. These reports are mentioned since grain boundaries and oxidation will have a large effect on the properties electrodeposited films presented in this chapter.

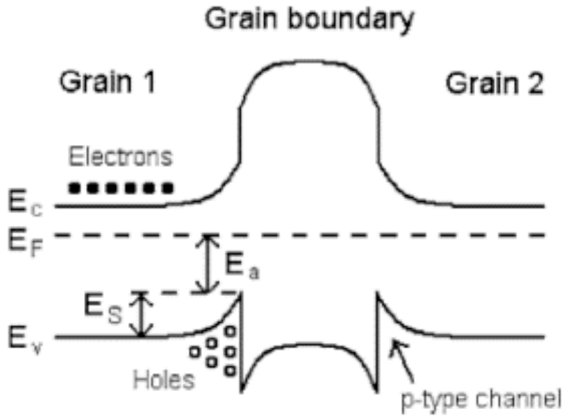

Figure 6-4. Activation barrier at grain boundary in PbTe thin film[139]

6.3 A Potential High zT Film and Sources of Error

Recall that in order for the Van der Pauw method to be applied successfully the films must be uniform and homogenous. Of all the samples prepared only one was considered homogenous enough to extract out the contributions of the PbTe layer in the measurements. The results from that sample will be presented in this section.

Of all the PbTe films grown, PbTe grown at –350 mV was the only film homogenous enough to extract out the contributions of the PbTe layer from the measurements. Shown in Figure 5 is thickness of the homogenous PbTe film across the sample as measured by profilometry. The variation of the thickness over the length of the sample was on the order of 2000 nm. The resistivity of the PbTe layer in the film was 4.0 x 10^{-4} Ω-cm. The Seebeck coefficient of the PbTe layer was –264 ± 20 μV/K. The power factor, $S^2\sigma$, of the sample is then 0.017. Assuming the thermal conductivity of the film is the same as it is in bulk, the calculated zT would be approximately 2 at 300 K. This zT is an order of magnitude higher than bulk PbTe at room temperature and also one of the highest measured zT's.[19] If the resistivity and Seebeck coefficient scale with temperature as they do in bulk PbTe, the highest achievable zT would be even greater.

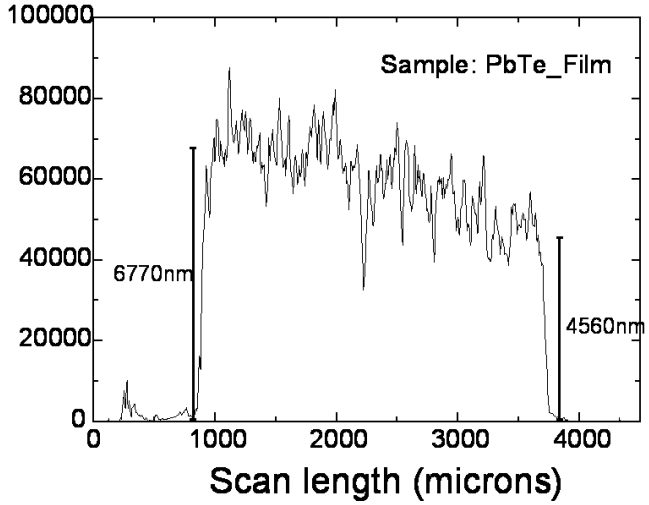

Figure 6-5. Profile of PbTe sample

Assuming the measurement of the figure of merit in this film is truly accurate, it would change the world of thermoelectrics. Not only would this figure of merit outshine any other material, it would necessitate a great change in thinking. The increase in the zT of this film only comes from an increased power factor. In this size regime, quantum confinement effects should be minimal so an increased power factor is not expected. A new explanation would then be needed. It is important to be cautious though because as Carl Sagan liked to say "Extraordinary claims require extraordinary evidence"[140] and this zT is certainly an extraordinary claim. Unfortunately, attempts at providing extraordinary evidence all fell short. Reproducing these results with other PbTe films all were unsuccessful. A discussion of the sources of error in the measurements is warranted to try and determine the cause of the abnormally high zT.

A high measurement in the power factor could be the result of an overestimate in the Seebeck coefficient, an overestimate in the electrical conductivity, or both. A logical

method to determine which measurement, either the resistivity or Seebeck coefficient, contributes most to the error is to compare the film measurements to expected bulk values. This is difficult, however, because the Seebeck coefficient and electrical conductivity can take on a range of values in bulk PbTe depending on the carrier concentration. It is possible to create electrically conductive PbTe by increasing the carrier concentration, and it is also possible to have a high Seebeck coefficient by decreasing the carrier concentration. Using the bulk electron mobility in PbTe, it is in fact possible to calculate the carrier concentration needed to achieve the electrical conductivity in the thin film.[70] Likewise, from the Mott equation it is possible to calculate the carrier concentration needed to achieve the Seebeck coefficient observed in the thin film.[19] Comparing these two carrier concentrations to the allowable carrier concentrations determined by the phase diagram of pure PbTe should indicate which value is off. The calculations are shown below.

$$\text{Seebeck carrier concentration } n = \pi/3\ (3Seh^2/8\pi^2 k_b^2 m_e T)^{-3/2}$$
$$n \cong 3 \times 10^{18}\ cm^{-3}$$

$$\text{Resistivity carrier concentration } n = \sigma/\mu e$$
$$n \cong 9 \times 10^{18}\ cm^{-3}$$

It should also be noted that the electron mobility used in the calculation of resistivity carrier concentration is for pristine PbTe. The mobility in the PbTe thin film should be much lower than in bulk PbTe due to increased scattering at grain boundaries. This fact means the carrier concentration calculated is a lower limit and most likely actually higher. Since the resistivity carrier concentration is already approaching the upper limit for undoped PbTe,[104] it can be concluded that measured electrical conductivity is most likely the source of error.

There are several possible reasons for the conductivity measurement to overestimate the actual conductivity of the PbTe thin film. One of the requirements of the Van der Pauw technique is a uniform sample. However, profiliometry indicates that over the length of the sample the thickness changes by around 25%. Since the formula for resistivity is

$$\rho = R\ d\ w/l \tag{6.1}$$

where d is the thickness of the sample, w is the width, and l is the length, the variation in the thickness of sample, which is around 25%, could therefore lead to an error in the resistivity of 25%. While this error by itself is not enough to move the measured power factor within the accepted range of bulk PbTe, there are other possible sources of error. The inhomogeneous nature of the film could also lead to another possible mechanism for an erroneously high conductivity. If there were any cracks or holes in the PbTe layer of the sample, the simple model of two parallel resistors would no longer hold. Current attempting to pass through the PbTe layer would be essentially blocked and pass instead through the Pt layer, as shown in Figure 6. The Pt layer would then dominate the resistivity, essentially creating a short circuit and an apparent increase in conductivity.

The parallel resistor model would then have to be replaced with a new equivalent resistor model that would instead be three resistors in series (PbTe layer, Pt layer, and PbTe layer) invalidating all the previous calculations. SEM images of PbTe films, which will be presented in the following section, provide some evidence for this possible mechanism. This mechanism would also affect the apparent Seebeck coefficient as well. The Seebeck coefficient requires charges to diffuse through the sample. If the current were completely inhibited in the PbTe layer, the Seebeck coefficient measured would be from the Pt substrate only. However, the measured Seebeck is closer to the value expected for PbTe than Pt. With the right degree of cracking, enough charge diffusion should be possible in the PbTe layer to generate the observed Seebeck coefficient, but also lead to a short circuit when the resistivity is measured.

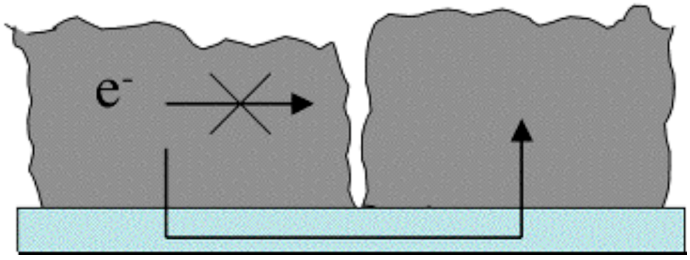

Figure 6-6. Short circuit error in conductivity measurements

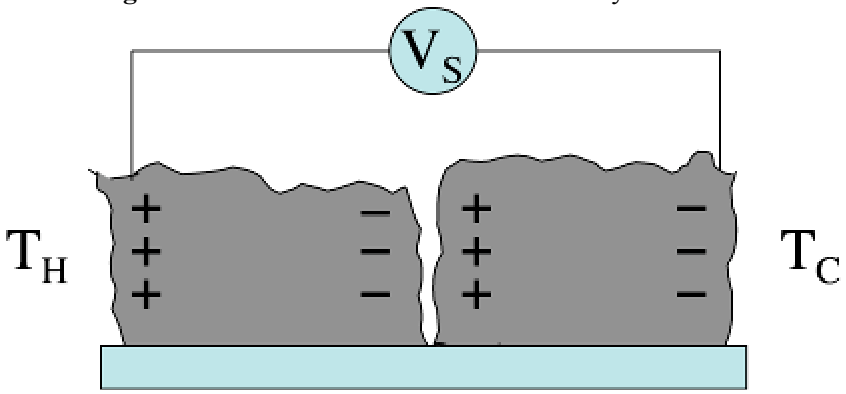

Figure 6-7. Seebeck effect in cracked PbTe film

6.4 Growth Potential Dependence on PbTe Film Properties

Following the discussion of all the possible sources of error, it might be tempting to throw out any further measurements on electrodeposited PbTe films. Taking some simple precautions, however, it is still possible to gather some useful information from these thin film measurements. The results presented in this section ignore the parallel resistor model that might have led to the erroneously high conductivity in the previous section. Instead, all the resistivities are the combined resistivity of the Pt layer and PbTe layer. Assuming the resistivity of the Pt layer does not differ much between samples, the PbTe resistivity should then scale with the total resistance. This makes comparing results between samples possible. The error in the conductivity is determined by the variation of the thickness of the sample as determined by profiliometry. Like the resistance measurements, the Seebeck coefficients reported are the results for the entire sample.

Since the Seebeck coefficient of the Pt/Ti layer is small, the effect of not subtracting it from the measurement is much smaller than in the case of the conductivity measurement.

PbTe thin films were grown at different potentials to determine the effect growth potential has on the resistivity and Seebeck coefficient. Shown in Table 1 are the thickness profiles of the PbTe films studied. Films were grown at –150 mV, -200 mV, -300 mV, and –400 mV all vs 3M Ag/AgCl. All films displayed similar XRD patterns indicating polycrystalline PbTe with no other peaks present besides the Pt substrate. The heights from 6 positions along the sample are reported in nanometers and the mean thickness and standard deviation of the thickness are shown as well. The thickness variation of just the Pt substrate was found to be minimal compared to the roughness of the entire sample. For a comparison to Figure 5, the complete profile of the film grown at –400 mV is also shown in Figure 8.

Position	-150mV	-200mV	-300mV	-400mV	Pt layer
1	12375	7342	9717	6097	634
2	2123	3525	4122	5475	650
3	--	3983	7367	5459	
4	11783	3947	7892	1069	
5	7907	4706	6386	3614	
6	12653		6509	3285	
Mean	9368	4700	6999	4166	642
Standard Deviation	4480	1536	1856	1886	11

Table 6-1. Thickness of PbTe films grown at various potentials

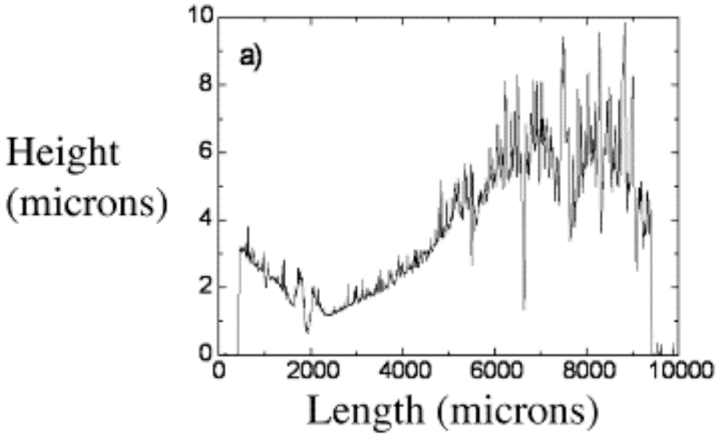

Figure 6-8. Thickness profile of PbTe grown at –400mV

The resistivity of these PbTe films is shown in Figure 9. Notice that there are large error bars on the resistivity values due to the large variation in the thickness of the samples. All of the films displayed nearly the same total resistivity, around 4.0×10^{-4} Ω-cm, regardless of growth potential. Since these values are the resistivities for the entire sample, comparisons to bulk PbTe are not possible. The fact that all the samples have nearly the same total resistivity can be explained in one of two ways. First, the electrical

properties of PbTe films could be independent of growth potentials. However, this seems unlikely since the growth potential has a large effect on a number of film properties, including morphology and grain size, which would likely lead to differing resistivities. Second, and more likely, is the total resistivity of the samples is dominated by the Pt substrate. The measured resistivities would then not change since the Pt layer is identical from sample to sample. This interpretation is supported by arguments made in the previous section.

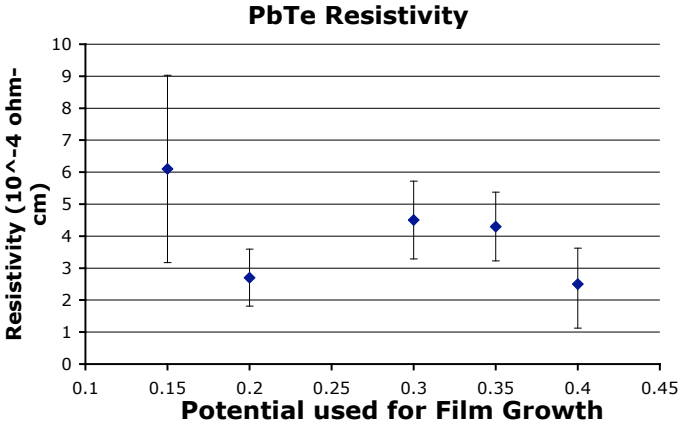

Figure 6-9. PbTe resistivity

The total Seebeck coefficient of the PbTe films is shown in Figure 10. In theory the variation in thickness of the sample should not be as crucial, therefore the error associated with the Seebeck coefficient measurement is estimated to only be on the order of 10%. Films deposited at low and high potentials had a small positive Seebeck coefficient. PbTe grown at intermediate potentials (–300 mV and –350 mV) had a negative Seebeck coefficient. The Seebeck coefficient of samples grown at –300 mV and –350 mV also had the largest absolute magnitude of all the films measured. The most striking feature about this graph is the change in carrier type from p-type to n-type back to p-type with increasing growth potential. This unusual behavior was unexpected and merits further discussion. Several possible explanations, both likely and unlikely, will be examined.

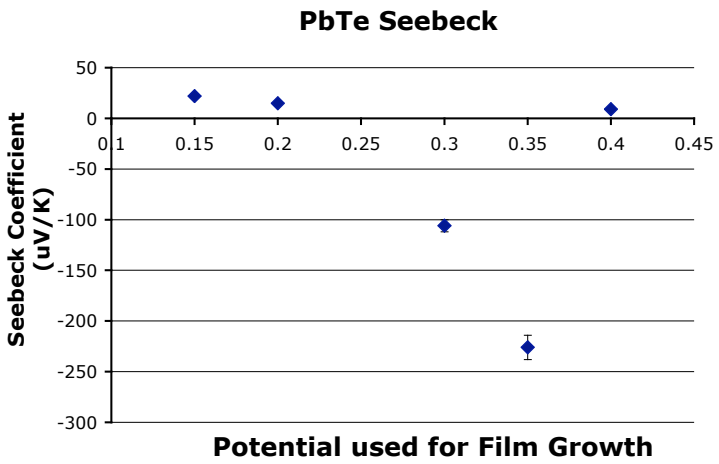

Figure 6-10. Seebeck coefficient of PbTe thin films

One way for the carrier type of PbTe to change is through the Pb to Te ratio. Recall that Te-rich PbTe is p-type, while Pb-rich PbTe is n-type.[104] If the films were to change from Te-rich, to Pb-rich, back to Te-rich, the results in Figure 9 would be expected. However, previous studies on the electrochemical deposition of PbTe films report that over these growth potentials the ratio of Te to Pb should remain constant.[43] This explanation for the change in carrier type therefore seems unlikely.

Recall from the discussion in [6.2] that the degree of oxidation and the number of grain boundaries plays a large role in the transport properties of PbTe thin films. Oxygen can be quickly adsorbed at grain boundaries and act as acceptors leading to p-type conductivity.[85] If the oxidation of the films is determining the carrier type, films grown at low and high potentials should be more heavily oxidized than at intermediate potentials. It should be possible to indirectly track the degree of oxidation in these electrodeposited films through the grain sizes. Since oxygen is preferentially found at the grain boundaries, it follows that the more grain boundaries in a film, the higher the degree of oxidation. Smaller grain sizes, and thus more grain boundaries, would lead to more oxygen adsorbed than the case with large grain sizes. Therefore, films with smaller grain sizes would be predicted to be p-type and films with larger grains n-type. The effect of growth potential on the grain size of electrodeposited PbTe films has not been previously studied. Figure 11 shows the grain size determined by the Debye-Scherrer equation plotted versus growth potential. Dividing lines indicating the carrier type in each potential region are included. The grain size first increases and then decreases with increasing potential. This trend in grain size however does not match the trend observed in carrier type. Unfortunately, the hypothesis that larger grain sizes and thus decreased oxidation lead to n-type conductivity appears to be refuted.

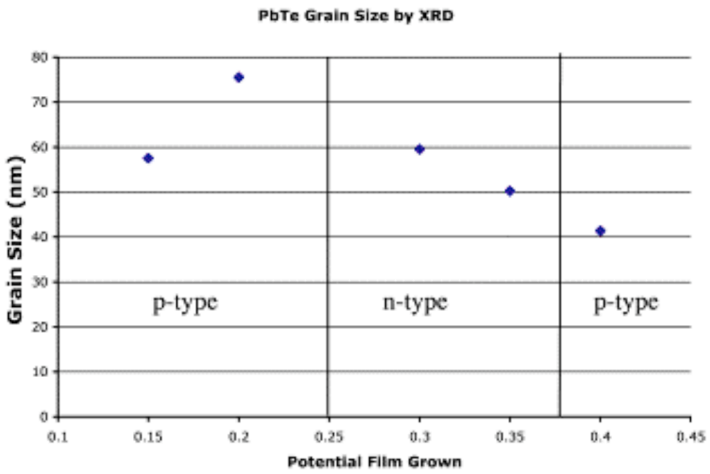

Figure 6-11. Grain size of PbTe thin films

Crystallite morphology of the thin films could also potentially account for the observed carrier type trend. A similar argument to what was made in the previous paragraph can be made for the thin film morphology. A film with high surface area should oxidize more than a film with a comparatively smaller surface area, and therefore display p-type conductivity. A film with numerous small crystallites or crystallites that are spaced far apart should have a higher surface area than a dense, compact film with large crystallites. The morphology of the films was studied by SEM and the images are shown in Figure 12. Note the magnifications are all identical to aid in comparison. There is a clear change in crystallite morphology with increasing growth potential. Films grown at low potentials (-150 mV and –200 mV) are made of a collection of 5-sided stars. As an aside, this 5-fold symmetry is a result of twinning along the (110) axis and is often seen in FCC structure types.[141] Increasing the growth potential, the 5-sided stars become more difficult to make out. At the highest potential (-400 mV) the stars are no longer visible and the size of crystallites has shrunk. The p-type film morphology seems to fall under two general categories, namely 5-sided stars that are spaced fairly far apart or small crystallites that are packed closer together. Both of these morphologies are consistent with a large surface area. The n-type films are comprised of larger crystallites, which appear closer together than in the –150 mV and –200 mV example. Larger and more tightly packed crystallites are indicative of a smaller surface area. Qualitatively, these SEM images seem to support the hypothesis that the surface area is the deciding factor in conductivity type. Of course estimating the surface area of electrodeposited thin films through SEM images is an imperfect science and can be open to interpretation. SEM evidence seems to merely support this hypothesis but does not conclusively prove it.

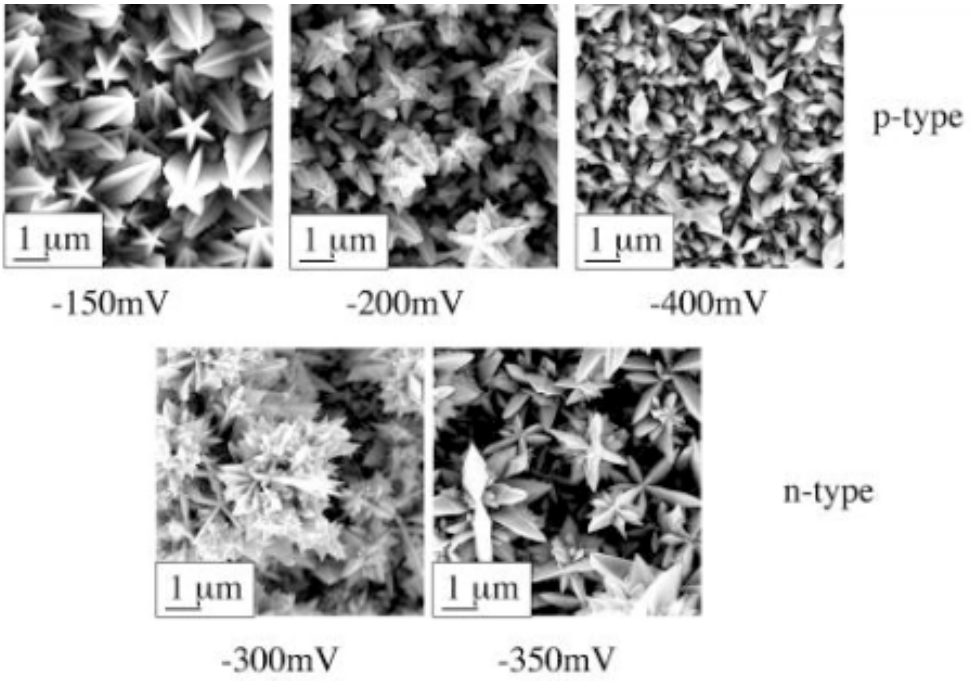

Figure 6-12. Morphology of PbTe films

There is one more possible explanation to justify the results of the Seebeck measurement. All of these measurements require that current be able to pass through the PbTe layer. However, this is not necessarily the case for all films studied. There are three possible current paths. The current can flow through both the PbTe layer and the Pt/Ti substrate like the parallel resistor model used in the previous section. If there were some kind of barrier layer between the PbTe and substrate, the current would only flow through the PbTe layer. Finally, the current can be limited to the Pt/Ti layer because of cracks or holes in the PbTe layer. The path the current travels has a huge effect on the resistivity and Seebeck coefficient measured. If current flow were completely inhibited in the PbTe layer and limited to the Pt/Ti layer, the Seebeck coefficient measured would be mainly from the Pt/Ti layer. SEM images of the film morphologies suggest that holes or cracks in the films are a reasonable possibility, even though none are observed. The samples that are p-type all have small Seebeck coefficients (on the order of 10-20 μVK^{-1}), not that different from the measured Seebeck coefficient of the Pt/Ti substrate ($+1.5\ \mu VK^{-1}$). This fact would seem to suggest current flow in these samples is limited to the Pt/Ti layer. A consequence of this prediction would be a lower measured resistivity since Pt is more conductive than PbTe. With the exception of the film grown at –150 mV, this is in fact the case, though the large error bars on the resistivities make this comparison difficult. N-type films would then result from current that flows through both the PbTe layer and the substrate or just the PbTe layer. However, justifying why the current paths would be so different among the samples is a more challenging proposition without direct SEM evidence of cracks or holes in films. Questions, such as are films grown at –300 mV and –350 mV less prone to cracks or were these samples merely handled more carefully, remain unanswered.

6.5 Conclusions

Electrodeposited films of PbTe grown at –350 mV were measured to have a tantalizingly high power factor. However, errors and difficulties in measuring the resistivity are most likely the cause of this high power factor.

Films of PbTe grown at different applied potentials show largely different Seebeck coefficients. There are numerous possible explanations for the observed results, but only two that are really plausible. The first is that films with large surface areas are more readily oxidized. Oxygen is a know acceptor in PbTe and thus these films have positive Seebeck coefficients. The second is that the positive Seebeck coefficient measured in some films is a result of current flowing mainly through the Pt/Ti layer.

While the results from these thin film measurements are important, extrapolating the lessons learned to nanowires is critical. The fact that surface area of the thin film might affect its properties is particularly relevant. Nanowires of PbTe have a much greater surface area than any of the films studied in this chapter. However, the nanowires are encased in a PAA matrix and therefore should not be exposed to the atmosphere. A question that will need answering is the degree to which the PAA matrix provides protection to oxidation.

Chapter 7: Device Contacts and Nanowire Array Measurements

The ultimate goal of this thesis is to create working thermoelectric devices that have efficiencies higher than bulk. Chapters 3 and 4 presented the synthesis of undoped and doped PbTe nanowires. The next step in creating a device is to create electrical contacts to these nanowires and then measure their thermoelectric properties. For accurate measurements, contacts to a majority of the 10^{10} nanowires per square centimeter must be created. Prior work in the Stacy group on contacting nanowire arrays of $Bi_{1-x}Sb_x$ and Bi_2Te_3 provided a starting point, but challenges still remain. Advancements in the contacting methods will be presented in this chapter along with thermoelectric measurement results.

7.1 Nanowire Array Measurement Introduction

There are two main ways to measure the figure of merit of a thermoelectric material. The first method is to measure the variables individually, the Seebeck coefficient, electrical conductivity, and thermal conductivity, and then insert them into the equation for ZT. The other method is the Harman technique invented by T. C. Harman in 1958.[142] In this technique the ZT is calculated from only the AC resistance and the DC resistance. The Harman equation for ZT is as follows

$$ZT = (R_{DC}-R_{AC})/R_{AC} \quad (7.1)$$

This method relies on the fact that the Seebeck voltage takes time to develop. Under an AC current the voltage measured is only from the voltage drop across the sample. With a DC current, two voltages are generated, one due to the resistance of the sample and the other due to the Seebeck voltage. Comparing the AC resistance and DC resistance thus gives a good estimate of the ZT of the sample. This method is useful for its simplicity, but provides less information on the thermoelectric properties. Measurements on nanowire arrays presented in this chapter employ the Harman technique.

Resistance measurements on nanowire arrays were made after creating top electrical contacts to the nanowires. A description of the contacting process will be provided in the following sections. To measure the R_{AC} and R_{DC} thermoelectric couples were made. The nanowire arrays were diced into 380 μm x380 μm squares and coupled with a bulk thermoelectric, either n-type or p-type. The array and bulk leg are connected electrically in series and thermally in parallel to create a thermoelectric device. A diagram of the setup is shown in Figure 1. Shown in Figure 2 is an optical image of a thermoelectric couple. Also shown in Figure 2 is an SEM image of the nanowire leg. To calculate the AC resistivity of the nanowires, the porosity of the PAA matrix was assumed to be 10% and it was assumed that all of the nanowires were contacted. In the specific cases presented in this thesis the resistance of the bulk leg can be effectively ignored since its resistance is several orders of magnitude lower than the nanowire array.

This method has been used successfully in the case of Bi_2Te_3 and $Bi_{1-x}Sb_x$ nanowire arrays.[143]

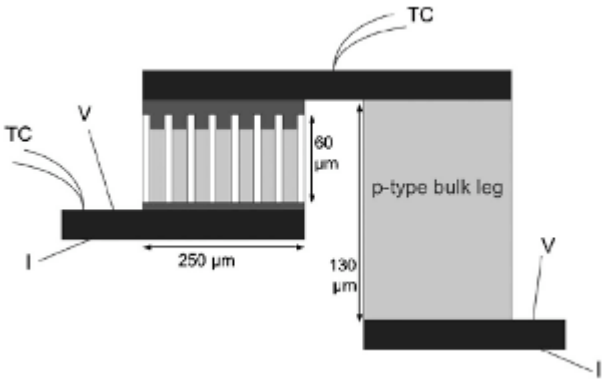

Figure 7-1. Thermoelectric couple[144]

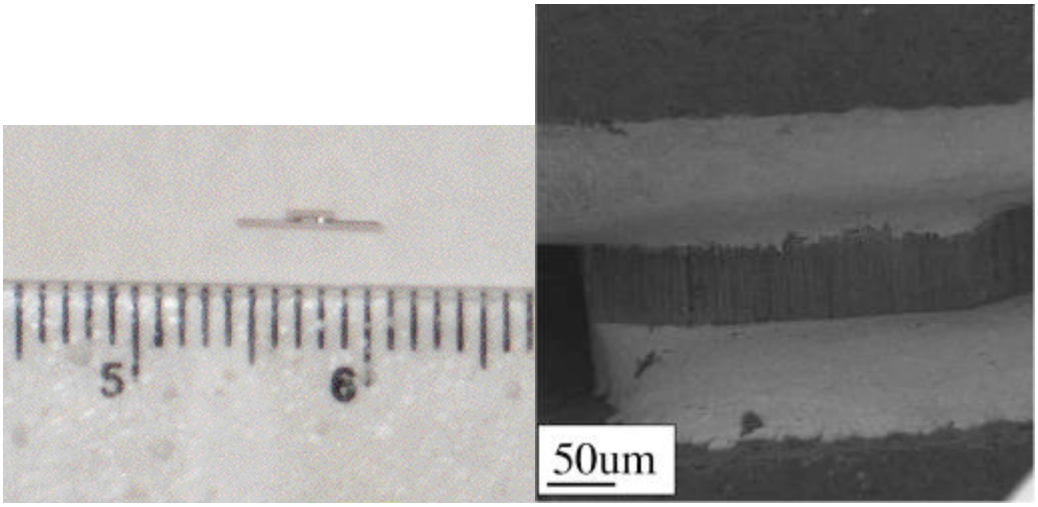

Figure 7-2. Optical image of thermoelectric couple; SEM image of nanowire leg

Resistance measurements were also measured on only nanowire arrays without the bulk leg component. Electrical leads were connected to the top and bottom of the arrays as shown in Figure 3. AC and DC resistances were then measured and the resistivity was calculated from the size of the sample.

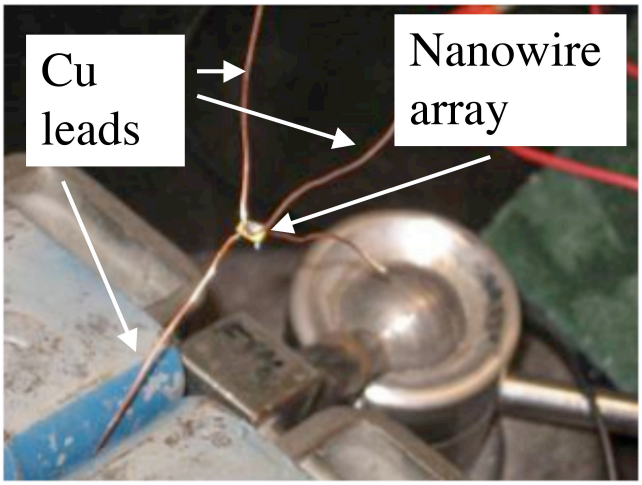

Figure 7-3. Nanowire resistance measurements

Measurements on PbTe nanowire arrays in PAA have never been made, though there have been measurements on single PbTe nanowires. Since only the resistance of the PbTe nanowire arrays is being measured, the resistivity of single nanowires, along with bulk and thin film, are presented for comparison in Table 1.

Nanowire Diameter (nm)	Resistivity (Ω•cm)
60	227.3[145]
83	10[146]
60x200 (square wire)	0.01[147]
73	0.0455[148]
Thin Film (chapter 6)	~0.0005
Bulk	~0.001 to 0.01[72]

Table 7-1. Resistivity of PbTe nanowires

Compared to the bulk resistivity of PbTe, the resistivity of these nanowires are orders of magnitude higher. Assuming typical values of the Seebeck coefficient and thermal conductivity of 275 μVK^{-1} and 2 $Wm^{-1}K^{-1}$, respectively, a resistivity of 0.001 Ω•cm is needed for a ZT of 1. The low conductivity of PbTe nanowires ultimately lowers the ZT below that of bulk.

The reason for the diminshed electrical conductivity of PbTe nanowires is still an active area of research. Evidence in the literature points to several different causes. One concern is that since PbTe has a large Bohr Exciton radius, nanowires with diameters below 100 nm are strongly quantum confined. It is possible in these size regimes electron and hole mobilities are decreased due to increased carrier scattering. However, the thermoelectric power factor is still expected to increase due to the increased Seebeck coefficient. Another contributing factor for decreased conductivity is the oxidation of PbTe nanowires. As discussed in chapter 6, oxidation of PbTe has a large effect on the electronic properties of PbTe. Since the surface to volume ratio is much greater in nanowires, surface oxidation plays an even greater effect than it does in bulk. XPS analysis on PbTe nanowires shows that after 24 hours an approximately 2nm thick oxide layer forms on the surface. While this is a relatively thin oxide layer, a large effect on

conductivity in these PbTe nanowires is observed. Shown in Figure 4 are the effects of time on the conductivity of different size PbTe nanowires. After 24 hours the conductivity of 20 nm PbTe nanowires drops to 39% of the initial conductivity.

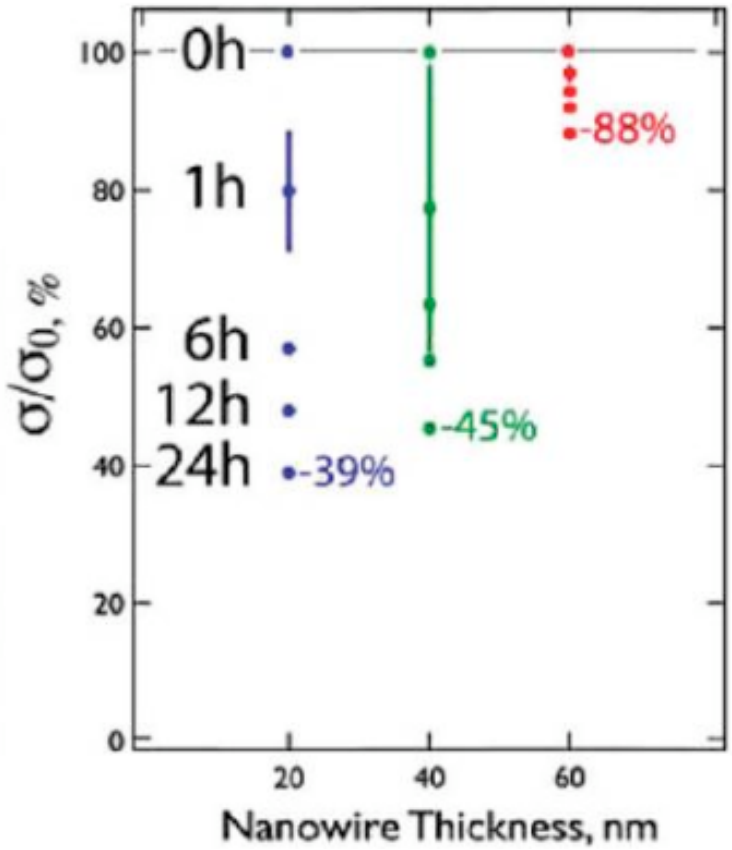

Figure 7-4. Conductivity of PbTe nanowires[85]

Another major factor in the low conductivity of PbTe nanowires is the nature of the electrical contacts. This problem is related to the formation of an oxide layer on PbTe as well. This oxide layer prevents the formation of good electrical contacts to the nanowires. Using galvanic displacement of Au ions on the surface of PbTe nanowires, instead of evaporating a metal contact, increases the conductivity by an order of magnitude.[145] Since Au is more noble than either Pb or Te, Au ions are reduced to metallic Au, while Pb and Te in the nanowire are oxidized to ions and dissolved in solution. This method etches a portion of the nanowire allowing for Au to contact PbTe instead of the native oxide. The issues of oxide formation and good electrical contacting are challenges that have plagued attempts at creating efficient nanowire thermoelectric devices. All of the methods of creating electrical contacts to nanowire arrays presented in this chapter are attempts at solving these problems.

7.2 Creation of Electrical Contacts

The Stacy group has already created electrical contacts to nanowire arrays of Bi_2Te_3 and $Bi_{1-x}Sb_x$. This work served as an important starting point for creating

electrical contacts to nanowires. A description of this contacting procedure and the results of resistance measurements will be presented in this section.

In order to create electrical contacts, the tops of the nanowires must be exposed. This necessitates removing a portion of the PAA matrix. PbTe nanowires are first deposited to fill the PAA template to within a few microns of the top. Then 5-10 μm of the template is etched for 3 minutes with 0.5 M NaOH. The tops of the nanowires are now exposed and free of the PAA matrix. Shown in Figure 5 is an SEM image of a PbTe nanowire array after this step. Notice how the nanowires have begun to clump together due to strong Van der Waals forces.

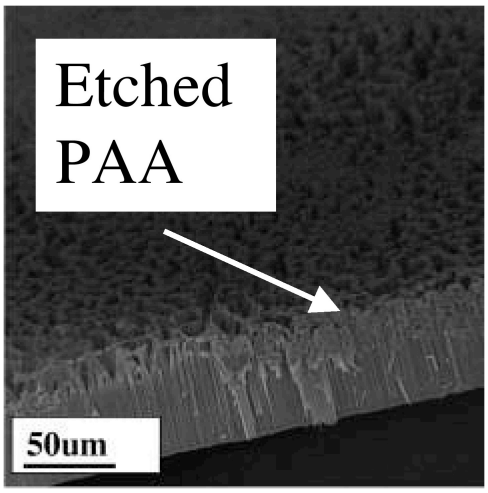

Figure 7-5. Etched PbTe/PAA

Once the tops of the PbTe nanowires are exposed, Ni is electrodeposited onto the tips of the nanowires. Ni was deposited onto the nanowires from a solution of 60 g/L $NiSO_4$ and 22.5 g/L H_3BO_3. A pulsed potential deposition was used. The "on" potential (-1 V vs Ag/AgCl) lasted for 2 seconds. The "rest" potential (-0.6 V vs Ag/AgCl) lasted 4 seconds. Ni was deposited for a total of 1 hour. Shown in Figure 6 is a backscattered SEM image after this electrochemical Ni step. The Ni and PbTe nanowire are marked with white arrows. The Ni forms small nodules on the PbTe nanowires. This Ni serves as the strike for the next contacting step.

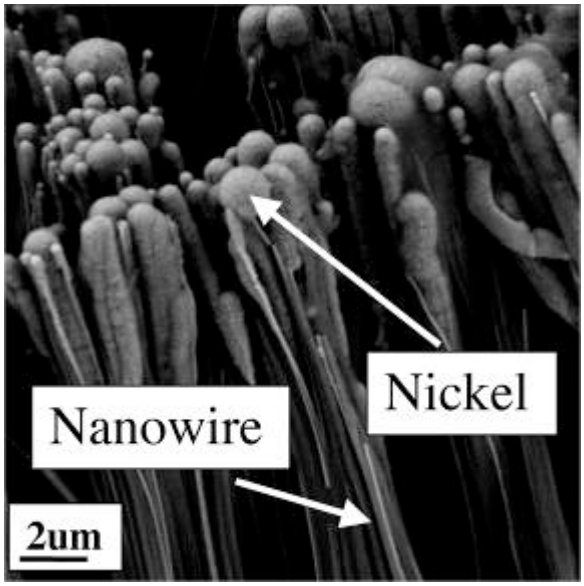

Figure 7-6. Electrochemical Ni on PbTe nanowires

The next step in the contacting process is to deposit a layer of electroless Ni. Electroless Ni is deposited from a solution of $NiSO_4$, lactic acid, potassium citrate, and dimethyl amine borane (DMAB).[149] DMAB serves as the reducing agent, reducing Ni^{2+} ions to Ni. This reduction is catalyzed by the electrochemical Ni deposited in the previous step. The electroless Ni fills in all the gaps left by the electrochemical Ni step, leaving a thick film. Shown in Figure 7 is a SEM image of the electroless Ni layer. This layer is typically 5-10 μm thick.

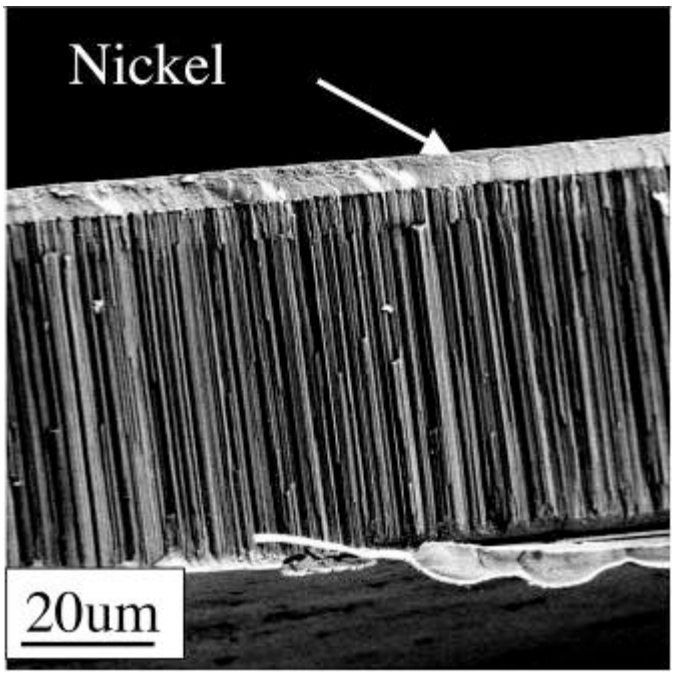

Figure 7-7. Electroless Ni layer on PbTe nanowires

After the electroless Ni step, a thin layer of Au is deposited through a galvanic displacement process, which is also known as immersion Au. A gold layer is deposited in order to create a suitable surface to solder and attach electrical leads. The immersion Au process is as follows; gold ions are reduced while metallic nickel is oxidized to Ni^{2+}. Therefore, Au replaces some of the Ni on the surface. The Au layer is typically around a few hundred nanometers. The thickness of the Au layer is limited by the diffusion of Au ions through the porous immersion Au layer. A backscattered SEM image of the Au layer on the electroless Ni layer is shown in Figure 8. The Au is the brighter contrast layer on top of the thicker electroless Ni layer. Notice at the bottom of the electroless Ni layer there are PbTe nanowires that have been broken during the sample preparation. An optical image of the nanowire array after the immersion Au step is shown in Figure 9.

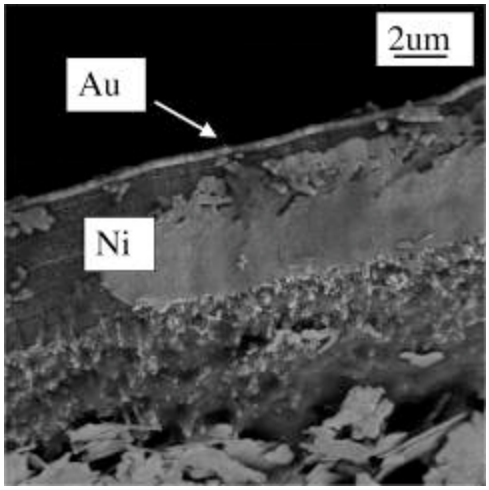

Figure 7-8. Immersion Au layer on Electroless Ni

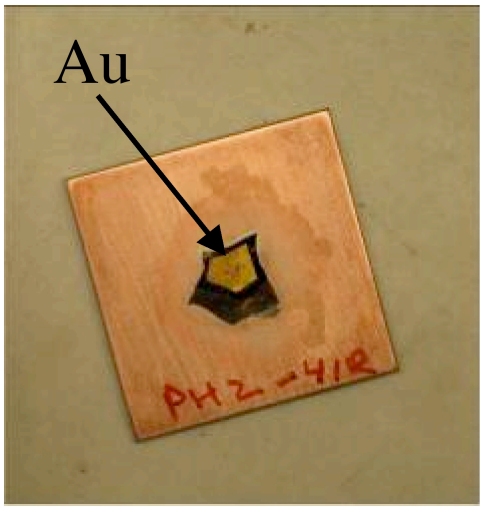

Figure 7-9. Optical Image of Immersion Au

Once the immersion Au layer is deposited, AC resistance measurements were conducted. Several samples were synthesized and measured. The average resistivity of the samples was calculated. Samples with a total resistance greater than 1 kΩ were discarded as a failed attempt at contacting. The resistivity of the PbTe nanowires was 11

ohm-cm +/- 6 Ω•cm. The success rate of electrical contacting was 50%. The "success" rate is a relative term because even the samples considered a success and used in the average calculation still had resistances far too high for a good thermoelectric device, and therefore the Harmen technique was not used. The resistivity of the PbTe nanowires is orders of magnitude higher than bulk values but consistent with some of the resistivity measurements on single PbTe nanowires.

7.3 Electrical Contacts with a Phosphoric Acid Etch Step

In order to improve the electrical contacts to the PbTe nanowires a different etchant was used to dissolve the PAA matrix and expose the nanowire tips. During the etching step, the concern is that the surface of the PbTe nanowires is prone to oxidation. This would lead to a large contact resistance and a higher resistivity.

The Pourbaix diagram of PbTe reveals that PbTe is more susceptible to oxidation at higher pH values.[150] A 10% phosphoric acid was used to etch the PAA matrix to test whether an acidic solution would minimize the formation of any oxidation layer and thus reduce the contact resistance.

A possible indication that oxide formation is lower in the case of a phosphoric acid etch as opposed to a sodium hydroxide etch is found in the current response during the electrochemical deposition of Ni. Shown in Figure 10 is the current response per unit area of the deposition of Ni after a phosphoric acid and sodium hydroxide etch. The current is larger when a phosphoric acid etch is used. Since both etch steps were designed to remove approximately the same amount of PAA, it can be concluded that the higher current is due to less oxidation of the nanowire surface.

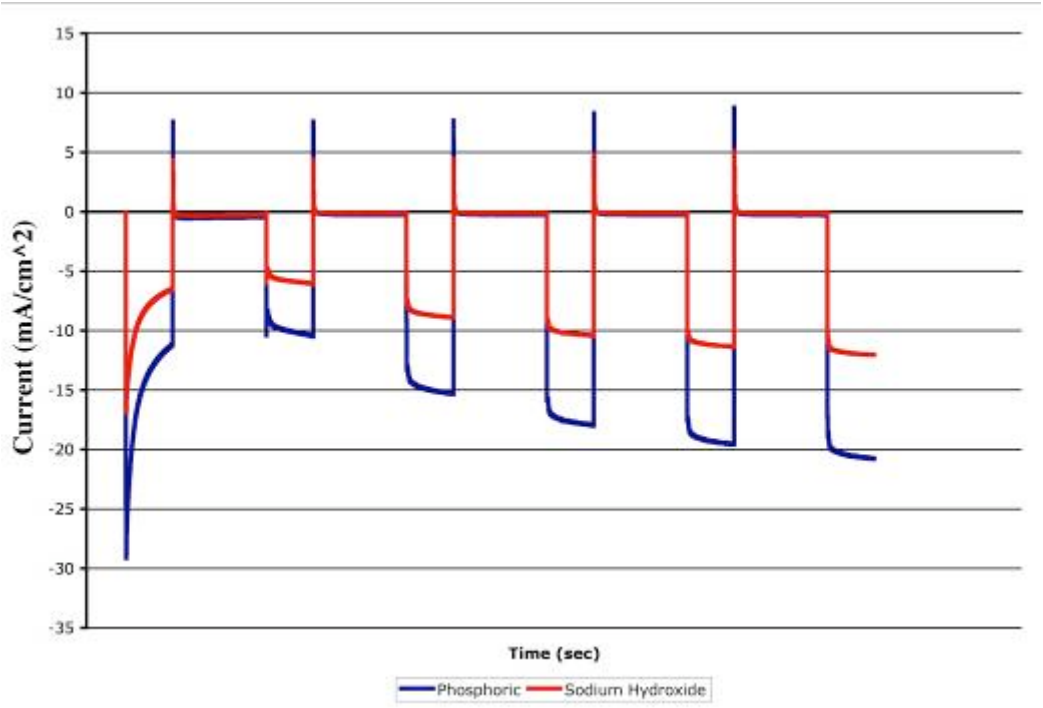

Figure 7-10. Current response of electrochemical Ni deposition

After the phosphoric acid etch, the same contact procedure described in the previous section was used to create electrical contacts. Like the previous analysis, samples with a total resistance greater than 1 kΩ were categorized as failures. The resistivity of the PbTe nanowires with a phosphoric acid etch was 7.7 Ω•cm. The success rate with a phosphoric acid etch however was only 14%. Because of this low success rate, it was not possible to determine the error in this resistivity. While this resistivity is slightly lower than the sodium hydroxide etch, the success rate is much lower. However, because of the slightly better resistance and better current response in the electrochemical Ni step, phosphoric acid was used as an etchant for future work, despite the low success rate.

7.4 Resistivity of Indium and Thallium Doped PbTe Nanowire Arrays

There is another possible explanation for the high resistivity of the PbTe nanowires. The carrier concentration of the nanowires could be too low for suitable electrical conduction. Electrically contacting and measuring the AC resistance of doped PbTe nanowires should answer whether the carrier concentration merely needs to be increased.

Nanowires of PbTe doped with either Tl or In were contacted using a phosphoric acid etch and the same contacting procedure used in the previous section. The resistivity of thallium doped PbTe was 1.7 Ω•cm. The resistivity of the indium doped PbTe was 2.7 +/- 1.2 Ω•cm. These resistivities are slightly better than in the un-doped case, but are still orders of magnitude higher than bulk and still much too high for a workable thermoelectric device. While increasing the carrier concentration does lead to a better conductivity, improvements are needed. New approaches to contacting the PbTe nanowires are explored in the following sections.

7.5 PbTe/Ni Nanowire Devices

While using phosphoric acid as an etchant slightly improved the resistivity of the PbTe nanowires, further improvements are needed. An oxide layer could still be forming leading to poor conductivity. A method that does not expose the PbTe nanowires to the etching solution should prevent the formation of an oxide layer. Using a thicker PAA template, it is possible to prevent the PbTe nanowires from being exposed to the etching solution.

PbTe nanowires were deposited into an 80 μm thick PAA template to a length of 60 μm. Then Ni nanowires were deposited onto the PbTe nanowires filling the remaining unfilled portion of the PAA template. Using phosphoric acid, the PAA template was then etched approximately 10μm. Since the top of the PAA template is comprised of only Ni nanowires, the PbTe is protected in the PAA matrix and never exposed to the etching solution. After etching, electroless Ni and then immersion Au was used to create a contacting layer. SEM images of an example of this method of contacting are shown in

Figure 11 are. The PbTe nanowires are approximately 60 μm long, followed by at least 12 μm of Ni nanowires, and then 9μm of electroless Ni.

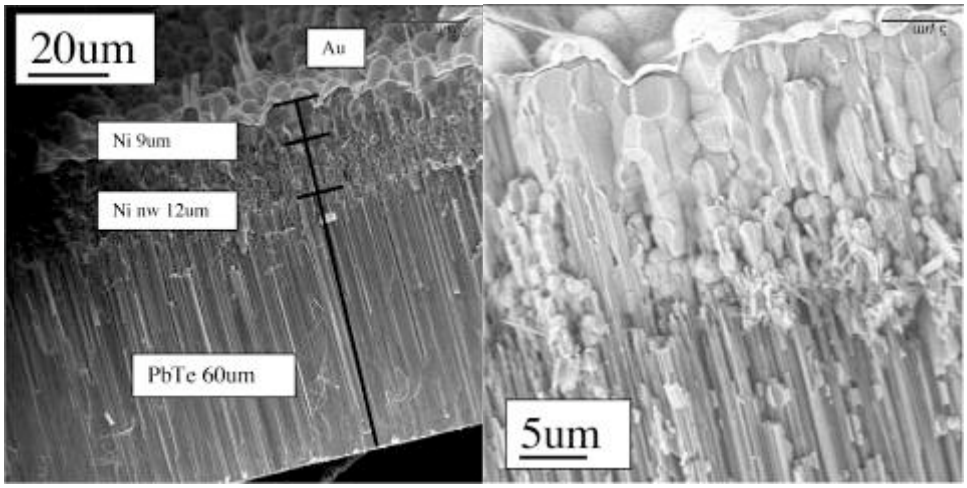

Figure 7-11. PbTe/Ni nanowire contacting method

The resistivity of the PbTe nanowires with this contacting method was 0.65 Ω•cm. While this value is a further improvement from the previous contacting method, it is still much too high for thermoelectric devices.

7.6 Immersion Au Contacting of PbTe Nanowires

Recently, it was discovered that using an immersion Au technique directly onto PbTe nanowires improved their conductivity by an order of magnitude compared to a metal evaporation process.[148] Since the Au immersion process involves the removal of some Pb and Te from the surface of the nanowires, it effectively cleans the native oxide coating. This method was tested to see if it could improve the conductivity of these nanowire arrays.

The immersion Au solution is a basic solution so it can also serve as a PAA etchant. Shown in Figure 12 is an SEM image of PbTe nanowires that have been placed in the Au immersion solution for 24 hours. The PAA template has been etched back exposing the nanowires for contacting. Spherical gold particles are visible on the PbTe nanowires.

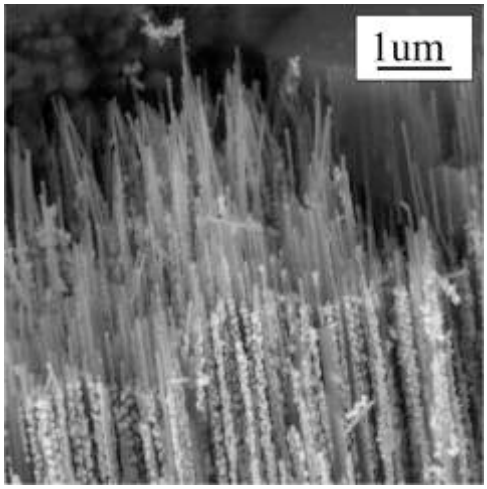

Figure 7-12. Immersion Au on PbTe nanowires

Following the immersion Au step, electrochemical Ni was deposited, followed by electroless Ni, and finally another layer of immersion Au. The resistivity of these PbTe nanowires was 0.5 Ω•cm, roughly equivalent to the resistivity for the technique described in the previous section. Unfortunately, immersion Au did not lead to the improved conductivity anticipated from the literature.

7.7 Conclusions and Future Work

A summary of the results from this chapter is included in Table 2.

Contacting Method	Resistivity (Ω•cm)
NaOH etch	11 +/- 6
H_3PO_4 etch	7
Tl doped PbTe	1.7
In doped PbTe	2.7 +/- 1.2
Ni nanowires	0.65
Immersion Au	0.5

Table 7-2. Summary of results

The best measured resistivity was found to be around 0.5Ω•cm for the sample contacted with immersion Au. This value is on par with results found in the literature, but still much larger than the expected bulk value. Even with numerous attempts at preventing the oxidation of PbTe nanowires, high-quality electrical contacts could not be created. While it is possible that a native oxide layer is still forming on nanowires, there is another possible cause for the high resistances. All calculations of the resistivity of the nanowires assumed that 100% of the pores in the PAA template have nanowires and 100% of these nanowires were contacted. However, for most depositions, nanowires nucleate in only ~ 90% of the available pores. Also, it is impossible to determine the actual percentage of these nanowires that are contacted. Taking into account these

considerations, the actual resistivity of the PbTe nanowires could be much lower. It is unlikely, however, that theses considerations would adjust the resistivity to the expected bulk value.

Measurements of the electronic properties of a single PbTe nanowires are needed in the future to determine the likely cause of the high resistances in nanowire arrays. If the electrical contacting methods used in this chapter can be applied to contacting a single nanowire, it is most likely that too few nanowires of the array are being contacted. If however, the single nanowire measurement still exhibits high resistances, it is most likely the nature of the electrical contacts or the oxidation of the nanowires.

Chapter 8: Electropolymerization of Polyaniline for Low Thermal Conductivity Polymer/Nanowire Hybrids

All of the results presented in this thesis have only been possible through the use of porous anodic aluminum templates. Without the properties of PAA, i.e. self-ordered parallel pores that can span several hundred micrometers, nanowires and thermoelectric devices could not be created. But as functional as the PAA template is in creating and housing nanowires, it actually has a parasitic effect on the efficiencies of nanowire/PAA hybrid thermoelectric devices. This chapter will present a method to overcome the losses associated with using a PAA template through the synthesis of PbTe/polyaniline core-shell nanostructures.

8.1 PAA Templates and Thermoelectric Efficiency

Recall that the thermoelectric efficiency of a device is determined by the figure of merit or zT, with the equation for zT as follows

$$zT = (S^2 \sigma T)/\kappa \tag{8.1}$$

with S the Seebeck coefficient, σ the electrical conductivity, and κ the thermal conductivity. Because of quantum confinement effects and increased phonon scattering, nanowires are predicted to have large zT's. However, measurements reported in chapter 7 on nanowire/PAA hybrid thermoelectric devices indicated no increase in zT. The problems mentioned in chapter 7 such as high contact resistance, insufficient number of wires contacted, and oxidation certainly all contribute to these low efficiencies. However, another problem inherent in the device is the high thermal conductivity of the PAA template. Since thermal conductivity is in the denominator of the equation for zT any increase in thermal conductivity will lead to a lower zT. A unique aspect to the PAA problem, unlike the problems associated with the electrical connections, is that it is possible to calculate the efficiency losses caused by using PAA.

The thermal conductivity of PAA has been reported to be 1.7 $Wm^{-1}K^{-1}$.[151] While this value is small, it is still much greater than the thermal conductivity of the nanowires. Because of this, the alumina serves as thermal shunt negating the benefits of the low thermal conductivity of the nanowires. Using a simple effective medium model the consequence of the PAA matrix can be calculated.[152] The ZT of the PAA/nanowire matrix is given by

$$ZT_{comp} = ZT_{nw} \{1+ (\kappa_m/\kappa_{nw})[(1/f_{nw})-1]\}^{-1} \tag{8.2}$$

where ZT_{comp} is the ZT of the composite, ZT_{nw} is the ZT of the nanowires, κ_m the thermal conductivity of the matrix, κ_{nw} the thermal conductivity of the nanowires, and f_{nw} the volume fraction of nanowires. For 40 nm porous alumina, the volume fraction of pores is around 10%.[153] Assuming optimistic values of 4 and 0.25 $Wm^{-1}K^{-1}$ for ZT_{nw} and κ_{nw} respectively, the expected composite ZT was calculated for different values of κ_m. The

results of the calculations are displayed in Table 1. Since the hybrid thermoelectric devices are mostly alumina (90%), the thermal conductivity of the matrix has a very large effect on the overall ZT. For the measured thermal conductivity of PAA, the composite ZT would shrink to 0.06 even with nanowires with a ZT of 4. However, if the PAA were replaced with air, which has a thermal conductivity of 0.025 $Wm^{-1}K^{-1}$, the ZT of the composite would be over 2.

ZT_{nw}	κ_m	κ_{nw}	f_{nw}	ZT_{comp}
4	1.7	0.25	0.1	0.06
4	1	0.25	0.1	0.11
4	0.75	0.25	0.1	0.14
4	0.5	0.25	0.1	0.21
4	0.25	0.25	0.1	0.40
4	0.10	0.25	0.1	0.87
4	0.025	0.25	0.1	2.11

Table 8-1. Composite ZT

8.2 Strategies For Replacing PAA

From the calculations in the previous section, there are two ways to reduce the parasitic losses due to the matrix; either decrease the thermal conductivity of the matrix or increase the fraction of nanowires in the composite. The obvious solution is to just find a new template material that has both a lower thermal conductivity and higher porosity. However, the PAA templates are extremely unique in their ability to form well-ordered nanopores and no suitable replacement exists. Because no other template exists, any solution to the problem must work within the confines of PAA.

One possible solution is to completely dissolve the PAA template after depositing the nanowires. This method would replace the high thermal conductivity of the PAA matrix with air, corresponding to the last row in Table 1. An illustration of this method is shown in Figure 1A. The problem with this method, however, is once the PAA matrix is removed the wires will immediately begin to clump together due to strong Van der Waals attractions. Once the wires are clumped together, electrons are no longer confined to one nanowire and therefore the benefits of quantum confinement are diminished.

A better solution would be to have an insulating spacer between the nanowires to prevent the loss of quantum confinement as shown in Figure 1B. One common method in the literature is to dissolve the PAA template and then fill the free space with an insulating polymer. The thermal conductivity of polymers is higher than air but typically on par with thermoelectric nanowires.[154] This method is not without problems however. Specific precautions must be taken to prevent the wires from bunching together before the insulating polymer is added. Also, this method often encases the entire array in the insulating polymer matrix. In order for a device to be made, electrical contacts must be made to the top of the nanowires, which is very difficult if they are buried in a polymer matrix.[152]

A strategy to work around some of these issues is to first deposit insulating polymer nanotubes, then deposit the thermoelectric nanowires inside these nanotubes, and finally remove the PAA matrix. This method along with the other strategies to replace the PAA matrix is illustrated in Figure 1. There are numerous benefits to the method outlined in Figure 1C. Thermoelectric nanowires can be grown slightly longer than the polymer nanotubes thus allowing for easy electrical contacting. In addition, the polymer coating on the nanotube will keep each nanowire electrically isolated. Also, the majority of the matrix in this case will be air, which has a lower thermal conductivity than any polymer. The polymer nanotubes also decrease the diameter of the thermoelectric nanowires, which should improve the nanowire ZT further. The only potential drawback with this method is the structural support provided by the PAA or the insulating polymer will be gone. Leaving a small portion of the PAA template near the edges to serve as structural support, though, should sufficiently protect the device.

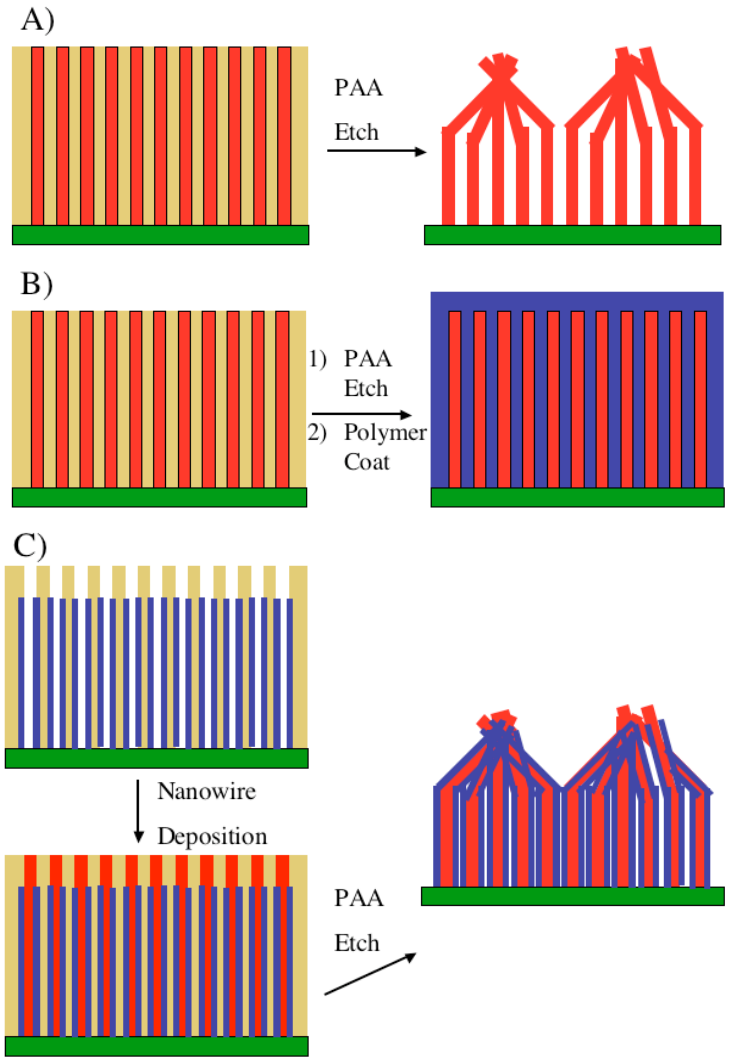

Figure 8-1. Methods for replacing PAA; A) remove PAA; B) remove PAA and replace with insulating polymer; C) deposit polymer nanotube and then thermoelectric nanowire and remove PAA

8.3 Polyaniline Properties

The strategy for replacing the PAA matrix described in the previous section requires a polymer with specific properties in order for it to be successful. These criteria will guide the selection of an appropriate polymer. The polymer should have a low thermal conductivity. It should also be insulating in at least the radial direction to insulate the nanowires. For actual devices the polymer synthetic method should also be scalable and cost effective.

While there might be several polymers that match all of these criteria, polyaniline was selected as an ideal candidate. Polyaniline is a semiconducting polymer comprised of the monomer aniline that was first synthesized 150 years ago.[155] Polyaniline has been investigated for a range of diverse applications, such as supercapacitors, electrochromics, and anti-corrosive coatings.[156] The electronic and thermal properties of polyaniline match well with the desired characteristics. The thermal conductivity of polyaniline is low, around 0.1 to 0.5 Wm-1K-1.[157,158] The electrical conductivity along the length of the chain is highly tunable, ranging from 10^{-10} to 10 S/cm. The conductivity of the polymer changes depending on the degree of oxidation and also protonation.[159] Shown in Figure 2 are three different oxidation levels in polyaniline. Interestingly, the color of the polymer also changes from white to green to blue with increasing oxidation. Additionally, the electrical properties of polyaniline are highly anisotropic, with conduction occurring mainly along the polymer chain, as one would expect.[160] Conduction between the polymer chains is limited, which should electrically isolate the thermoelectric nanowires. Moreover, by adjusting the electrical conductivity it is possible to create polyaniline with a measurable, albeit small, zT.[161] Recent work on other conducting polymers suggests that with more research this zT could be increased.[162]

The final factor in selecting polyaniline concerns the required synthetic method. A discussion on the ability to synthesize polyaniline, both in general and in nanotube form, will be presented in the next sections.

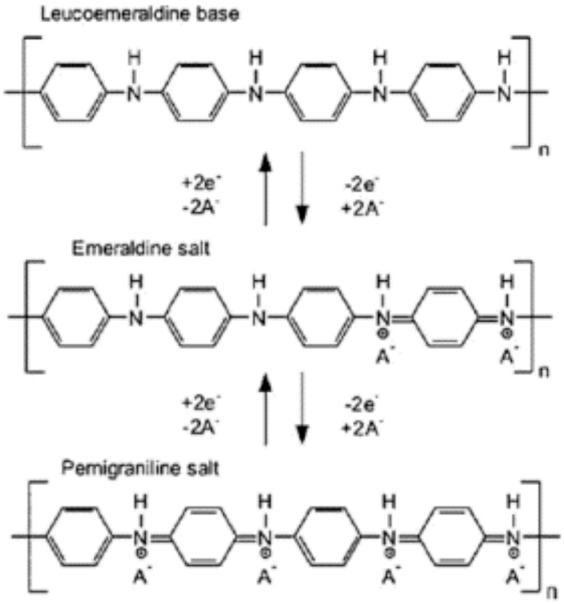

Figure 8-2. Oxidation states of polyaniline[163]

8.4 Electropolymerization of Polyaniline

Polyaniline can be synthesized by electrochemical deposition from an aqueous solution. The process is both scalable and cost effective. The electrochemical oxidation of aniline to polyaniline has been widely studied and the deposition mechanism has already been worked out.[164] Shown in Figure 3 is the CV of a solution of 0.3 M aniline and 1 M HCl. The four reduction/oxidation peaks have been labeled. The peak corresponding to the reverse reaction is marked prime. The electrochemical reactions corresponding to the marked peaks are shown in Figure 5. Peaks A and D are the one-electron oxidation of the end aniline unit on the polyaniline chain. Peaks B and C are the two-electron oxidation of hydroquinone and p-aminophenol, respectively. Hydroquinone and p-aminophenol are byproducts of the hydrolysis of polyaniline, which will be discussed in a later section.

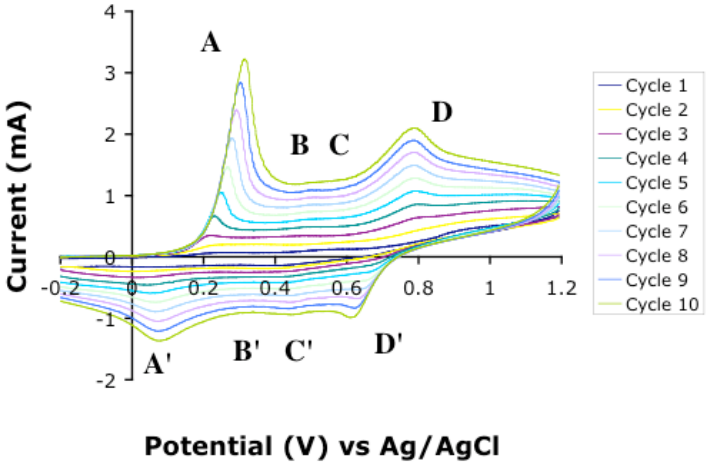

Figure 8-3. CV of polyaniline solution

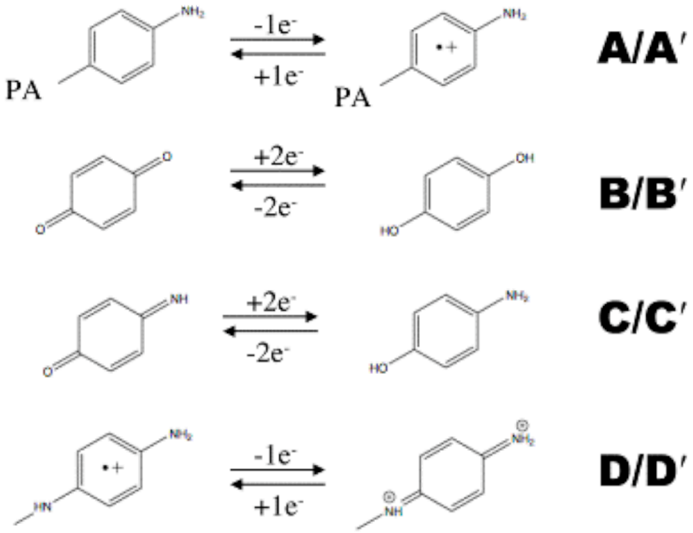

Figure 8-4. Electrochemical reactions of polyaniline

Growth of the polyaniline chain occurs through addition of aniline to the oxidation product of reaction D. The mechanism of the reaction is shown in Figure 5. For polyaniline to be deposited the applied potential must be large enough (~+800 mV vs Ag/AgCl) to generate the oxidation product of D. Below this potential, polyaniline can not be deposited.

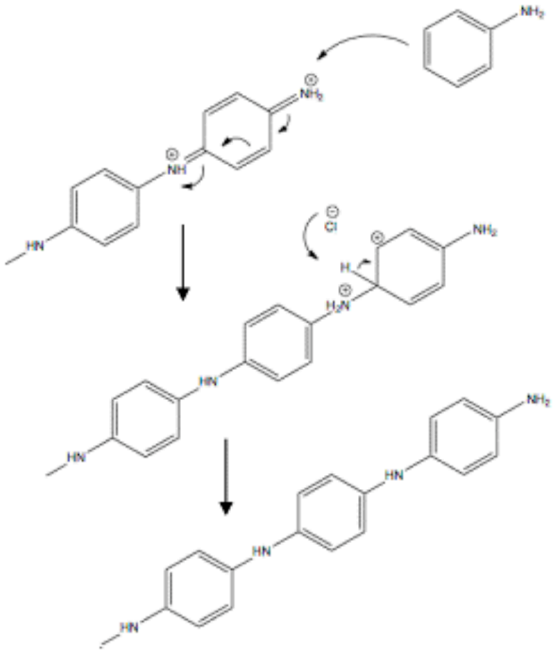

Figure 8-5. Growth mechanism of polyaniline

8.5 Synthesis of Polyaniline Nanotubes

Not only does polyaniline synthesis need to be scalable and cost effective, it also must produce nanotubes inside a PAA template. Nanotubes will result from electrochemical deposition into PAA only if the interaction between the pore wall and polymer is sufficiently strong. For polyaniline this is in fact the case and the first report of electrodeposited polyaniline nanotubes was in 2000,[165] though chemical approaches have been around longer.[166] Since then polyaniline nanotubes have been deposited in templates with a variety of pore sizes. The majority of nanotubes have been deposited in templates with larger sized (100-200 nm) pores,[167,168] but depositions with pore sizes of 10-60 nm[169] have also been reported. However, the template thickness in the case of the smaller pore sizes has only been on the order of 10 μm, compared to the 60-100 μm thick PAA templates used in this thesis. The reason for the use of thinner templates in these reports will become clear later.

Recently researchers have even begun to deposit electrochemically other materials into these polyaniline nanotubes. The diameters of these core-shell structures have all been 100-200 nm, much larger than needed for quantum confinement, and with one exception all reports have deposited a simple metal (Fe,[170] Ni,[171] Cu,[172] or Co[173]) into the polyaniline nanotubes. The one exception is Bi_2Te_3/polyaniline nanowires, which

might have interesting thermoelectric properties if they had been measured.[174] The goal of this chapter is to extend these reports to smaller size pores, thicker templates, and PbTe nanowires for improved thermoelectric devices.

8.6 Ultra-High Aspect Ratio Polyaniline Nanotubes

Initial attempts at extending the electropolymerization of polyaniline to 60 um thick, 40 nm pores PAA templates were all unsuccessful. Visually the templates appeared unchanged after deposition and no nanotubes were seen under SEM. Both potentiostatic and galvanostatic depositions were conducted but neither proved successful. However, it is possible to reproduce the results found in the literature in templates with larger pores. Shown in Figure 6 is an SEM image of polyaniline electrodeposited into a template with larger pores. The top of the template has been etched slightly in a 10 % NaOH solution to expose the nanotubes. The outer diameter of the nanotube is around 300 nm and the inner diameter is around 130 nm. Unfortunately, these diameters are not small enough for quantum confinement effects to be observed.

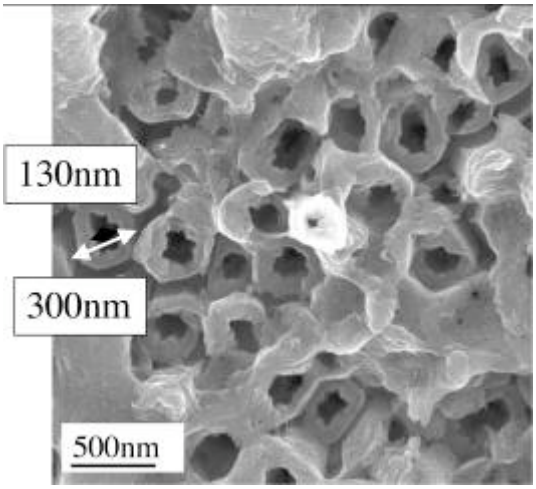

Figure 8-6. Large diameter polyaniline nanotubes

In order to deposit polyaniline into smaller sized pores a better understanding of the differences between depositing in large vs small pores is needed. One major difference between depositing into 40 nm pores and 300 nm pores is the rate of diffusion down the pores. Aniline in solution will diffuse much more slowly down the 40 nm pores compared to the 300 nm pores. In most cases, this difference in the rate of diffusion only changes the growth rates of the nanowires, but in the case of polyaniline the situation is very different. Recall that in the discussion of the electrochemistry of polyaniline there were two peaks that corresponded to the oxidation/reduction of byproducts of polyaniline hydrolysis. At around 800 mV, polyaniline is oxidized and has a quinoid end unit. Under normal growth conditions, this end group reacts with an aniline monomer as shown in Figure 5. However, there is a competing process that becomes important in 40 nm templates, specifically the hydrolysis of the end unit of polyaniline. The hydrolysis mechanism is shown in Figure 7.[175] The best working

hypothesis to explain the difficulties in depositing polyaniline into smaller sized pores invokes this hydrolysis mechanism. As the pore size is decreased aniline diffusion to the working electrode becomes slower. Since the concentration of aniline at the bottom of the pores is very low, the end unit of the growing polymer chain is hydrolyzed instead, thus limiting growth. This hypothesis would also explain why the only reports of polyaniline deposition into smaller pores used thin templates. With thinner templates diffusion down smaller pores becomes less of an issue.

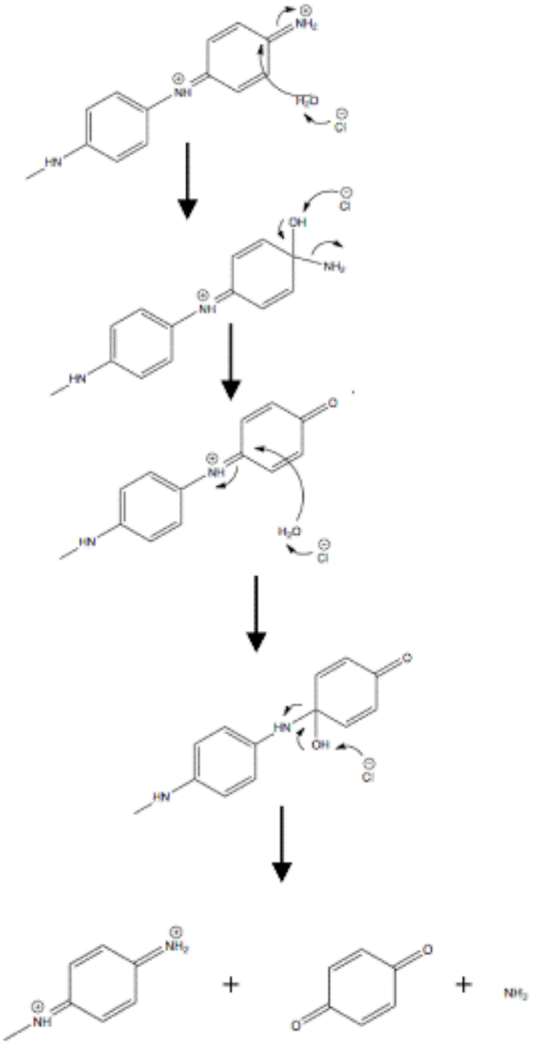

Figure 8-7. Hydrolysis of polyaniline

To test this hypothesis, polyaniline was deposited into 40 nm pores using a pulsed potential deposition. Pulsed potential depositions have been used many times in polyaniline thin films but never for nanotubes.[176,177,178,179,180,181] The applied potential was held at 850 mV for 1 second and then lowered to 140 mV for 5 seconds. The current response of this potential waveform is shown in Figure 8. During the 850 mV pulse polyaniline is oxidized to allow for the growth of the polymer chain. During the 140 mV pulse, polyaniline is reduced, changing the end unit from a reactive quinoid group to a less reactive aromatic end unit. The potential is held at 140 mV for 5 seconds to allow

time for polyaniline to diffuse down the nanopores, and since the end unit is now aromatic, no degradation occurs.

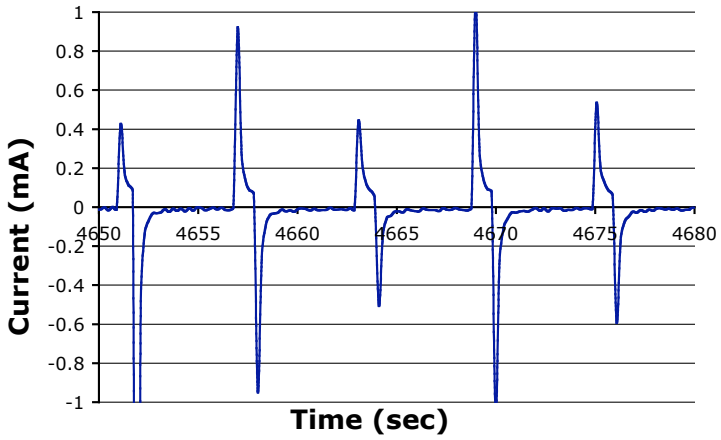

Figure 8-8. Current response of pulsed potential deposition

Shown in Figure 9 is the optical image of the 40 nm PAA template after the pulsed potential polyaniline deposition. Unlike the galvanostatic and potentiostatic attempts, the template appears green in color, indicative of polyaniline in its conductive emeraldine state.

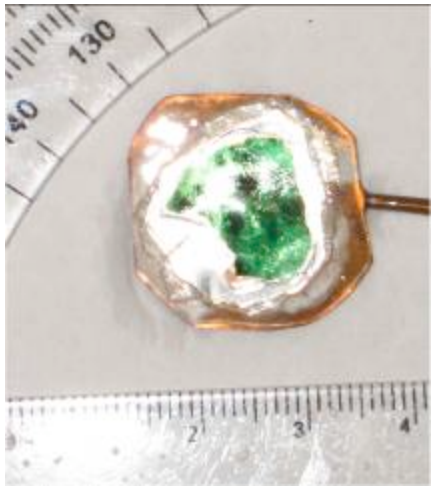

Figure 8-9. Optical image of polyaniline filled PAA template

Shown in Figure 10 are cross-sectional SEM images of the polyaniline filled template. From these images it is difficult to confirm polyaniline is in fact nanotubes and not nanowires. However, back-scattered SEM images presented in the next section suggest nanotube formation. The polyaniline nanotubes have diameters ranging from 50-100 nm. The larger diameter nanotubes could be a result of possible expansion as the tubes poke out of the PAA template. A nanotube with a length around 35 μm was observed indicating polymer growth is not limited by hydrolysis. The density of the nanotubes appears quite low, but this is most likely a result of nanotubes falling out of the

PAA template. Dissolving the PAA template completely in a 10 % NaOH solution reveals a large number of nanotubes, as shown in Figure 11.

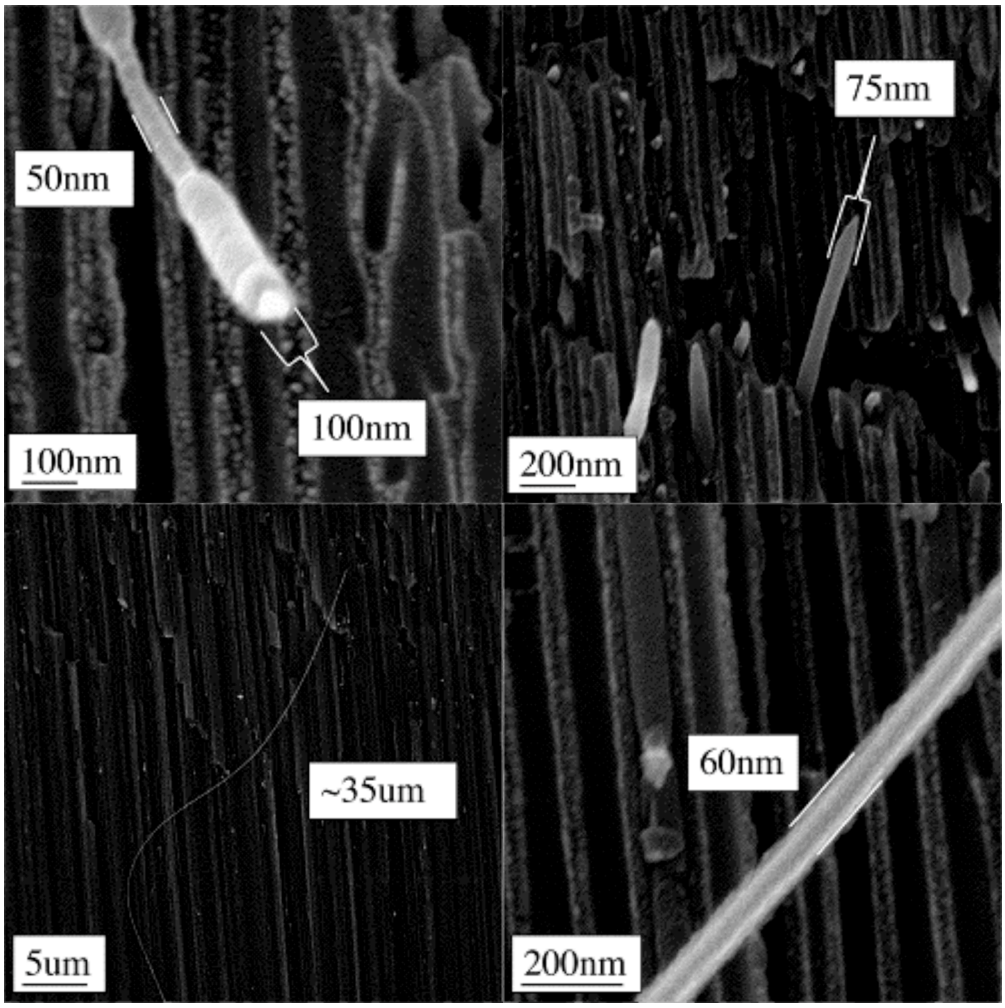

Figure 8-10. Cross-section SEM image of polyaniline nanotubes

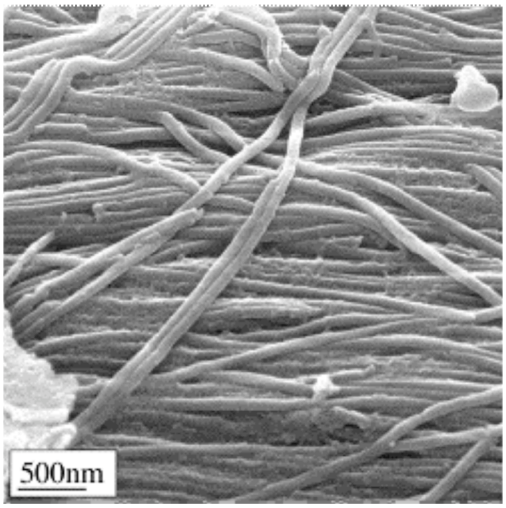

Figure 8-11. Polyaniline nanotubes removed from the PAA matrix

Using a pulsed potential technique, polyaniline could be deposited into 40nm PAA templates. This is the first report of using a pulsed potential technique to produce extremely high aspect ratio polyaniline nanotubes inside PAA. These nanotubes are small enough where the benefits of quantum confinement effects should be significant. Additionally, these nanotubes are long enough that a practical thermoelectric device would be possible.

8.7 PbTe Deposited into Polyaniline Nanotubes

Using the method for PbTe nanowires outlined in chapter 3, PbTe was deposited inside polyaniline nanotubes created by a pulsed potential deposition. After depositing PbTe the template changed in color from green to black, which is typical of a filled PbTe template. The optical image of the PbTe/polyaniline template is shown in Figure 12. XRD analysis indicates the PbTe nanowires are oriented in the (111) direction and no secondary phases were observed.

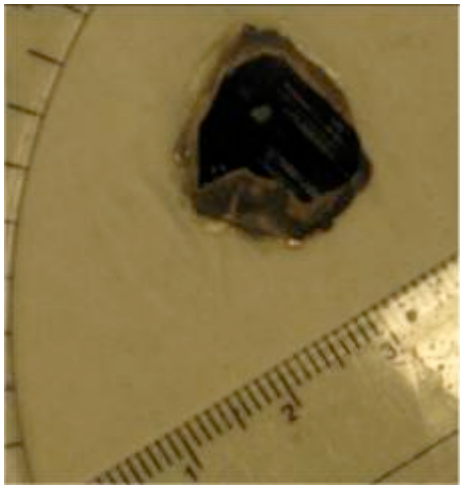

Figure 8-12. Optical image of polyaniline/PbTe filled PAA template

A back-scattered SEM cross section of the sample is shown in Figure 13. The polyaniline in the image appears nearly transparent, which is characteristic of nanotubes and not nanowires. PbTe are the brighter nanowires in the image. Due to the transparency of polyaniline in this back-scattered SEM image it is difficult to determine whether PbTe is actually filling the nanotubes. It is possible that PbTe deposits only in pores of the PAA template that have not been filled with polyaniline nanotubes. Secondary electron images of the sample do not provide any clarification since it is primarily a surface imaging technique. Based on the large number of polyaniline nanotubes seen in Figure 11 though, it seems likely that very few pores are unfilled with polyaniline. This would imply that PbTe/polyaniline core-shell structures have been synthesized successfully.

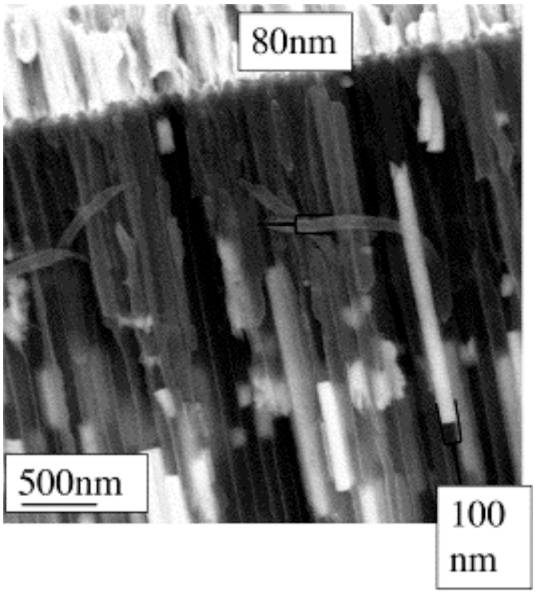

Figure 8-13. Back-scattered SEM image of PbTe/Polyaniline core-shell structures

8.8 Conclusions

Calculations reveal the parasitic effect of PAA in thermoelectric devices is large, lowering the composite ZT by orders of magnitude. To realize the predictions of high ZT nanowires, the large thermal conductivity of the PAA matrix must be minimized. Ideally, the PAA could be completely removed after the nanowires have been deposited. However, doing so would most likely erase any benefits from quantum confinement. Replacing the PAA matrix after nanowire deposition with an insulating polymer is promising, but there are several technical questions that have not been solved. Electrodepositing PbTe/polyaniline core-shell structures should allow for the removal of the PAA matrix, while maintaining electrically isolated nanowires.

Prior work on the electrodeposition of polyaniline has all focused on larger pores or thinner templates to avoid the problems of diffusion. Using a pulsed potential deposition, extremely high aspect ratio polyaniline nanotubes were deposited. The pulsed potential prevents the hydrolysis of the growing polymer chain and allows the aniline monomer to diffuse down the nanopores.

Electrodepositing PbTe into a polyaniline filled template most likely results in PbTe/polyaniline core-shell structures. However, due to the limitations of SEM and back-scattered SEM, it is difficult to say for certain. Further work needs to be conducted to determine the feasibility of creating thermoelectric devices out of these nanostructures. Numerous issues and parameters will first need to be explored, such as contacting, precisely controlling nanotube length, removing the PAA matrix, creating enough structural support, and tuning the conductivity of polyaniline. There exists a lot of potential for further study now that some of the groundwork has been laid.

Chapter 9: Conclusions

Thermoelectric nanowires are predicted to show a higher zT than their bulk counterparts through increased phonon scattering and quantum confinement effects. Efficient high temperature thermoelectrics that can function as waste heat recovery systems could make a significant impact on the energy problems of the future. Electrodeposition of nanowires in PAA templates is a cost effective and scalable method to create high zT thermoelectric nanowires. PbTe is an ideal candidate for thermoelectric nanowires because of its large Bohr exciton radius and high bulk zT.

Previous work on the electrochemical depositions of PbTe has mainly been focused on thin films and not nanowires. Thin films have all been rich in tellurium caused by the large difference in reduction potentials of Pb and Te. By using citric acid as a complexing agent for Te, the deposition potentials of Pb and Te can be brought closer together, and stoichiometric nanowires of PbTe were deposited.

Group III doped nanowires of PbTe were also deposited in PAA templates. N-type arrays were formed by incorporating indium and p-type arrays by thallium. Dopant concentrations were measured by electron microprobe and incorporation into the structure was tracked through XRD analysis of the lattice parameter. The mechanism of the dopant atom incorporation was also determined.

Work on the mechanism of thallium incorporation into PbTe led to the first ever study on the electrodeposition of thallium telluride. The electrodeposition of TlTe and Tl_5Te_3 was demonstrated both as thin films and nanowire arrays. The mechanisms of both depositions were determined through a series of CV studies. Due to their interesting crystal structures and heavy element constituents, these compounds could show promising thermoelectric properties in the nanowire form and also could serve as a starting point for the synthesis of more complex thallium tellurides.

Transport measurements were conducted on thin films and nanowires of PbTe to determine their thermoelectric properties. Depending on the growth potential, thin films exhibited very different Seebeck coefficients. It is possible that oxidation levels in the film are responsible for the differing Seebeck coefficient. Inaccuracies in the measurements could not be ruled out however.

The resistivities of nanowire arrays were all too high for a good thermoelectric device. Similar to the thin film results, oxidation of the nanowires is likely a large part of the problem. Attempts to prevent the oxidation of the nanowires resulted in slightly better resistivity values, but values still orders of magnitude higher than bulk PbTe. Until better electrical contacting methods are devised, high zT nanowire arrays are not possible.

Even if the nanowire contacting issue is resolved, parasitic losses due to the high thermal conductivity of PAA will limit the efficiency of nanowire/PAA devices. Through electrodepositing PbTe/polyaniline core-shell structures, the PAA template should be able to be removed, thus eliminating parasitic losses. Using a pulsed potential deposition, extremely high aspect ratio polyaniline nanotubes were deposited. Electrodepositing PbTe into a polyaniline filled template results in PbTe/polyaniline core-shell structures. Further work is needed to determine the thermoelectric properties of these nanowires.

References

[1] F. DiSalvo, *Science*, **285**, 703 (1999).
[2] E.J. Winder, A. B. Ellis, and GC. Lisensky, *Journal of Chemical Educucation*, **73**, 940 (1996).
[3] W. B. Gosney, *Principles of Refrigeration*; Chap 1, Cambridge University, Cambridge, U.K. (1982).
[4] C. B. Vining, *Nature Materials*, **8**, 83 (2009).
[5] L.D. Hicks and M. S. Dresselhaus, *Physical Review B,* **47**, 16631 (1993).
[6] L.D. Hicks and M. S. Dresselhaus, *Physical Review B,* **47**, 12727 (1993).
[7] L.D. Hicks, T.C. Harman, X. Sun, and M. S. Dresselhaus, *Physical Review B*, **53** 10493 (1996).
[8] N. S. Lewis and D. G. Nocera, *Proceedings of the National Academy of Sciences*, **103**, 15729 (2006).
[9] J. R. Petit, J. Jouzel, D. Raynaud, N. I. Barkov, J.-M. Barnola, I. Bassile, M. Bender, J. Chappellaz, M. Davis, G. Delaygue, M. Delmotte, V. M. Kotlyakov, M. Legrand, V. Y. Lipenkov, C. Lorius, L. Pepin, C. Ritz, E. Saltzman, and M. Stievenhard, *Nature*, **399**, 429 (1999).
[10] U. Siegenthaler, T. F. Stocker, E. Monnin, D. Luthi, J. Schwander, B. Stauffer, D. Raynaud, J.-M. Barnola, H. Fischer, V. Masson-Delmotte, and J. Jouzel, *Science*, **310**, 1313 (2005).
[11] Intergovernmental Panel on Climate Change (2001) *Climate Change 2001, Synthesis Report Summary for Policymakers* (Intergovernmental Panel on Climate Change, Washington, DC),
[12] V. S. Arunachalam and E. L. Fleischer, *MRS Bulletin*, **33**, 264 (2008).
[13] J. Yang, *International Conference on Thermoelectrics*, **24**, 155 (2005).
[14] J. P. Heremans, *Basic Research Needs to Assure a Secure Energy Future-DOE Report from the Basic Energy Sciences Advisory Committee*, February, 2003.
[15] NASA's Voyager website http://voyager.jpl.nasa.gov/spacecraft/spacecraftlife.html
[16] Mars Science Laboratory website http://mars.jpl.nasa.gov/msl/mission/technology/technologiesofbroadbenefit/power/
[17] D. Kraemer, B. Poudel, H. Feng, J. C. Caylor, B. Yu, X. Yan, Y. Ma, X. Wang, D. Wang, A. Muto, K. McEnaney, M. Chiesa, Z. Ren, and G. Chen, *Nature Materials*, **10**, 532, (2011).
[18] D. M. Rowe, Thermoelectrics Handbook Nano to Macro (CRC Taylor & Francis, 2006).
[19] G. J. Snyder, and E. S. Toberer, *Nature Materials*, **7** 105 (2008).
[20] G. A. Slack, *CRC Handbook of Thermoelectrics* (Ed. : D. M. Rowe, CRC, p. 407, 1995).
[21] G. S. Nolas, Thermoelectrics Handbook Nano to Macro (CRC Taylor & Francis, 2006).
[22] C. Uher, Thermoelectrics Handbook Nano to Macro (CRC Taylor & Francis, 2006).
[23] D. Y. Chung, T. Hogan, P. Brazis, M. Rocci-Lane, C. Kannewurf, M. Bastea, C. Uher, and M. G. Kanatzidis, *Science* **287**, 1024 (2000).
[24] S. R. Brown, S. M. Kauzlarich, F. Gascoin, and G. J. Snyder, *Chemistry of Materials* **18**, 1873 (2006).
[25] S. M. Kauzlarich, S. R. Brown, and G. J. Snyder, *Dalton Transactions* 2099 (2007).

[26] T. Ikeda, L. Collins, V. A. Ravi, F. Gascoin, S. M. Haile, and G. J. Snyder, Chemistry of Materials **19**, 763 (2007).
[27] T. Ikeda, V. A. Ravi, and G. J. Snyder, Acta Materialia 57, 666 (2009).
[28] M. Zhou, J.-F. Li, and T. Kita, *Journal of the American Chemical Society* **130**, 4527 (2008).
[29] H. Wang, J. F. Li, C. W. Nan, M. Zhou, W. S. Liu, B. P. Zhang, and T. Kita, *Applied Physics Letters* **88**, 092104 (2006).
[30] K. F. Hsu, S. Loo, F. Guo, W. Chen, J. S. Dyck, C. Uher, T. Hogan, E. K. Polychroniadis, and M. G. Kanatzidis, *Science* **303**, 818 (2004).
[31] G. A. Slack, In *Solid State Physics*, Vol. 34, H. Ehreneich, F. Seitz, D. Turnbull, Eds. (Academic Press, New York, 1979), pp. 1-71.
[32] H. J. Goldsmid, Thermoelectrics Handbook Nano to Macro (CRC Taylor & Francis, 2006).
[33] N. F. Mott, and H. Jones, *The Theory of the Properties of Metals and Alloys*, (Dover Publications, New York, 1958).
[34] J. P. Heremans, C. M. Thrush, D. T. Morelli, and M-C. Wu, *Physical Review Letters* **88**, 216801 (2002).
[35] J. P. Heremans, V. Jovovic, E. S. Toberer, A. Saramat, K. Kurosaki, A. Charoenphakdee, S. Yamanaka, and G. S. Snyder, *Science* **321**, 554 (2008).
[36] C. Dames and G. Chen, Thermoelectrics Handbook Nano to Macro (CRC Taylor & Francis, 2006).
[37] M. S. Dresselhaus, G. Dresselhaus, X. Sun, Z. Zhang, S. B. Cronin, T. Koga, J. Y. Ying, and G. Chen, *Microscale Thermophysical Engineering*, **3**, 89 (1999).
[38] T. C. Harman, P. J. Taylor, D. L. Spears, and M.P. Walsh, *J. Electron. Mater.*, **29**, L1 (2000).
[39] T. C. Harman, D. L. Spears, and M. P. Walsh, *J. Electron. Mater.*, **28**, L1 (1999).
[40] T. Koga, T. C. Harman, S. B. Cronin, and M. S. Dresselhaus, *Phys. Rev. B*, **60**, 14286 (1999).
[41] S. Cho, A. DiVenere, G. K. Wong, J. B. Ketterson, and J. R. Meyer, *Phys Rev B. Condens. Matter*, **59**, 10691 (1999).
[42] R. Venkatasubramanian, T. Colpitts, E. Watko, and J. Hutchby, in *Proceedings of the IEEE 15th International Conference on Thermoelectrics*, p. 454 (1996).
[43] T. C. Harman, D. L. Spears, and M. J. Manfra, *J. Electron. Mater.*, **25**, 1121 (1996).
[44] R. Venkatasubramanina, E, Silvola, T. Colpitts, and B. O'Quinn, *Nature* **413**, 597 (2001).
[45] J. E. Cornett and O. Rabin, *Applied Physics Letters* **98**, 182104 (2011).
[46] G. D. Mahan, *Solid State Physics* **51**, 82 (1998).
[47] F. Xiao, C. Hangarter, B. Yoo, Y. Rheem, K-H. Lee, and N. V. Myung *Electrochimica Acta* **53**, 8103 (2008).
[48] C. Boulanger, *Journal of Electronic Materials* **39**, 1818 (2010).
[49] M. Paunovic, and M. Schlesinger, *Fundamentals of Electrochemical Deposition* (Electrochemical Society Series, New York, 1998).
[50] Wikipedia http://en.wikipedia.org/wiki/Cyclic_voltammetry
[51] M. Pourbaix, Ph.D. thesis, University of Brussels, 1939.

[52] J.-J. McChesney, J. Haigh, I. M. Dharmadasa, and D. J. Mowthorpe, *Optical Materials* **6**, 63 (1996).
[53] G. D. Bengough, and J. M. Stuart, British Patent 223,994, 1923.
[54] F. Keller, M. S. Hunter, and D. L. Robinson, *Journal of the Electrochemical Society* **100**, 411 (1953).
[55] J. P. O'Sullivan, and G. C. Wood, *Proceedings of the Royal Society of London*, Ser. A. **317**, 511 (1970).
[56] O. Jessensky, F. Muller, and U. Gosele, *Applied Physics Letters* **72**, 1173 (1998).
[57] J. E. Houser, and K. R. Herbert, *Nature Materials* **8**, 415 (2009).
[58] H. Masuda and M. Satoh, *Japanese Journal of Applied Physics* **35**, 126 (1996).
[59] C. R. Martin, *Science* **266**, 1961 (1994).
[60] C. R. Martin, *Chemistry of Materials* **8**, 1739 (1996).
[61] Y. I. Ravich, B. A. Efimova, and I. A. Smirnov, *Semiconducting Lead Chalcogenides*, (Plenum Press, New York, 1970).
[62] Z. Dashevsky, Lead Chalcogenides Physics and Applications (Taylor and Francis, New York, 2003).
[63] US Department of Energy, "Atomic power in space," available at http://www.fas.org/nuke/space/index.html
[64] J.P. Angello, G. T. Prysinger, Intersociety Energy Conversion Engineering Conference, IEEE, USA, 1968, p. 986.
[65] G. Guazzoni, Intersociety Energy Conversion, IEEE, USA, 1970, p. 136.
[66] C. Wood, *Reports on Progress in Physics* **51**, 459 (1988).
[67] A. D. LaLonde, Y. Pei, H. Wang, and G. J. Snyder, *Materials Today* **14**, 526 (2011).
[68] G. L. Miessler and D. A. Tarr, *Inorganic Chemistry* (Pearson Prentice Hall, Upper Saddle River, New Jersey, 2004).
[69] S. S. Zumdahl, Chemical Principles (Houghton Mifflin Company, Boston, 2002).
[70] W. W. Scanlon, *Journal of Physical Chemistry of Solids* **8**, 423 (1959).
[71] Yu. I. Ravich, B. A. Efimova, and V. I. Tamarchenko, *Physica Status Solidi B* **43**, 453 (1971).
[72] Z. H. Dughaish, *Physica B* **322**, 203 (2002).
[73] G. S. Nolas, J. Sharp, and H. J. Goldsmid, Thermoelectrics Basic Principles and New Materials Developments (Springer, Berlin, 2001).
[74] P. Yang, Chemistry 253B lecture notes, spring 2008.
[75] F. W. Wise, *Accounts of Chemical Research* **33**, 773 (2000).
[76] Y. A. Ugai, A. P. Dynnik, S. D. Ignatovich, and E. M. Averbakh, *Elektrokhimiya* **12**, 1626 (1976).
[77] H. Saloniemi, T. Kannianen, M. Ritala, and M. Leskela *Thin Solid Films* **326**, 78 (1998).
[78] H. Saloniemi, M. Kemell, P. Ritala, and M. Leskela, *Journal of Electroanalytical Chemistry* **482**, 139 (2000).
[79] L. Beaunier, H. Cachet, R. Cortes, and M. Froment, *Journal of Electroanalytical Chemistry* **532**, 215 (2002).
[80] Y. A. Ivanova, D. K. Ivanou, and E. A. Streltsov, *Electrochemistry Communications* **9**, 599 (2007).

[81] F. Xiao, B. Yoo, M. A. Ryan, K. H. Lee, and N. V. Myung, *Electrochimca Acta* **52**, 1101 (2006).
[82] F. Xiao, B. Yoo, M. A. Ryan, K. H. Lee, and N. V. Myung, *Journal of Physical Chemistry C* **111**, 11397 (2007).
[83] L. Trahey, C. R. Becker, and A. M. Stacy, *Nano Letters* **7**, 2535 (2007).
[84] W. Liu, W. Cai, and L. Yao, *Chemistry Letters* **36**, 1362 (2007).
[85] Y. Yang, D. K. Taggart, M. A. Brown, C. Xiang, S.-C. Kung, F. Yang, J. C. Hemminger, and R. M. Penner, *ACS Nano* **3**, 4144 (2009).
[86] Y. Yang, S. C. Kung, D. K. Taggart, C. Xiang, F. Yang, M. A. Brown, A. G. Guell, T. J. Kruse, J. C. Hemminger, and R. M. Penner, *Nano Letters* **8**, 2447 (2008).
[87] Y. Yang, D. K. Taggart, M. H. Cheng, J. C. Hemminger, and R. M. Penner, *The Journal of Physical Chemistry Letters* **1**, 3004 (2010).
[88] H. Jung, D.-Y. Park, F. Xiao, K. H. Lee, Y.-H. Choa, B. Yoo, and N. V. Myung, *The Journal of Physical Chemistry C* **115**, 2993 (2011).
[89] M. S. Martin-Gonzalez, A. L. Prieto, R. Gronsky, T. Sands, and A. M. Stacy, *Journal of the Electrochemical Society* **149**, C546 (2002).
[90] E. Mori, C. K. Baker, J. R. Reynolds, and K. Rajeshwar, *Journal of Electroanalytical Chem*istry **252**, 441 (1988).
[91] M. Traore, R. Modolo, and O. Vittori, *Electrochimica Acta*, **33**, 991 (1988).
[92] M. P. R. Panicker, M. Knaster, and F. A. Kroger, *J. Electrochem. Soc*., **125**, 566 (1978).
[93] CRC Handbook of Chemistry and Physics (CRC Press, Cleveland, 2002).
[94] A. J. M. Valente, A. C. F. Ribeiro, V. M. M. Lobo, and A. Jimenez, *Journal of Molecular Liquids* **111**, 33 (2004).
[95] V. Richoux, S. Diliberto, C. Boulanger, and J. M. Lecuire, *Electrochimica Acta* **52**, 3053 (2007).
[96] A. S. Fouda and A. K. Mohamed, *Bulletin of Electrochemistry* **6**, 677 (1990).
[97] F. Chraibi, M. Fahoume, A. Ennaoui, and J. L. Delpancke, *Physica Status Solidi A* **186**, 373 (2001).
[98] T. Ishizaki, T. Ohtomo, and A. Fuwa, *J. Phys. D: App. Phys.*, **37**, 255 (2004).
[99] T. Ishizaki, T. Ohtomo, and A. Fuwa, *Journal of the Electrochemical Society* **151**, C161 (2004).
[100] A. M. Hageman, *Journal of the American Chemical Society* **41**, 342 (1919).
[101] A. Albeck, H. Weitman, B. Sredni, and M. Albeck, *Inorganic Chemistry* **37**, 1704 (1998).
[102] J. Keyani, A. M. Stacy, and J. Sharp, *Applied Physics Letters* **89**, 233106 (2006).
[103] J.-C. Lin, K.-C. Hsie, R. C. Sharma, and Y. A. Chang, *Bulletin of Alloy Phase Diagrams* 10, 340 (1989).
[104] B. J. Sealy and A. J. Crocker, *Journal of Materials Science* **8**, 1737 (1973).
[105] Y. Gelbstein, Z. Dashevsky, and M. P. Dariel, *Physica B* **363**, 196 (2005).
[106] D. M. Freik, V. M. Boichuk, and L. I. Mezhilovskaya, *Inorganic Materials* **40**, 1171 (2004).
[107] A. K. Tkalich, V. N. Demin, and V. P. Zlomanov, *Journal of Solid State Chemistry* **116**, 33 (1995).

[108] P. G. Rustamov, M. A. Alidzhanov, and Ch. I. Abilov, *Physica Status Solidi A* **12**, K103 (1972).
[109] S. A. Belokon, S. D. Larchuk, S. V. Plyatsko, F. F. Sizov, and V. V. Teterkin, *Inorganic Materials* **24**, 1618 (1988).
[110] A. M. Samoilov, S. A. Buchnev, E. A. Dolgopolova, Yu. V. Synorov, and A. M. Khoviv, *Inorganic Materials* **40**, 349 (2004).
[111] J. C. Woolley and B. R. Pamplin, *Journal of the Less-Common Metals* **1**, 363 (1959).
[112] H. Okamoto, *Journal of Phase Equilibrium* **12**, 507 (1991).
[113] Y. V. Voroshilov, M. I. Gurzan, Z. Z. Kish, and L. V. Lada, *Inorganic Mate*rials, **24**, 1265 (1988).
[114] P. G. Rustamov, M. A. Alidzhanov, and C. I. Abilov, *Inorganic Materials*, **10**, 1053 (1974).
[115] T. Ikari, and K. Hashimoto, *Physica Status Solidi (b)*, **86** 239 (1978)
[116] A. A. Toure, G. Kra, R. Eholie, J. Olivier-Fourcade, and J.-C. Jumas, *Journal of Solid State Chemistry*, **87** 229 (1990).
[117] A. A. Hussein, M. M. Nassary, G. A. Gamal, and A. T. Naga, *Crystal Research and Technology*, **28**, 1021 (1993).
[118] M. A. McGuire, T. K. Reynolds, and F. J. DiSalvo, *Chemistry of Materials*, **17**, 2875 (2005).
[119] B. Wolfing, C. Kloc, J. Teubner, and E. Bucher, *Physical Review Letters*, **86**, 4350 (2001).
[120] K. Kurosaki, A. Kosuga, H. Muta., M. Uno, and S. Yamanaka, *Applied Physics Letters* **87**, 061919 (2005).
[121] J. W. Sharp, B. C. Sales, D. G. Mandrus, and B. C. Chakoumakos, *Applied Physics Letters*, **74**, 3794 (1999).
[122] V. P. Vasil'ev, A. V. Nikol'skaya, Ya. I. Gerasimov, and A. F. Kuznetsov, *Izv. Akad. Nauk SSSR, Neorg. Mater.,* **4**, 1040 (1968).
[123] M. P. R. Panicker, M. Knaster, and F. A. Kroger, *Journal of the Electrochemical Soc*iety **125**, 568 (1978).
[124] F. A. Kroger, *Journal of the Electrochem*ical Society. **125**, 2028 (1978).
[125] V. P. Vasil'ev, *Inorganic Mater*ials, **43**, 155 (2007).
[126] P. Grosse, *Springer Tracts in Modern Physics* **48**, 1 (1969).
[127] K. Stowe, *Journal of Solid State Chemistry* **149**, 123 (2000).
[128] C. Konigstein and M. Neumann-Spallart, *Journal of the Electrochemical Society*, **145**, 337 (1998).
[129] W. J. Danaber and L. E. Lyons, *Austrian Journal of Chem*istry, **37**, 689 (1984).
[130] G. A. Shaw, I. P. Parkin, *Inorganic Chem*istry, **40**, 6940 (2001).
[131] K. Bruckardt, K. Schubert, *Journal of Less-Common Metals*, **20**, 426 (1969).
[132] J. Weis, H. Schafer, B. Eisenmann, and G. Schon, *Z. Naturforsh.*, **B29**, 585 (1979).
[133] A. Abba-Toure, G. Kra, R. Eholie, J. Olivier-Fourcade, and J. C. Jumas, *Journal of Solid State Chemistry*, **87**, 229 (1990).
[134] B.Bozzini, M. A. Baker, P. L. Cavallotti, E. Cerri, and C Lenardi, *Thin Solid Films*, **361**, 388 (2000).
[135] L. J. Van der Pauw, *Philips Technical Review,* **20**, 220 (1958).
[136] H. Saloniemi, *VTT Publications*, **423**, 1 (2000).

[137] A. Mondal, N. Mukherjee, S. K. Bhar, and D. Banerjee, *Thin Solid Films*, **515**, 1255 (2006).
[138] Z. Dashevsky, E. Shufer, V. Kasiyan, E. Flitsiyan, and L. Chernyak, *Physica B*, **405**, 2380 (2010).
[139] J. Wang, J. Hu, X. Sun, A. M. Agarwal, L. C. Kimerling, D. R. Lim, and R. A. Synowicki, *Journal of Applied Physics*, **104**, 053707 (2008).
[140] C. Sagan, *Billions and Billions,* (Random House, New York, 1997).
[141] H. E. Cheng, and M. H. Hon, *Journal of Crystal Growth*, **142**, 117 (1994).
[142] T. C. Harman, *Journal of Applied Physics*, **29**, 1373 (1958).
[143] L. Trahey, Dissertation (2007).
[144] J. Keyani, A. M. Stacy, and J. Sharp, *Journal of Applied Physics*, **89**, 233106 (2006).
[145] S. Y. Jang, H. S. Kim, J. Park, M. Jung, J. Kim, S. H. Lee, J. W. Roh, and W. Lee, *Nanotechnology*, **20**, 415204 (2009).
[146] M. Fardy, A. I. Hochbaum, J. Goldberger, M. M. Zhang, and P. Yang, *Advanced Materials*, **19**, 3047 (2007).
[147] Y. Yang, D. K. Taggart, M. H. Cheng, J. C. Hemminger, and R. M. Penner, *Journal of Physical Chemistry Letters*, **1**, 3004 (2010).
[148] H. Jung, D.-Y. Park, F. Xiao, K. H. Lee, Y.-H. Choa, B. Yoo, and N. V. Myung, *Journal of Physical Chemistry C*, **115**, 2993 (2011).
[149] M. Paunovic, *Plating and Surface Finishing*, **70**, 62 (1983).
[150] V. V. Robozerov, V. A. Zykov, and T. A. Gavrikova, *Inorganic Materials*, **36**, 177 (2000).
[151] D. A. Borca-Tascuic and G. Chen, *Journal of Applied Physics*, **97**, 084303 (2005).
[152] K. G. Biswas, T. D. Sands, B. A. Cola, and X. Xu, *Applied Physics Letters*, **94**, 223116 (2009).
[153] K. Nielsch, J. Choi, K. Schwirn, R. B. Wehrspohn, and U. Gusele, *Nano Letters*, **2**, 677 (2002).
[154] Y. Yang, *Physical Properties of Polymers Handbook*, (AIP, New York, 1996).
[155] H. Letheby, *Journal of the Chemical Society*, **15**, 161 (1862).
[156] Wikipedia "Polyaniline" http://en.wikipedia.org/wiki/Polyaniline
[157] P. B. Kaul, K. A. Day, and A. R. Abramson, *Journal of Applied Physics*, **101**, 083507 (2007).
[158] H. Yan, N. Ohno, and N. Toshima, *Chemistry Letters*, 392 (2000).
[159] J. Stejskal and R. G. Gilbert, *International Union of Pure and Applied Chemistry*, **74**, 857 (2002).
[160] P. N. Adams, P. J. Laughlin, A. P. Monkman, and A. M. Kenwright, *Polymer*, **37**, 3411 (1996).
[161] H. Yan, T. Ohta, and N. Toshima, *Macromolecule Material Engineering*, **286**, 139 (2001).
[162] O. Bubnova, Z. U. Khan, A. Malti, S. Braun, M. Fahlman, M. Berggren, and X. Crispin, *Nature Materials*, **10**, 429 (2011).
[163] A. R. Elkias, M. M. Gvozdenovic, B. Z. Jugovic, J. S. Stevanovic, N. D. Nikolic, B. N. Grgur, *Progress in Organic Coatings*, **71**, 32 (2011).
[164] D. E. Stilwell and S.-M. Park, *Journal of Electrochemical Society*, **135**, 2254 (1988).

[165] M. Delvaux, J. Duchet, P.-Y. Stavaux, R. Legras, S. D.-Champagne, *Synthetic Metals*, **113**, 275 (2000).
[166] C. R. Martin, *Accounts of Chemical Research*, **28**, 61 (1995).
[167] B. H. Kim, D. H. Park, J. Joo, S. G. Yu, and S. H. Lee, *Synthetic Metals*, **150**, 279 (2005).
[168] Y. Cao and T. E. Mallouk, *Chemistry of Materials*, **20**, 5260 (2008).
[169] S. M. Yang, K. H. Chen, and Y. F. Yang, *Synthetic Metals*, **152**, 65 (2005).
[170] H. Cao, Z. Xu, D. Sheng, J. Hong, H. Sang, and Y. Du, *Journal of Materials Chemistry*, **11**, 958 (2001).
[171] H. Cao, C. Tie, Z. Xu, J. Hong, and H. Sang, *Applied Physics Letters*, **78**, 1592 (2001).
[172] A. Pruna, B. Branzoi, and F. Branzoi, *Journal of Applied Electrochemistry*, **41**, 77 (2011).
[173] H. Cao, Z. Xu, H. Sang, D. Sheng, and C. Tie, *Advanced Materials*, **13**, 121 (2001).
[174] X. Xu, L. Chen, C. Wang, Q. Yao, and C. Feng, *Journal of Solid State Chemistry*, **178**, 2163 (2005).
[175] D. E. Stilwell and S.-M. Park, *Journal of the Electrochemical Society*, **135**, 2497 (1988).
[176] V. Tsakova and A. Milchev, *Electrochimica Acta*, **36**, 1579 (1991).
[177] V. Tsakova and A. Milchev, *Journal of Electroanalytical Chemistry*, **346**, 85 (1991).
[178] V. Rajendran, A. Gopalan, T. Vasudevan, W.-C. Chen, and T.-C. Wen, *Materials Chemistry and Physics*, **65**, 320 (2007).
[179] H.-H. Zhou, J.-B. Wen, W.-H Ning, C.-P. Fu, J.-H. Chen, and Y.-F. Kuang, *Journal of Applied Polymer Science*, **104**, 458 (2007).
[180] H. Zhou, J. Wen, X. Ning, C. Fu, J. Chen, and Y. Kuang, *Synthetic Metals*, **157**, 98 (2007).
[181] H.-F. Jiang and X.-X. Liu, *Electrochimica Acta*, **55**, 7175 (2010).